

The Pennsylvania State University
The Graduate School
Department of Aerospace Engineering

**CFD INVESTIGATION OF UNSTEADY ROTORCRAFT
AIRFOIL AERODYNAMICS**

A Thesis in
Aerospace Engineering

by
James G. Coder

© 2010 James G. Coder

Submitted in Partial Fulfillment
of the Requirements
for the Degree of

Master of Science

August 2010

The thesis of James G. Coder was reviewed and approved* by the following:

Mark D. Maughmer
Professor of Aerospace Engineering
Thesis Advisor

Kenneth S. Brentner
Professor of Aerospace Engineering

George A. Lesieutre
Professor of Aerospace Engineering
Head of the Department of Aerospace Engineering

*Signatures are on file in the Graduate School

ABSTRACT

As part of an effort to improve rotorcraft performance, the ability of the OVERFLOW computational fluid dynamics solver to predict the onset of dynamic stall and the influence of upstream miniature trailing-edge effectors (MiTEs) has been investigated. Static CFD validation cases and grid resolution studies were first performed for airfoils both clean and with Gurney flaps. It was determined that CFD generally performs well in predicting the zero-lift angle of attack and zero-lift pitching-moment coefficient for an airfoil, but the fully turbulent assumption causes the maximum lift coefficient to be generally overpredicted.

Several trailing-edge stall suppression and double stall cases from the U.S. Army Dynamic Stall Data Package were used to provide experimental validation of the computational methods used in OVERFLOW for dynamic stall. The overprediction of the maximum lift coefficient resulted in the introduction of a quasi-steady scaling factor for these cases; the use of this scaling factor is shown to greatly improve the quality of the dynamic stall predictions.

The aerodynamic response of a deploying and retracting upstream MiTE, which is a deployable Gurney flap, has also been investigated and validated for the purpose of providing “virtual wind tunnel” data for the development of an unsteady aerodynamic model. Moving the MiTE upstream of the trailing edge creates a lower-surface vortex which causes significant deviations from trailing-edge MiTE behavior that had previously been observed. This vortex was observed in both 2-D unsteady RANS and 3-D DES simulations, with the transient responses being qualitatively similar for both methods.

TABLE OF CONTENTS

LIST OF FIGURES	vi
LIST OF TABLES	x
LIST OF SYMBOLS	xi
ACKNOWLEDGEMENTS	xiii
Chapter 1 Introduction	1
1.1 Introduction	1
1.2 Dynamic Stall	2
1.2.1 Description	2
1.2.2 Prediction Methods	3
1.3 Miniature Trailing-Edge Effectors	4
1.4 Goals	9
1.4.1 Static CFD Validation	9
1.4.2 Dynamic Stall CFD Predictions	10
1.4.3 Upstream MiTE CFD Predictions	10
Chapter 2 Description of Numerical Methods	12
2.1 Solvers and Solution Strategies	12
2.1.1 OVERFLOW 2.1	12
2.1.2 ANSYS FLUENT 12.1	13
2.1.3 XFOIL 6.96	14
2.2 Grid Generation Software	14
2.2.1 Chimera Grid Tools 2.0	14
2.2.2 Airfoil Surface Grid Generation Software	15
2.2.3 GAMBIT 2.4.6	16
Chapter 3 Static CFD Validation	18
3.1 Somers S408 Airfoil	18
3.2 OVERFLOW 2.1 Grid Resolution Study	18
3.3 Comparison with Experiment	21
3.5 Gurney Flap Predictions	23
3.6 Somers S903 Airfoil	26
3.7 Assessment of Results	31
Chapter 4 Dynamic Stall CFD Predictions	32
4.1 Vertol VR-7 Airfoil	32
4.2 Static Predictions	34
4.3 Quasi-Steady Scaling	36

4.3.1 Lift Scaling	36
4.3.2 Moment Scaling	37
4.4 Trailing-Edge Stall Suppression	38
4.5 Double Stall.....	46
Chapter 5 Upstream Miniature Trailing-Edge Effector Predictions	51
5.1 Upstream MiTE Grids	51
5.2 Baseline Operating Conditions	54
5.3 Indicial and Ramp Deployments	55
5.3.1 Verification of CFD Indicial Response	55
5.3.2 Vortex due to Upstream MiTE.....	58
5.3.3 Slower Ramp Deployments.....	69
5.3.4 Verification of Two-Dimensional Approach	71
5.3.5 Effect of Compressibility	74
5.4 Ramp Retractions.....	77
5.4.1 Effect of Retraction Rate.....	77
5.4.2 Effect of Compressibility	79
5.5 Oscillating Deployments	82
5.5.1 Effect of Reduced Frequency	82
5.5.2 DES Verification	87
5.5.3 Comparison with Experiment.....	89
Chapter 6 Summary and Conclusions	91
6.1 Static CFD Analyses	91
6.2 Dynamic Stall Predictions.....	91
6.3 CFD Investigation of Upstream MiTEs	92
6.4 Recommendations for Future Work.....	94
6.4.1 Transition in Unsteady CFD Simulations	94
6.4.2 Additional Unsteady MiTE Experiments	94
Appendix A Description of Langtry-Menter Turbulence Model [40-42]	95
Appendix B Airfoil Coordinates	97
REFERENCES	99

LIST OF FIGURES

Figure 1-1. Boeing AH-64 Apache helicopter	1
Figure 1-2. Flow morphology and lift, drag, and moment characteristics of an airfoil undergoing dynamic stall [1]	3
Figure 1-3. Liebeck's hypothetical flow structure around a Gurney flap [16]	4
Figure 1-4. Change in maximum lift coefficient with varying Gurney flap heights and chordwise locations for the S903 airfoil [28].....	5
Figure 1-5. Time-averaged streamlines of an upstream Gurney flap for the S903 airfoil [5].....	6
Figure 1-6. S903 airfoil with an oscillating $0.02c$ MiTE located at $0.90c$ (a) and at $1.00c$ (b), $\alpha = 0^\circ$, $M_\infty = 0.1$, $R = 1.0 \times 10^6$, and $k = 0.14$ [7]	7
Figure 1-7. Instantaneous streamlines of an S809 airfoil with a $0.011c$ Gurney flap at $0.95c$ [23]	7
Figure 1-8. Unsteady aerodynamic responses for various MiTE deployment times on the S809 airfoil [23]	8
Figure 2-1. Schematic diagram of three-block C-grid	17
Figure 3-1. S408 predictions from OVERFLOW for various grid resolutions, $R = 1.5 \times$ 10^6	20
Figure 3-2. S408 airfoil predictions from OVERFLOW compared with experiment for the clean configuration, $R = 1.5 \times 10^6$	22
Figure 3-3. S408 airfoil with a $0.0238c$ Gurney flap at $0.90c$ predictions from OVERFLOW compared with experiment, $R = 1.5 \times 10^6$	24
Figure 3-4. Change in drag coefficient of the S408 with $0.0238c$ Gurney flap at $0.90c$ from a clean configuration predicted by OVERFLOW and compared with experiment, $R = 1.5 \times 10^6$	25
Figure 3-5. Somers S903 airfoil geometry [52]	27
Figure 3-6. S903 airfoil with a $0.0208c$ Gurney flap at $0.90c$ predictions from OVERFLOW compared with experiment, $R = 1.0 \times 10^6$	28
Figure 3-7. Comparison of time-averaged streamlines for the S903 airfoil in both clean (a) and $0.0208c$ Gurney flap at $0.90c$ (b) configurations, $\alpha = 4^\circ$, $R = 1.0 \times 10^6$, $M_\infty =$ 0.2	29

Figure 3-8. Close-up of time-averaged streamlines near a 0.0208c Gurney flap upstream at 0.90c on the S903 airfoil, $\alpha = 4^\circ$, $R = 1.0 \times 10^6$, $M_\infty = 0.2$	30
Figure 3-9. Pressure distributions for the S903 airfoil for clean and 0.0208c Gurney flap at 0.90c configuration, $\alpha = 4^\circ$, $R = 1.0 \times 10^6$, $M_\infty = 0.2$	30
Figure 4-1. Vertol VR-7 airfoil geometry.....	32
Figure 4-2. Far-field stretched Cartesian (a) and near-field body-fitted O-type (b) overset grids for VR-7 dynamic stall cases in OVERFLOW 2.1	33
Figure 4-3. Comparison of CFD, XFOIL, and experimental [15] predictions for the VR-7 airfoil at $M_\infty = 0.184$, $R = 2.56 \times 10^6$	35
Figure 4-4. Dynamic stall predictions for the VR-7 compared with experiment [15] at $M_\infty = 0.184$, $R = 2.56 \times 10^6$, $\alpha = 4.55^\circ \pm 10.05^\circ$, and $k = 0.01$	41
Figure 4-5. Dynamic stall predictions for the VR-7 compared with experiment [15] at $M_\infty = 0.184$, $R = 2.56 \times 10^6$, $\alpha = 4.55^\circ \pm 10.05^\circ$, and $k = 0.025$	42
Figure 4-6. Dynamic stall predictions for the VR-7 compared with experiment [15] at $M_\infty = 0.184$, $R = 2.56 \times 10^6$, $\alpha = 4.55^\circ \pm 10.05^\circ$, and $k = 0.1$	43
Figure 4-7. Dynamic stall predictions for the VR-7 compared with experiment [15] at $M_\infty = 0.184$, $R = 2.56 \times 10^6$, $\alpha = 4.55^\circ \pm 10.05^\circ$, and $k = 0.25$	44
Figure 4-8. Error in predicted maximum lift coefficient as a function of reduced frequency for both scaled and unscaled simulations	45
Figure 4-9. Error in predicted stall angle of attack as a function of reduced frequency for both scaled and unscaled simulations	45
Figure 4-10. Dynamic stall predictions for the VR-7 compared with experiment [15] at $M_\infty = 0.184$, $R = 2.53 \times 10^6$, $\alpha = 14.77^\circ \pm 9.90^\circ$, and $k = 0.025$	48
Figure 4-11. Dynamic stall predictions for the VR-7 compared with experiment [15] at $M_\infty = 0.185$, $R = 2.60 \times 10^6$, $\alpha = 14.78^\circ \pm 9.90^\circ$, and $k = 0.10$	49
Figure 4-12. Dynamic stall predictions for the VR-7 compared with experiment [15] at $M_\infty = 0.185$, $R = 2.58 \times 10^6$, $\alpha = 14.77^\circ \pm 9.90^\circ$, and $k = 0.20$	50
Figure 5-1. Near-field grid with a hole cut in far-field grid for the VR-7 with a 0.02c MiTE at 0.90c	53
Figure 5-2. Body-fitted grid for a 0.02c MiTE retracted (a), partially extended (b), and fully deployed (c)	53
Figure 5-3. Close up of body-fitted grids and collar grids with the MiTE retracted	54
Figure 5-4. Half-sine ramp deployment scheme for $k_{HS} = 0.1$	56

Figure 5-5. Comparison of the aerodynamic response of an indicially-deployed, infinitely thin MiTE with the response of a finite-thickness MiTE deployed at $k_{HS} = 10$, both $0.02c$ high located at $0.90c$ with $\alpha = 5^\circ$, $M_\infty = 0.3$, $R = 4 \times 10^6$	57
Figure 5-6. Half-sine ramp deployment of a $0.02c$ MiTE at $1.00c$ on the VR-12 airfoil, $k_{HS} = 10$, with $\alpha = 5^\circ$, $M_\infty = 0.3$, $R = 4 \times 10^6$	61
Figure 5-7. Aerodynamic predictions for a $k_{HS} = 10$ ramp deployment of a $0.02c$ MiTE at $0.90c$ on the VR-7 airfoil, $M_\infty = 0.3$, $R = 4 \times 10^6$, and $\alpha = 0^\circ$, 5° , and 10°	62
Figure 5-8. Half-sine ramp deployment of a $0.02c$ MiTE upstream at $0.90c$ for various airfoils, $k_{HS} = 10$, with $\alpha = 5^\circ$, $M_\infty = 0.3$, $R = 4 \times 10^6$	63
Figure 5-9. Pressure distributions for the VR-7, VR-12, and S408 airfoils at $c_l = 0.7$, $M_\infty = 0.3$, and $R = 4 \times 10^6$	64
Figure 5-10. Pressure contours (red = high, blue = low) of select frames following a $k_{HS} = 10$ half-sine deployment of a $0.02c$ MiTE at $0.90c$ on the VR-7 airfoil, $\alpha = 5^\circ$, $M_\infty = 0.3$, $R = 4 \times 10^6$	65
Figure 5-11. Entropy contours (red = high, blue = low) of select frames following a $k_{HS} = 10$ half-sine deployment of a $0.02c$ MiTE at $0.90c$ on the VR-7 airfoil, $\alpha = 5^\circ$, $M_\infty = 0.3$, $R = 4 \times 10^6$	67
Figure 5-12. Comparison of aerodynamic responses of the VR-7 airfoil for various half-sine deployments of a $0.02c$ MiTE at $0.90c$, $\alpha = 5^\circ$, $M_\infty = 0.3$, $R = 4 \times 10^6$	70
Figure 5-13. Comparison of DES (3-D) and unsteady RANS (2-D) predictions for a $k_{HS} = 1.0$ half-sine MiTE deployment on a VR-7 airfoil, $\alpha = 5^\circ$, $M_\infty = 0.3$, $R = 4 \times 10^6$	73
Figure 5-14. Comparison of $M_\infty = 0.3$ and $M_\infty = 0.5$ aerodynamic responses of the VR-7 airfoil for a $k_{HS} = 0.05$ half-sine deployment of a $0.02c$ MiTE at $0.90c$, $\alpha = 5^\circ$, $R = 4 \times 10^6$	75
Figure 5-15. Comparison of $M_\infty = 0.3$ and $M_\infty = 0.5$ aerodynamic responses of the VR-7 airfoil for a $k_{HS} = 0.25$ half-sine deployment of a $0.02c$ MiTE at $0.90c$, $\alpha = 5^\circ$, $R = 4 \times 10^6$	76
Figure 5-16. Comparison of aerodynamic responses of the VR-7 airfoil for various half-sine retractions of a $0.02c$ MiTE at $0.90c$, $\alpha = 5^\circ$, $M_\infty = 0.3$, $R = 4 \times 10^6$	78
Figure 5-17. Comparison of $M_\infty = 0.3$ and $M_\infty = 0.5$ aerodynamic responses of the VR-7 airfoil for a $k_{HS} = 0.1$ half-sine retraction of a $0.02c$ MiTE at $0.90c$, $\alpha = 5^\circ$, $R = 4 \times 10^6$	80
Figure 5-18. Comparison of $M_\infty = 0.3$ and $M_\infty = 0.5$ aerodynamic responses of the VR-7 airfoil for a $k_{HS} = 0.25$ half-sine retraction of a $0.02c$ MiTE at $0.90c$, $\alpha = 5^\circ$, $R = 4 \times 10^6$	81

Figure 5-19. Comparison of limit-cycle aerodynamic responses of the VR-7 airfoil for various oscillatory deployments of a $0.02c$ MiTE at $0.90c$, $\alpha = 5^\circ$, $M_\infty = 0.3$, $R = 4 \times 10^6$	84
Figure 5-20. Comparisons between CFD predictions and Kinzel's trailing-edge MiTE model for $k = 0.2$, $M_\infty = 0.3$, $\alpha = 10^\circ$ [5]	86
Figure 5-21. Comparison of DES (3-D) and unsteady RANS (2-D) predictions for a $k = 0.25$ oscillating MiTE deployment on a VR-7 airfoil, $\alpha = 5^\circ$, $M_\infty = 0.3$, $R = 4 \times 10^6$	88
Figure 5-22. Comparison of OVERFLOW predictions with experiment [58] for a $0.025c$ MiTE at $0.90c$ oscillating at $k = 0.204$ on an NACA 0012 airfoil, $R = 0.348 \times 10^6$	90

LIST OF TABLES

Table 3-1. Summary of key predictions for S408 grid resolution study, $R = 1.5 \times 10^6$	19
Table 4-1. Summary of CFD and XFOIL theoretical predictions compared with experiment for VR-7 airfoil, $M_\infty = 0.184$, $R = 2.56 \times 10^6$	34
Table B-1. Somers S903 airfoil coordinates [52]	97
Table B-2. Vertol VR-7 airfoil coordinates [30].....	98

LIST OF SYMBOLS

C_p	=	pressure coefficient, $(p - p_\infty)/q_\infty$
c	=	airfoil chord length
c_d	=	profile-drag coefficient
c_l	=	section lift coefficient
c_l'	=	scaled section lift coefficient
c_m	=	section pitching-moment coefficient about the quarter-chord point
h_{GF}	=	static Gurney flap height
h_{MiTE}	=	instantaneous MiTE deployment height
k	=	reduced frequency, $\omega c/(2V_\infty)$
k_{HS}	=	equivalent reduced frequency of a half-period sine wave
M_∞	=	freestream Mach number
p	=	local static pressure
p_∞	=	freestream static pressure
q_∞	=	freestream dynamic pressure, $\rho_\infty V_\infty^2/2$
R	=	Reynolds number based on chord and freestream conditions, $\rho_\infty V_\infty c/\mu$
s	=	reduced time, $2t^*$
T_{deploy}^*	=	non-dimensional MiTE-deployment time
t	=	time
t^*	=	non-dimensional time, tV_∞/c
V_∞	=	freestream velocity
x	=	chordwise coordinate
x_{MiTE}	=	chordwise Gurney flap location
y^+	=	non-dimensional turbulent boundary layer coordinate

α	=	angle of attack
α'	=	scaled angle of attack
$\Delta c_{(l,d,m)}$	=	change in aerodynamic coefficient
μ	=	molecular viscosity
ρ_∞	=	freestream air density
ω	=	circular frequency of oscillation

Subscripts

0	=	zero lift
GF	=	Gurney flap
max	=	maximum
$norm$	=	normalized
static	=	static data

ACKNOWLEDGEMENTS

This work could not have been completed without the support of my wife, Julie, who is always there for me and always willing to support me while I'm working on my research.

I would like to thank the Penn State Vertical Lift Research Center of Excellence, through which this research was funded. Along with that, I want to thank Dr. Preston B. Martin of the U.S. Army AFDD for being the technical monitor for this research and encouraging me to keep working on the dynamic stall problem.

Special thanks goes out to Kurt Acheson of Boeing Research and Technology for giving me the first crash course in CFD that started it all and Dr. Michael Kinzel of Penn State ARL for giving me help and guidance throughout my research.

I must also mention Bernardo Augusto de Oliveira Vieira, as his persistence in working on the MiTE model never left with me without some CFD to run, and his patience in explaining how his current model works helped me to understand my own task so much better.

Last, but not least, I want to sincerely thank Dr. Mark D. Maughmer for accepting me as a graduate student and keeping me on my toes with new research topics and for always being somebody to talk to about new ideas.

Chapter 1

Introduction

1.1 Introduction

The maximum forward speed of most rotorcraft configurations (such as the helicopter shown in Fig. 1-1) is often limited by a combination of compressibility effects on the advancing blades and dynamic stall on the retreating blades. These limitations usually become even more stringent with high blade loading and high altitude or hot day operating conditions [1,2].



Figure 1-1. Boeing AH-64 Apache helicopter

While these issues are straightforward to address for fixed-wing aircraft, the diverse operating environment of a rotor in forward flight generally requires the blade geometry to be capable of handling both limitations. Passive methods of addressing the individual limitations,

such as airfoil design and blade tip speed, tend to be conflicting. Mitigating the compressibility effects favors a slow hover tip Mach number with thin airfoils designed for low lift coefficients, while reducing the amount of retreating blade stall favors high tip speeds and airfoils designed for high lift coefficients. Thus, efforts for expanding the rotorcraft operating envelope and improving the maximum speed must turn to active control of the rotor blade.

One method which has been widely considered is the use of miniature trailing-edge effectors (MiTEs), which are active, deployable Gurney flaps. MiTEs have the potential to increase rotorcraft performance if they can be stored within the blade and deployed as needed. Such devices allow for airfoils to be optimized more for the advancing blade compressibility requirements without sacrificing as much maximum lift coefficient on the retreating blade [3-11].

1.2 Dynamic Stall

1.2.1 Description

Dynamic stall is a phenomenon that occurs whenever an airfoil exceeds its static stall angle of attack as a result of any unsteady, time-dependent motion, and is characterized graphically in Fig. 1-2 [1]. The boundary layer development is lagged, which delays the trailing-edge separation to a higher angle of attack. Separation then occurs from the leading edge, creating a bound vortex on the upper surface which increases the lift of the airfoil. Eventually the leading-edge vortex is convected downstream and creates a rapid drop in lift and an increase in nose-down pitching moment. After the vortex is convected downstream with decreasing angle of attack, the flow reattaches.

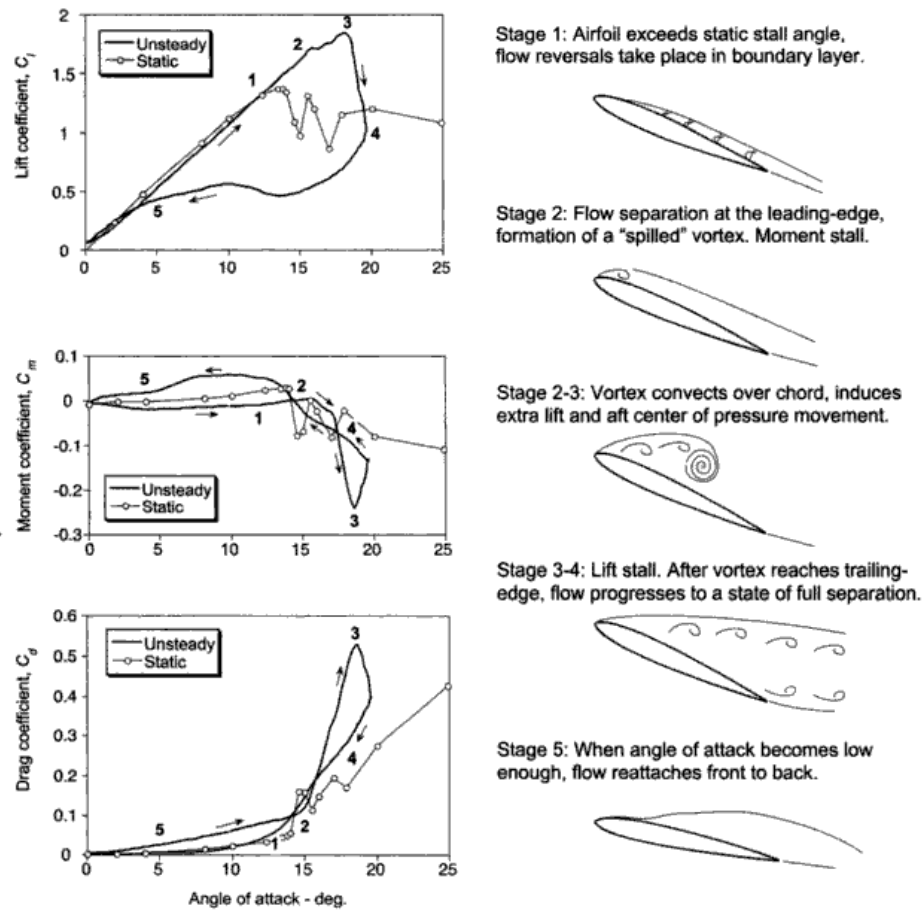


Figure 1-2. Flow morphology and lift, drag, and moment characteristics of an airfoil undergoing dynamic stall [1]

1.2.2 Prediction Methods

Several methods exist for predicting the onset and subsequent characteristics of dynamic stall, including the Leishman-Beddoes indicial [12] and the ONERA [13] semi-empirical models, and computational fluid dynamics (CFD). While McCroskey attained good agreement using CFD for predicting dynamic stall [14], it is still believed that there is much room for improvement using this technology [15].

1.3 Miniature Trailing-Edge Effectors

Miniature trailing-edge effectors (MiTEs) are active Gurney flaps which can be stored inside a rotor blade and deployed when needed. Gurney flaps were invented by race car driver Dan Gurney as a way to increase the down-force produced by the wing of his Indianapolis 500 car. Gurney flaps were experimentally investigated by Liebeck and were shown to increase the maximum lift coefficient of an airfoil by nearly 30%. Liebeck also proposed a hypothetical flow structure around the flap, shown in Fig. 1-3, which moves the Kutta condition off the surface of the airfoil and increases lift [16]. Computational investigations into the flow field around Gurney flaps by Jang et al. [17], Date and Turnock [18], Lee and Kroo [19,20], Kinzel et al. [5-8], van Dam et al. [21-24], and others have confirmed Liebeck's hypothesis.

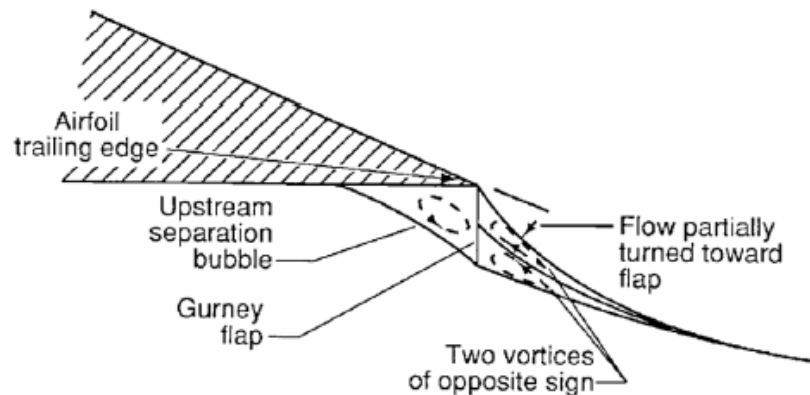


Figure 1-3. Liebeck's hypothetical flow structure around a Gurney flap [16]

If a Gurney flap can be stored within a rotor blade and deployed as needed, they have great potential to increase rotorcraft performance [3-6,10,11] and reduce vibratory loads [25-27]. Storing the MiTE usually entails moving it upstream of the trailing edge to a place where the airfoil has sufficient depth for retraction, but this has the effect of reducing the effectiveness of the MiTE. The aerodynamic effectiveness of an upstream Gurney flap was investigated

experimentally by Bramesfeld and Maughmer [28], with key results included as Fig. 1-4. It was observed that for a given chordwise location, the change in maximum lift coefficient is nearly linear with the height of the flap. As would be expected, the effectiveness of a Gurney flap decreases the further upstream it is located.

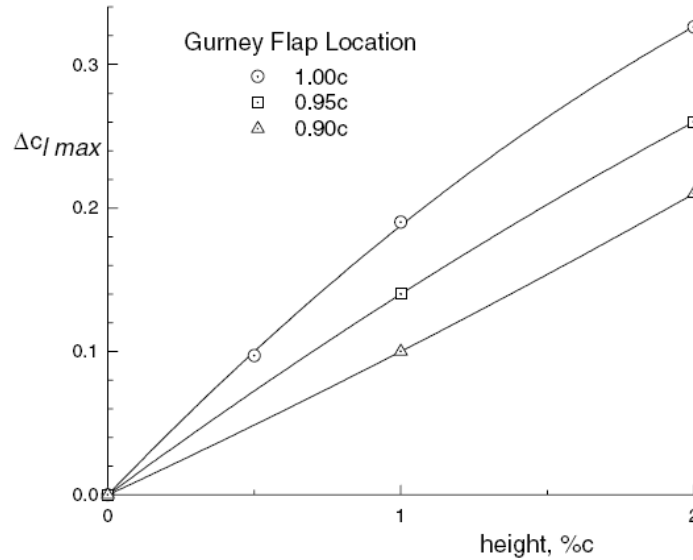


Figure 1-4. Change in maximum lift coefficient with varying Gurney flap heights and chordwise locations for the S903 airfoil [28]

The reduction in upstream MiTE effectiveness was investigated computationally by Kinzel [5-8]. For the S903 airfoil it was revealed that a vortex forms on the lower surface of the airfoil behind the Gurney flap, shown in Fig. 1-5. This vortex also affects the development of unsteady forces on the airfoil when compared to those of a MiTE at $1.00c$; an example of these differences can be seen in Fig. 1-6 for the S903 airfoil with MiTEs at $0.90c$ and $1.00c$ oscillating harmonically with a reduced frequency of 0.14.

The numerical investigations by Chow and van Dam for an upstream MiTE (which they refer to as a “microtab”) on the S809 wind-turbine airfoil revealed very similar results for the flow structure [23,24], which is shown in Fig. 1-7. They also investigated the aerodynamic

response due to ramp deployments, which for this case are step functions approximated using sinusoidal deployment functions of various lengths between the retracted and deployed states; their results for the various deployment times are included as Fig. 1-8. The responses show very peculiar behavior, particularly in the lift coefficient; the change in lift is at first negative for the deployments before increasing to the eventual steady state response. Chow and van Dam recognize this behavior, but they do not investigate why it occurs. Instead, they conclude that the transients do not affect the post-deployment aerodynamic behavior [23,24]. The applicability to rotorcraft of their conclusion is not immediately apparent and deserves further investigation.

It is this behavior of the lift, drag, and pitching-moment that is of particular interest in recent efforts to develop a generalized, unsteady upstream MiTE model [29]. Previous models were found to be limited in either their applicability to upstream MiTEs [5,7] or their applicability to generalized, non-harmonic deployment schemes in the time domain [10,11]. Computational fluid dynamics is a powerful tool to support the development of this new model, as physical insights into the flow field can be gained and forces predicted without needing an expensive, time-accurate unsteady experiment.

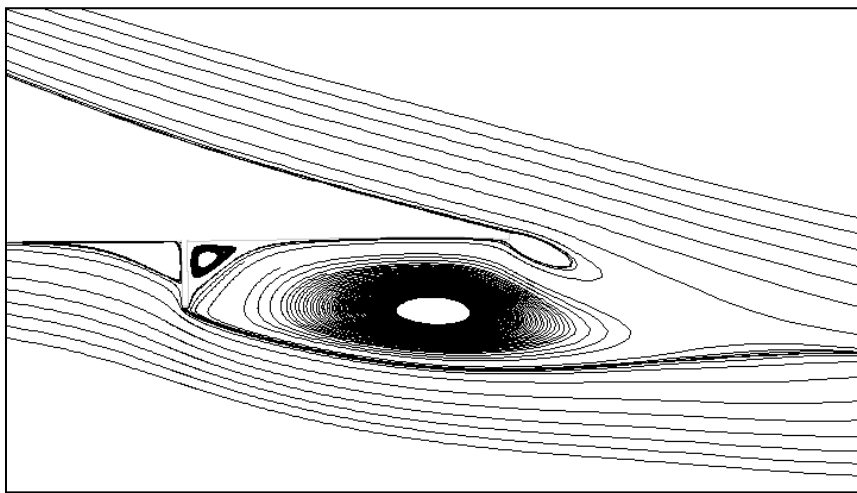


Figure 1-5. Time-averaged streamlines of an upstream Gurney flap for the S903 airfoil [5]

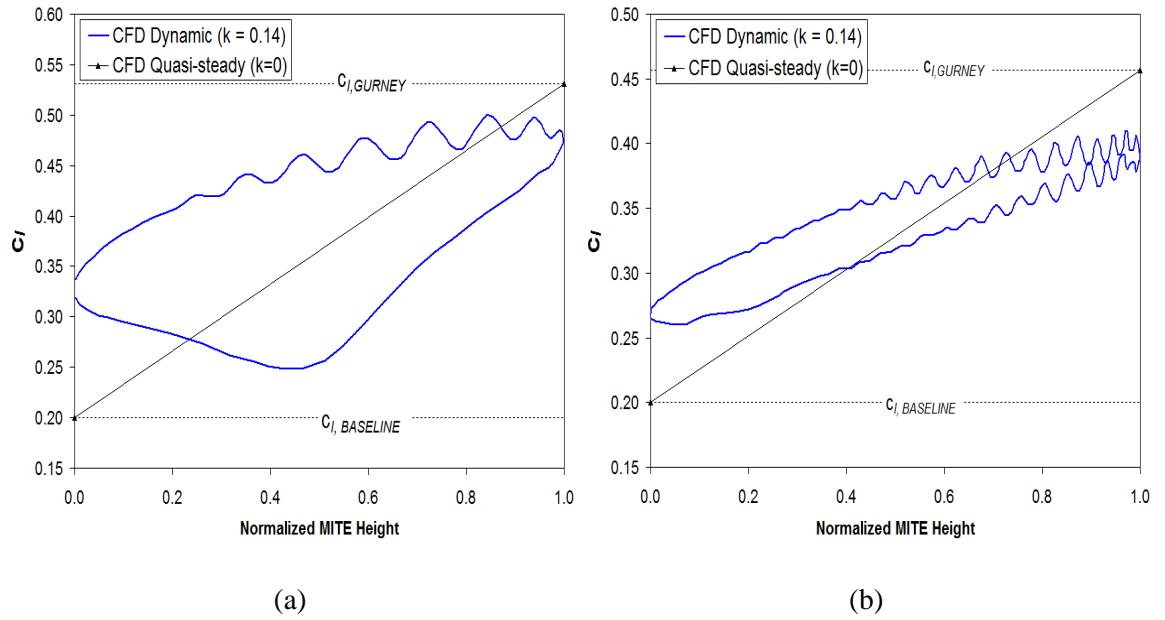


Figure 1-6. S903 airfoil with an oscillating $0.02c$ MiTE located at $0.90c$ (a) and at $1.00c$ (b), $\alpha = 0^\circ$, $M_\infty = 0.1$, $R = 1.0 \times 10^6$, and $k = 0.14$ [7]

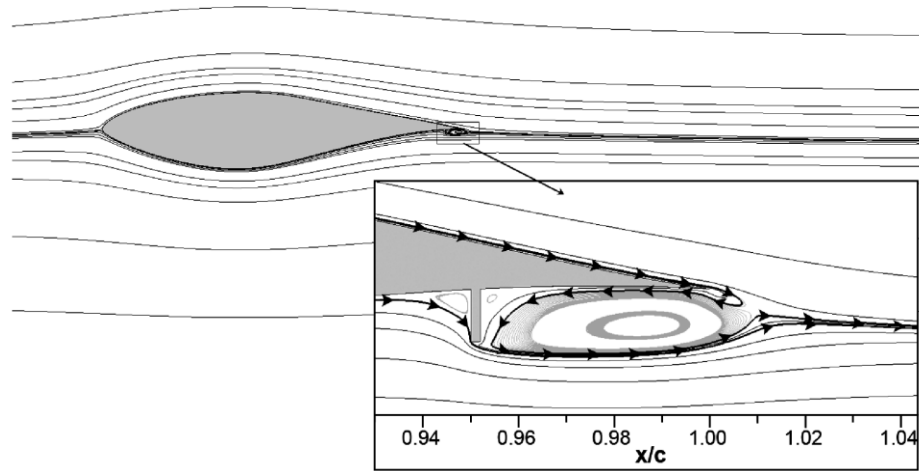


Figure 1-7. Instantaneous streamlines of an S809 airfoil with a $0.011c$ Gurney flap at $0.95c$ [23]

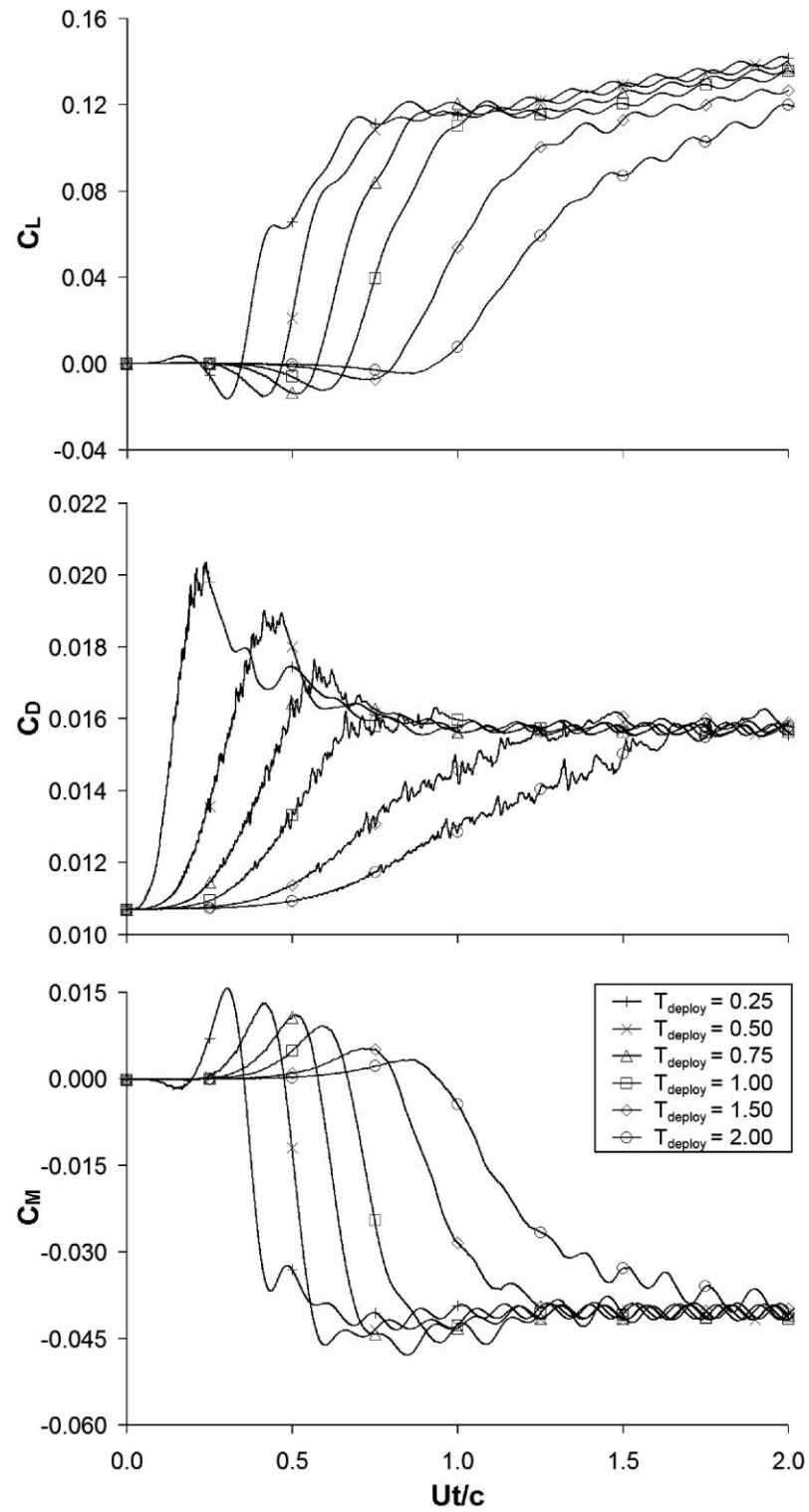


Figure 1-8. Unsteady aerodynamic responses for various MiTE deployment times on the S809 airfoil [23]

1.4 Goals

As it is beneficial to improve the fundamental understanding and the capabilities for predicting both dynamic stall and MiTE aerodynamics, the present study is divided into three components, each dependent on the previous:

1. Validate static predictions from OVERFLOW 2.1 for airfoils, both clean and with Gurney flaps
2. Assessment and validation of OVERFLOW 2.1 for predicting the onset of dynamic stall
3. Development of a database of CFD upstream MiTE predictions which are conducive to developing a generalized unsteady aerodynamic model

1.4.1 Static CFD Validation

A certain requisite for analyzing dynamic stall and MiTE aerodynamics using CFD is to first validate that the solver produces reasonable solutions and that the solution is grid independent. This will be accomplished by analyzing the S408 tilt-rotor airfoil, which has been tested in the Penn State Low-Speed, Low-Turbulence Wind Tunnel in both clean and with upstream Gurney flap configurations.

These geometries will be analyzed using OVERFLOW 2.1 to determine which surface grid resolution produces sufficient results without excessive computation time, whether the solution method is valid for this class of problem, and if the turbulence modeling produces reasonable results given the assumption of fully turbulent flow.

1.4.2 Dynamic Stall CFD Predictions

This investigation will make use of OVERFLOW 2.1 and all results will be validated against experimental data from the US Army Dynamic Stall Data Package (USADSDP) [15]. The USADSDP provides a useful set of experimental data for the Vertol VR-7 airfoil for the purpose of identifying flow physics which are not being adequately modeled by CFD. These data were originally collected by McCroskey et al. when they investigated the dynamic stall characteristics of seven rotorcraft airfoils and one supercritical fixed-wing airfoil [30,31].

Static, trailing-edge stall suppression, and double stall cases are included in the data package. Each case will be analyzed using CFD, and methods for improving the quality of predictions will be considered.

1.4.3 Upstream MiTE CFD Predictions

The primary objective of investigating MiTE aerodynamics in OVERFLOW 2.1 is to use CFD as a “virtual wind tunnel” in lieu of experimental data to identify important flow physics that influence the transient aerodynamic responses. This is to foster the development of a generalized unsteady upstream MiTE aerodynamic model based on indicial methods using the Duhamel integral [29]. While the indicial response is the basis of the method, CFD simulations of ramp deployments and oscillatory deployments are also necessary to provide validation cases for the generalized model. The predictions by Kinzel et al. [5-8] and Chow and van Dam [23,24] provide a dataset against which the CFD results can be qualitatively compared to improve confidence in the quality of the solutions.

An additional aspect of this study would be to improve the understanding of the important flow physics which influence the unsteady responses and to investigate how they affect the forces and moments produced by a MiTE in a rotor environment. It is initially believed that the decreases in lift immediately after MiTE deployment as observed by Chow and van Dam [23,24] are related and possibly equivalent to the deviations from Theodorsen-like behavior observed by Kinzel for oscillating upstream MiTEs [5-8].

Chapter 2

Description of Numerical Methods

2.1 Solvers and Solution Strategies

2.1.1 OVERFLOW 2.1

The Reynolds-averaged Navier-Stokes (RANS) solver OVERFLOW 2.1 was used as the primary analysis tool for all static and dynamic solutions. It is a structured solver and can use either single-block or Chimera-overset meshes. All grids are required to be defined in three-dimensions, however boundary conditions available in OVERFLOW 2.1 allow for the treatment of two-dimensional and axisymmetric geometries [32]. The most recent release as of the writing of this thesis, version 2.1ae, includes a variety of one- and two-equation turbulence models, but with no treatment of unforced transition. While it is possible to define trip-lines and fully-laminar regions, all cases run for the present studies were assumed to be fully turbulent. The Spalart-Allmaras (S-A) one-equation turbulence model [33] with streamline curvature corrections was used for the majority of the cases considered. The use of a hybrid RANS/Large-Eddy-Simulation (Detached Eddy Simulation, or DES) approach [35] was also examined. All cases using the S-A turbulence model were run two-dimensionally, while the DES solutions were run three-dimensionally to resolve large-scale spanwise turbulent structures.

The current investigations employ an implicit algorithm using the second-order-accurate Pulliam-Chaussee scalar pentadiagonal left-hand-side (LHS) [36] and an upwinded, second-order-accurate right-hand-side (RHS). While the Pulliam-Chaussee algorithm (which is based on the Beam-Warming algorithm [37]) favors a central-difference RHS for Courant-number

independence of the solution, this was found to be numerically unstable for some dynamic cases. The errors introduced by having an upwinded RHS and the recommended artificial dissipation were investigated and determined to be negligible compared to the flow characteristics being investigated.

All static airfoil cases without Gurney flaps were run non-time-accurate until the L2-Norm of the residuals vector converged to machine-zero. All unsteady cases as well as static Gurney flaps cases were run second-order time-accurate until the forces achieved a limit-cycle or the desired amount of simulation time was reached. Newton sub-iterations were used for all time-accurate cases to improve temporal accuracy, the number of which varied depending on the size of the time-step. Force integrations are performed using USURP [38].

These methods yielded reasonable solutions and computation times, so other numerical methods were not investigated.

2.1.2 ANSYS FLUENT 12.1

FLUENT 12.1 is an unstructured Navier-Stokes solver which is capable of both two- and three-dimensional operation [39]. While it includes a variety of turbulence models, including the Spalart-Allmaras model, this solver has garnered much attention due to its recent inclusion of the four-equation Langtry-Menter (L-M) transitional turbulence model [40-42]. While it is labeled as a four-equation turbulence model, it is more accurately described as being the SST two-equation turbulence model enhanced by the addition of two transport equations for intermittency and transition momentum-thickness Reynolds number. These additional equations allow for the prediction of transition using the local variables of the flow field and can predict natural transition and transition via a laminar separation bubble; they are described in more detail in Appendix A. This model has the potential to be a major improvement over existing one- and two-equation

turbulence models that approximate the flow field as being fully turbulent. All FLUENT 12.1 solutions are two-dimensional and were obtained using the SIMPLE scheme with second-order-accurate upwinding of all flux variables, with non-time-accurate marching initially and then implicit time-accurate marching until force convergence was achieved.

2.1.3 XFOIL 6.96

Some verification of static CFD results can be obtained by comparing the predictions with those generated by XFOIL 6.96 [43]. XFOIL is a potential-flow panel method code coupled with an integral boundary layer method. The solution iterates on the boundary-layer displacement thickness with the outer flow solution until convergence is reached. Transition is predicted using an approximate e^n -envelope method and includes the influence of laminar separation bubbles. Unlike previous studies which fixed the transition near the leading edge of the airfoil [5], all comparisons with CFD use natural transition with $n = 9$. While the underlying panel method is based on incompressible flow theory, the Karman-Tsien compressibility correction is used and provides reasonable results with increasing Mach number until the transonic drag rise. Airfoils with Gurney flaps are not analyzed with XFOIL in this study, as a working Gurney flap has significant amounts of separation which is well outside of the potential flow assumptions.

2.2 Grid Generation Software

2.2.1 Chimera Grid Tools 2.0

All overset grids used for OVERFLOW 2.1 solutions were generated using Chimera Grid Tools 2.0 [44] based on surface grid definitions generated by in-house software (described in

section 2.2.2). Chimera Grid Tools provides a graphical user interface for visually inspecting the grids and allowing the user to provide local refinements. The near-field body-fitted O-grids are generated using an implicit hyperbolic marching scheme with optional volume sub-iterations (ten sub-iterations gave high quality grids without much increase in computation time), and the far-field grids are stretched Cartesian box-grids. The wall spacing and maximum allowable stretching ratios were determined by the best practices in overset grid generation [45].

While the far-field grid completely overlays the body-fitted grid, it lacks sufficient resolution near the airfoil surface and actually includes grid points inside the airfoil itself. These superfluous far-field grid points are removed in a process referred to as hole-cutting. This is done such that the newly-defined inner boundary of the far-field grid and the outer boundary of the body-fitted grids have sufficient overlap to facilitate the overset interpolation used in the flow solver [46]. The hole-cutting is accomplished using “XRAYs,” which are defined in Chimera Grid Tools and interpreted by OVERFLOW 2.1 to cut the desired holes. These XRAYs are also able to move with a body in a dynamic simulation to allow adaptable geometries in OVERFLOW 2.1 while still preserving logically structured grids.

Hole-cutting is also required on the body-fitted grid when analyzing a MiTE, as the near-field grids of the airfoil and Gurney flap overlap and the boundary conditions become otherwise inconsistent. Since the grids and boundary conditions are logically orthogonal to each other in this case, collar grids must be introduced to ensure that there are no “leaks” in the grid.

2.2.2 Airfoil Surface Grid Generation Software

To avoid the need for CAD software to generate airfoil surface geometries, a computer code was written in the C++ language to facilitate the development of airfoil surface grids for import into Chimera Grid Tools. The code reads in a standard airfoil coordinate file, representing

a continuous curve beginning and ending at the trailing edge, and creates a piecewise cubic Hermite spline to define the surface. The user inputs the desired number of surface grid points and the grid spacing for the leading and trailing edges. A cubic distribution, which is parameterized by arc length, is then used on the upper and lower surfaces. The total arc-length is then iterated based on straight-line segments between grid points until convergence is achieved.

The user also has an option of defining the location and size of a MiTE grid to be generated for the airfoil. The normal and tangent vectors at the user-specific MiTE location are calculated from the Hermite spline, and the MiTE surface grid is defined such that its centerline is coincident with the normal vector. The collar surface grids are generated next and follow the airfoil surface before turning to become parallel to the MiTE. This guarantees that the grids properly align, even when the MiTE region of the airfoil has a large amount of surface curvature. Finally, the computer code generates grid regions that are used by Chimera Grid Tools for generating XRAYs for both the airfoil surface and the MiTE.

2.2.3 GAMBIT 2.4.6

All two-dimensional unstructured grids for FLUENT cases were generated using GAMBIT 2.4.6 [47]. This software lacks a hyperbolic field grid generation feature, and so all sides of the computational domain need to be defined before generating the field grid. The grid around the airfoil is a C-type mesh with three blocks, each populated with quadrilateral elements and extending 30 chord lengths from the surface; the use of multiple blocks facilitates high-quality mesh generation for airfoils with blunt trailing edges. The arrangement of the blocks is shown below in Fig. 2-1. While FLUENT is an unstructured solver, each block was generated as a structured mesh to ensure proper boundary-layer spacing and to control the number of elements in the field grid. As the turbulence model used in the FLUENT cases is based on the SST two-

equation model, and since a no-slip wall boundary condition is used (rather than a wall-function), the y^+ value of the first grid point was set to be less than one at approximately the 10%-chord location. While it is possible for transition to occur aft of this location for most of the lift coefficient range, the sensitivity of $c_{l,max}$ on boundary layer parameters necessitates accurate resolution at higher angles of attack.

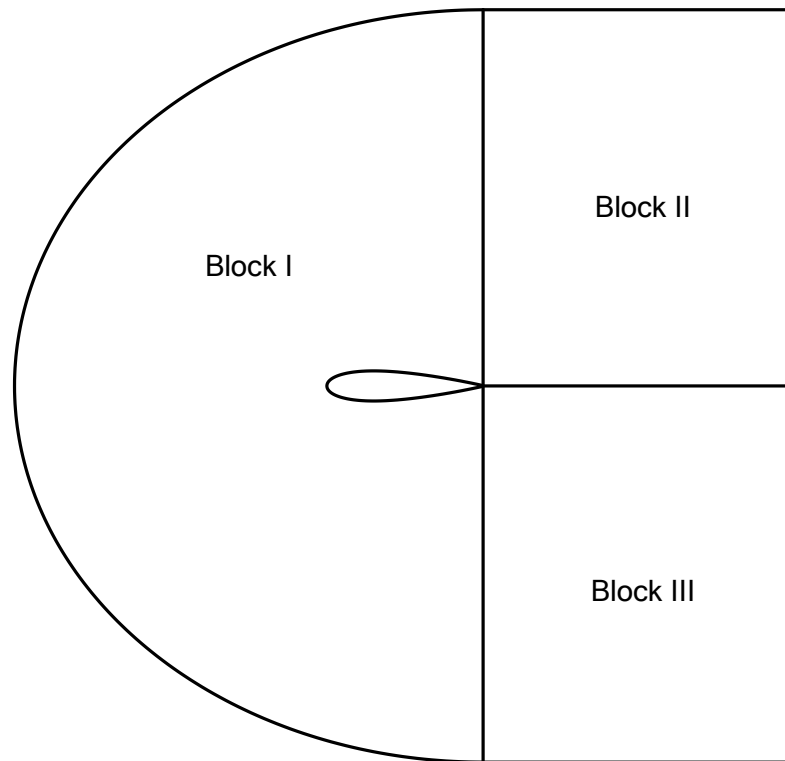


Figure 2-1. Schematic diagram of three-block C-grid

Chapter 3

Static CFD Validation

3.1 Somers S408 Airfoil

The Somers S408 airfoil is a tilt-rotor airfoil that was tested in the Penn State Low-Speed, Low-Turbulence Wind Tunnel [48]. Validation of the wind tunnel can be found in Refs. 49 and 50. The airfoil was also tested with a Gurney flap, making it an ideal choice for a grid resolution study and some static validation of the CFD methods. Due to restrictions, neither an image of the airfoil nor coordinates may be included with this thesis, although they are available from Dan Somers of Airfoils, Incorporated.

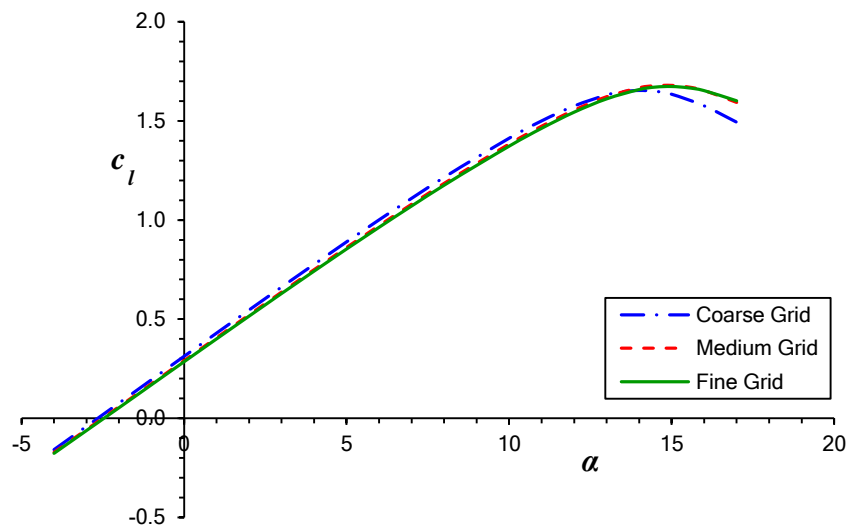
3.2 OVERFLOW 2.1 Grid Resolution Study

A surface-grid resolution study was performed on the S408 airfoil operating at $M_\infty = 0.2$ and $R = 1.50 \times 10^6$. Three near-body resolutions were considered: 225 x 100, 450 x 100, and 675 x 100 (referred to as coarse, medium, and fine, respectively). The leading- and trailing-edge spacing was chosen for the medium grid to give a maximum stretching ratio of less than 1.2, and appropriately scaled to the coarse and fine grids. As the body-fitted grid was generated so that the first off-body grid point lies at $y^+ = 1$, and the stretching ratio is ~ 1.1 (in accordance to best practices [45]), grid resolution normal to the airfoil was not varied. The Spalart-Allmaras turbulence model with streamline curvature corrections was used in the calculations for this study.

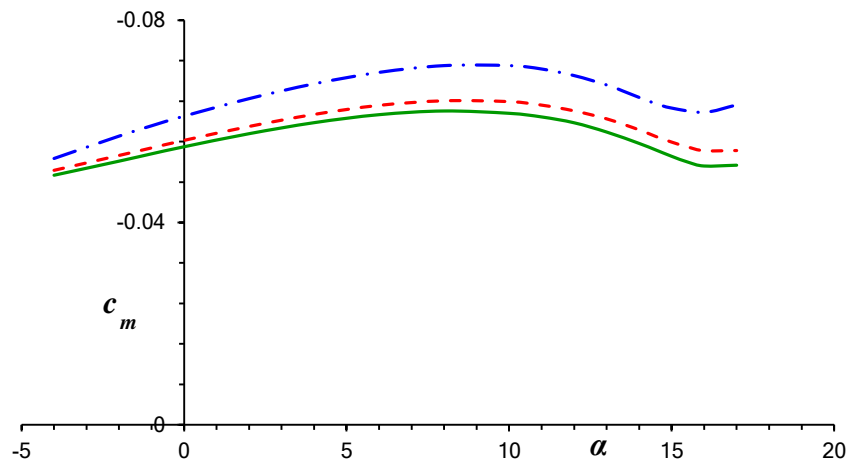
The lift, drag, and pitching-moment coefficients for each grid are plotted in Fig. 3-1, with key results listed in Table 3-1. The coarse grid shows the best agreement with experiment for maximum lift coefficient, but its solution lacks grid independence. The medium and fine grids show improvement over the coarse grid for predicting of the zero-lift angle of attack. The fine grid shows better agreement than the medium grid for maximum lift coefficient and the character of the pitching-moment coefficient, but the differences are slight. Given that the solution for the medium grid shows the beginnings of grid independence, the improvements gained by going to a finer grid do not justify the increase in computation time. Therefore all airfoil grids used for OVERFLOW solutions have a baseline resolution of ~450 surface points.

Table 3-1. Summary of key predictions for S408 grid resolution study, $R = 1.5 \times 10^6$

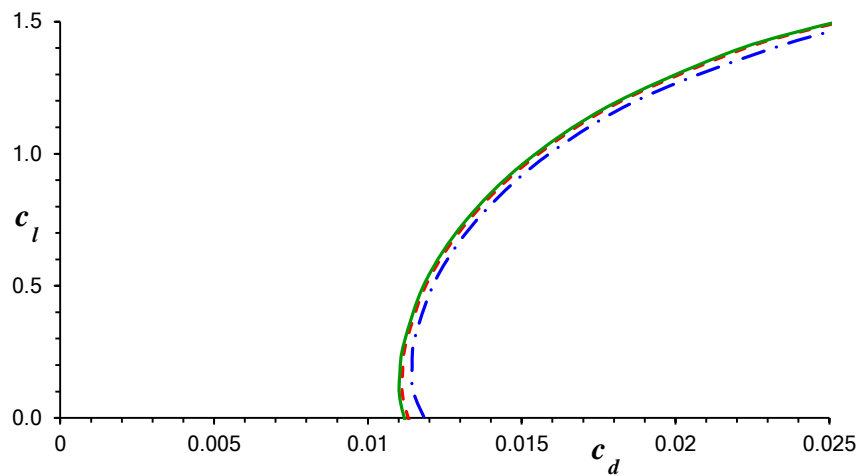
	Coarse Grid	Medium Grid	Fine Grid
α_0	-2.6566°	-2.5115°	-2.4671°
$c_{l,max}$	1.6532	1.6788	1.6731
α_{stall}	14.0°	15.0°	15.0°
$c_{m,0}$	-0.05563	-0.05251	-0.05148
$c_{d,min}$	0.01144	0.01113	0.01104



(a) Lift



(b) Pitching Moment



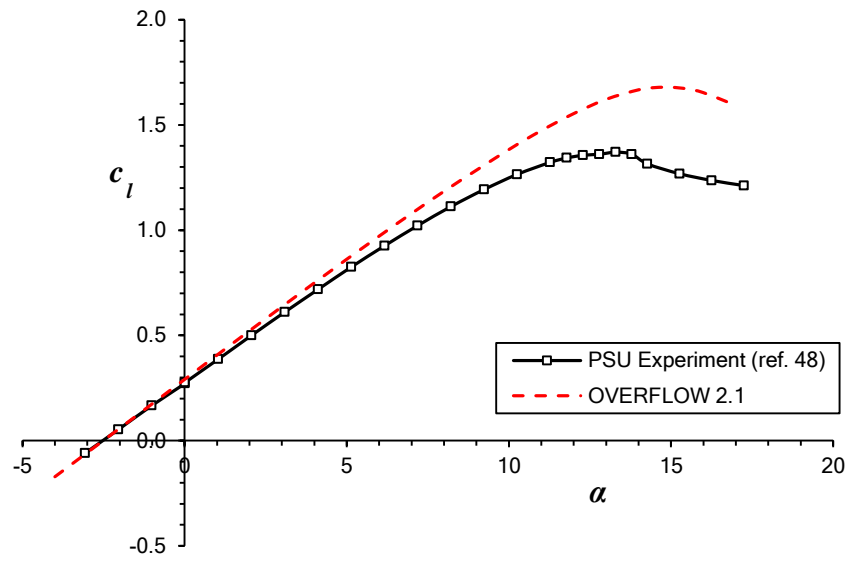
(c) Drag

Figure 3-1. S408 predictions from OVERFLOW for various grid resolutions, $R = 1.5 \times 10^6$

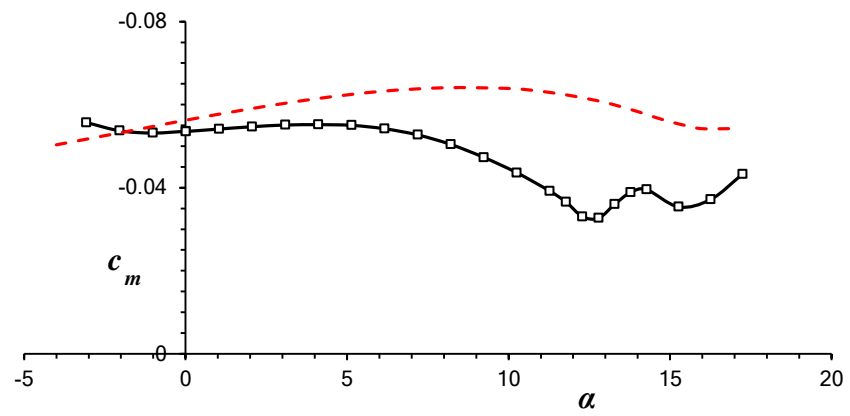
3.3 Comparison with Experiment

The predictions from the medium grid are plotted in Fig. 3-2 with experimental data from Ref. 48. There is strong agreement between CFD and the experiment in the linear region, especially with the zero-lift angle of attack and zero-lift pitching-moment coefficient. There are, however, noticeable differences in the slope of the lift curve and that the maximum lift coefficient is overpredicted by approximately 0.30. Both of these effects may be due to CFD underpredicting the amount of trailing edge separation.

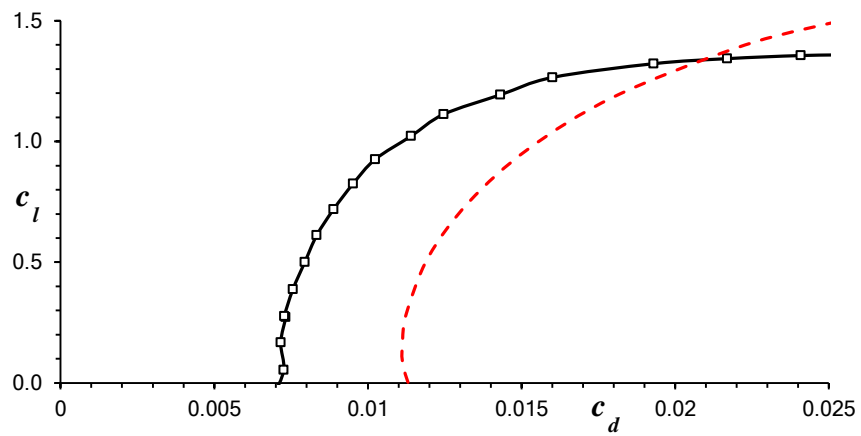
OVERFLOW also predicted significantly higher drag for the airfoil than was observed in the Penn State Low-Speed, Low-Turbulence Wind Tunnel. This is most likely attributable to the lack of transition modeling in the results obtained using CFD with the Spalart-Allmaras turbulence model. Recent investigations comparing the Spalart-Allmaras model with the Langtry-Menter four-equation transition/turbulence model have confirmed that including transition in a CFD solution can allow for much improved accuracy in predicting the drag coefficient as well as the prediction of a low-drag “laminar bucket” [51].



(a) Lift



(b) Pitching Moment



(c) Drag

Figure 3-2. S408 airfoil predictions from OVERFLOW compared with experiment for the clean configuration, $R = 1.5 \times 10^6$

3.5 Gurney Flap Predictions

The S408 airfoil was also analyzed in OVERFLOW with a 2.38%-chord Gurney flap located upstream at 90% chord; these results are presented in Figs. 3-3 and 3-4, along with the experimental data for the same configuration obtained in the Penn State University wind tunnel. OVERFLOW captures the change in lift very well through the linear region of the lift curve, but it deviates somewhat at higher lift coefficients and overpredicts the maximum lift coefficient by approximately 0.23. Considering that the OVERFLOW results for the clean configuration overpredicts the maximum lift coefficient by approximately 0.30, the prediction of $\Delta c_{l,max}$ to within 0.07 shows that the CFD predictions are reasonable and consistent. An interesting aspect of these results is that with a Gurney flap, OVERFLOW shows excellent agreement with experiment for pitching-moment coefficient, whereas there was little agreement for the clean configuration. The improvement in the pitching-moment predictions is likely due to OVERFLOW more accurately predicting the lower-surface separation location with a Gurney flap. In the clean configuration, the separation point is strongly influenced by the boundary layer development, whereas flow separation around a Gurney flap is relatively insensitive to the boundary layer properties.

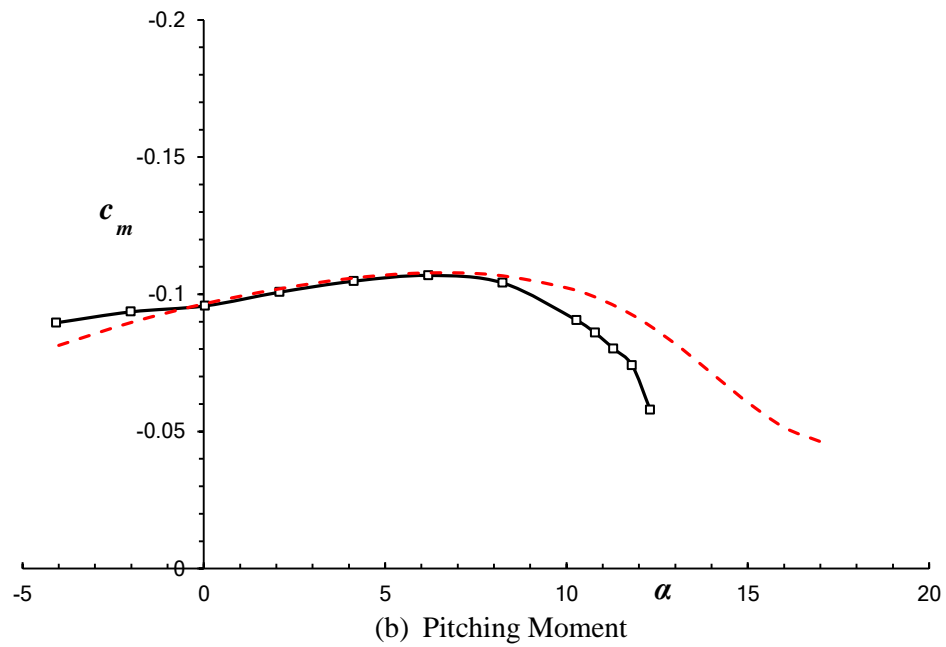
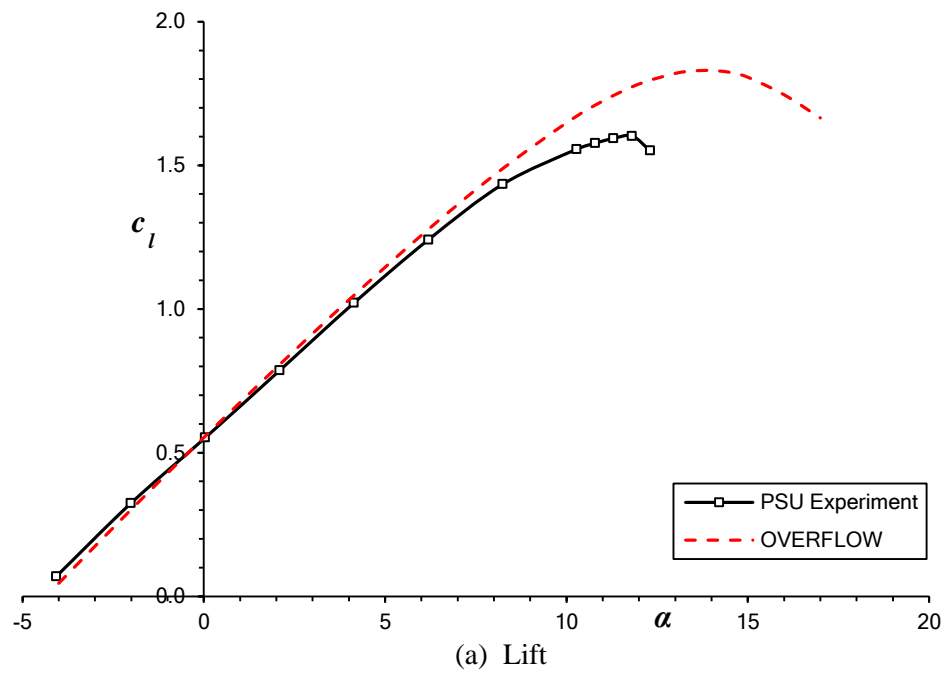


Figure 3-3. S408 airfoil with a $0.0238c$ Gurney flap at $0.90c$ predictions from OVERFLOW compared with experiment, $R = 1.5 \times 10^6$

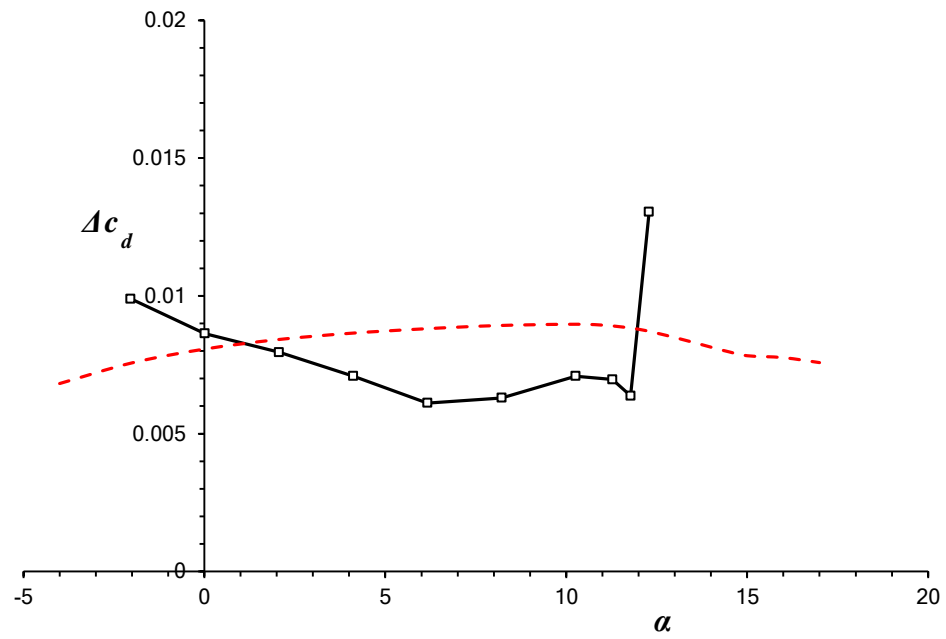


Figure 3-4. Change in drag coefficient of the S408 with 0.0238c Gurney flap at 0.90c from a clean configuration predicted by OVERFLOW and compared with experiment, $R = 1.5 \times 10^6$

3.6 Somers S903 Airfoil

Additional static validation was performed using the Somers S903 wind-turbine airfoil [52], shown in Fig. 3-5, as high-quality experimental data is available for both the clean configuration and with a 2.08%-chord Gurney flap located upstream at 90% chord [28]. The grid was generated using the techniques described previously along with a surface grid resolution in accordance with the results of the grid study. The OVERFLOW predictions for lift, drag, and pitching moment are compared with experimental data in Fig. 3-6.

For both configurations, OVERFLOW does very well in predicting the zero-lift angles of attack and the zero-lift pitching-moment coefficients. The slope of the lift curves are also captured reasonably well at lower lift coefficients, but OVERFLOW does not capture the change in the lift curve slope for the clean configuration above an angle of attack of 6 degrees.

OVERFLOW overpredicts the maximum lift coefficient by approximately 0.04 for the clean configuration, which is surprisingly accurate. This improved accuracy may be due to the S903 being designed to have a maximum lift coefficient that is insensitive to roughness, and so the fully turbulent assumption in the CFD does not break down as noticeably. When a Gurney flap is applied, however, the maximum lift coefficient is overpredicted by 0.13 compared to experiment. As a result, OVERFLOW does not do a good job capturing the change in maximum lift coefficient due to an upstream Gurney flap being applied to this airfoil.

The pitching-moment coefficient shows reasonable agreement between CFD and experiment at pre-stall angles of attack. As was true for the S408 study, better agreement is obtained for the Gurney flap configuration than for the baseline airfoil.

The drag coefficients were significantly overpredicted by OVERFLOW for both configurations, but that was an expected result of the fully turbulent assumption. For lift

coefficients corresponding to the linear region of both lift curves, OVERFLOW does rather well in predicting the change in drag coefficient due to a Gurney flap.

Further validation of this case was achieved by investigating the flow field around the airfoil, in both the clean and Gurney flapped configurations. Figure 3-7 shows the streamlines around the airfoil in both configurations from the OVERFLOW solutions at 4 degrees angle of attack. These results are consistent with the expected flow field around an airfoil; the stagnation point is in a reasonable location and the Kutta condition is satisfied for the clean airfoil. The off-body Kutta induced by the Gurney flap is evident in Fig. 3-7(b), but can be seen more clearly in Fig. 3-8. The flow field near the Gurney flap shown in Fig. 3-8 is consistent with Kinzel's predictions, which have been shown previously as Fig. 1-5 [5]. It can be concluded from this that the methods used in OVERFLOW for this investigation can adequately predict not just the integrated quantities, but also the flow field around an airfoil.

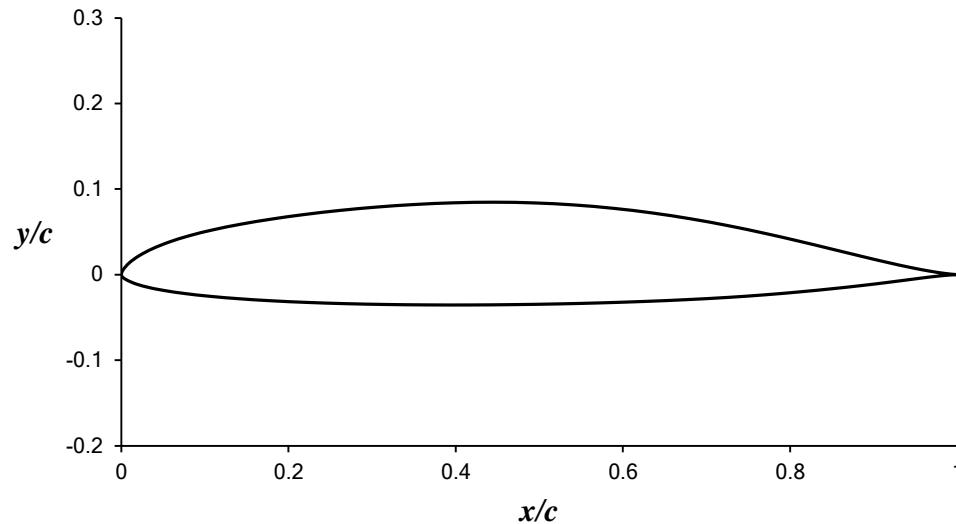
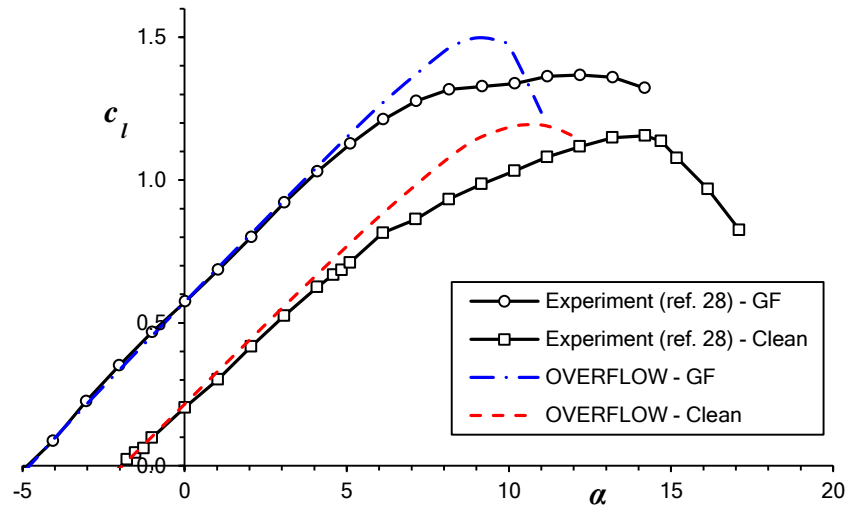
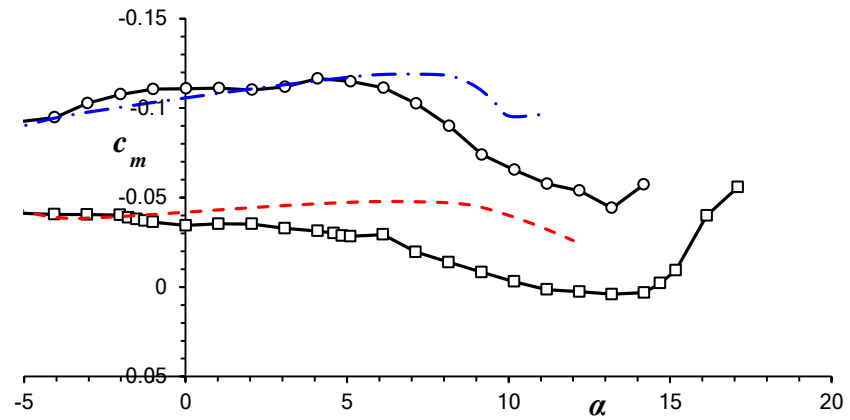


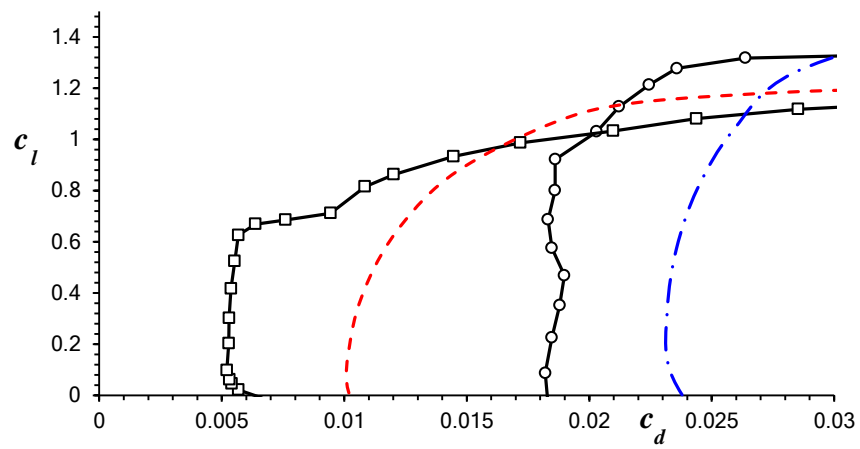
Figure 3-5. Somers S903 airfoil geometry [52]



(a) Lift

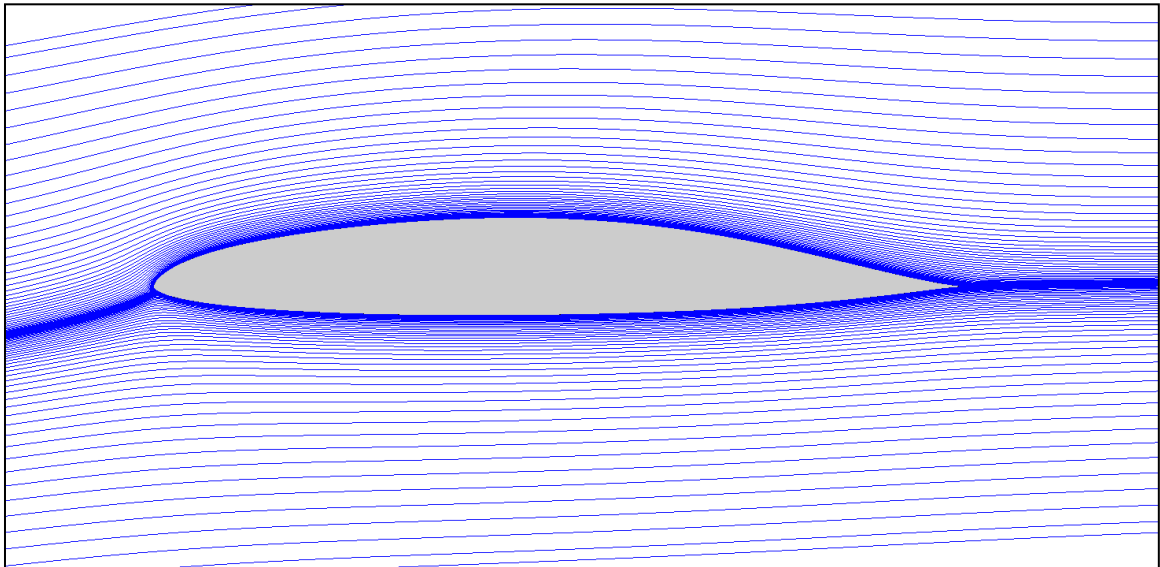


(b) Pitching Moment

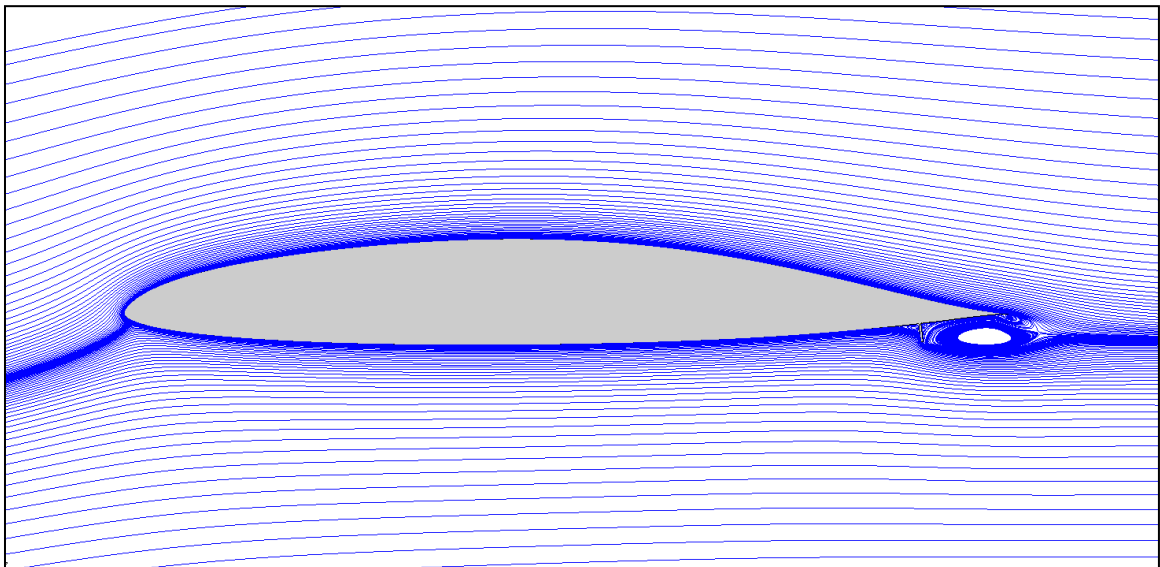


(c) Drag

Figure 3-6. S903 airfoil with a $0.0208c$ Gurney flap at $0.90c$ predictions from OVERFLOW compared with experiment, $R = 1.0 \times 10^6$



(a) Clean



(b) Upstream Gurney Flap

Figure 3-7. Comparison of time-averaged streamlines for the S903 airfoil in both clean (a) and 0.0208c Gurney flap at 0.90c (b) configurations, $\alpha = 4^\circ$, $R = 1.0 \times 10^6$, $M_\infty = 0.2$

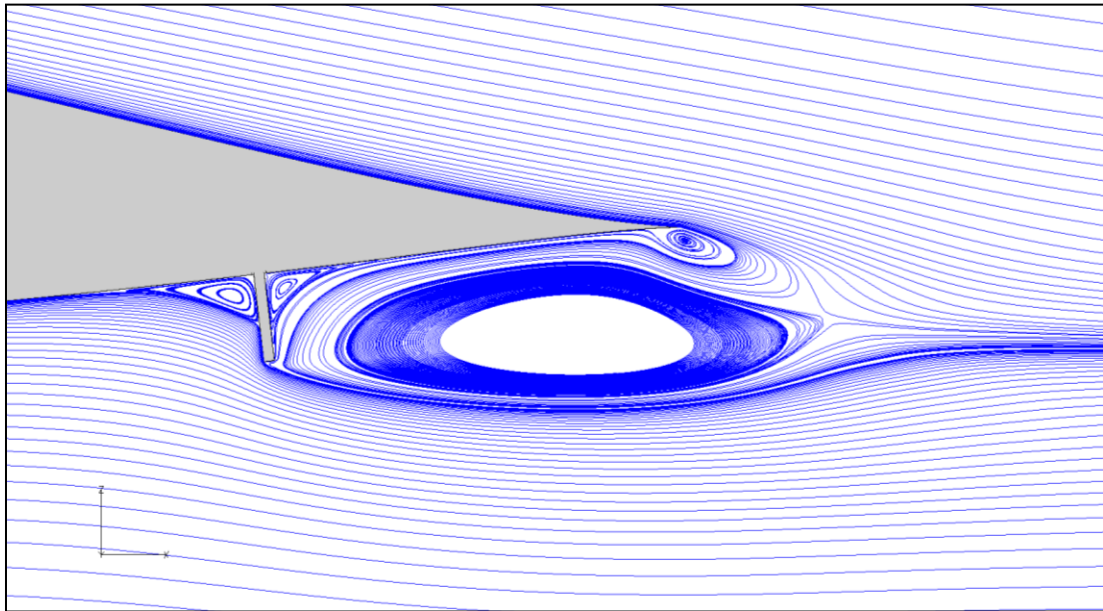


Figure 3-8. Close-up of time-averaged streamlines near a $0.0208c$ Gurney flap upstream at $0.90c$ on the S903 airfoil, $\alpha = 4^\circ$, $R = 1.0 \times 10^6$, $M_\infty = 0.2$

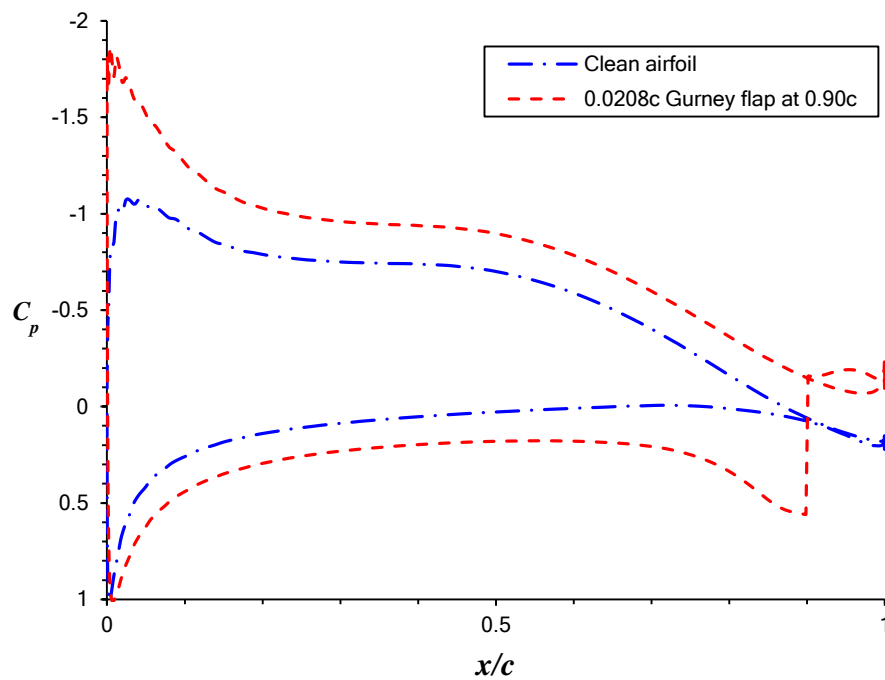


Figure 3-9. Pressure distributions for the S903 airfoil for clean and $0.0208c$ Gurney flap at $0.90c$ configuration, $\alpha = 4^\circ$, $R = 1.0 \times 10^6$, $M_\infty = 0.2$

3.7 Assessment of Results

Considering that dynamic stall studies usually do not incorporate an accurate profile drag prediction, and that Gurney flap studies tend to focus on the changes in drag associated due to flap deflection, the differences in predicted and observed drag coefficient due to the fully-turbulent approximation are therefore considered to be an acceptable error for this study. The overprediction of the maximum lift coefficient for a clean airfoil is somewhat of concern, as it is a key component of dynamic stall predictions, but this will be addressed in the next chapter.

The flow physics that govern a working Gurney flap involve flow separating around a flat plate placed normal to the local flow velocities, thereby changing the outer flow. Thus, one would expect that a sufficiently tall Gurney flap, such as the 2.38%- and 2.08%-chord flaps used in the static studies, would be relatively insensitive to the details of the boundary layer development and the presence of laminar-turbulent transition. This would imply that a fully-turbulent CFD solution would give reasonably good predictions for the changes in the aerodynamic coefficients due to an upstream MiTE, even if the baseline, clean solution has errors in the drag and maximum lift coefficient. Given that the OVERFLOW solution showed good agreement for the change in lift coefficient and the total pitching-moment coefficient with an upstream Gurney flap, the approach used for the grid generation and the solution techniques are considered to be sufficient for this study.

Chapter 4

Dynamic Stall CFD Predictions

The ability of OVERFLOW 2.1 to predict the dynamic stall characteristics of the Vertol VR-7 airfoil was investigated for three types of cases, static, trailing-edge stall suppression, and double stall, at nominal baseline operating conditions of $M_\infty = 0.184$ and $R = 2.56 \times 10^6$. The USADSDP also includes select cases at $M_\infty = 0.3$, however these cases were not considered in the present study.

4.1 Vertol VR-7 Airfoil

The airfoil geometry as tested in the U.S. Army Aeromechanics Laboratory 2- by 3-meter wind tunnel [15,30,31] is shown in Fig. 4-1, and coordinates are included in Appendix B. Aspects of the corresponding overset grid for OVERFLOW cases are depicted in Fig. 4-2.

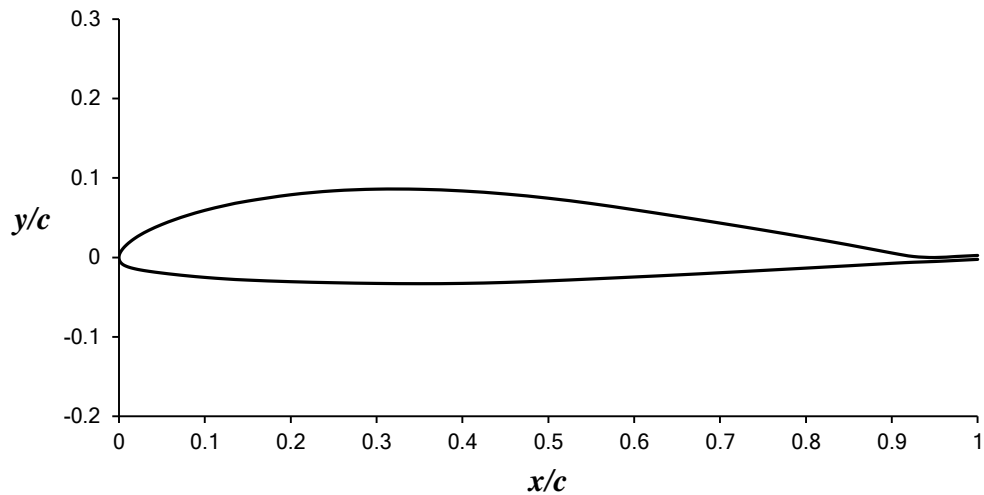
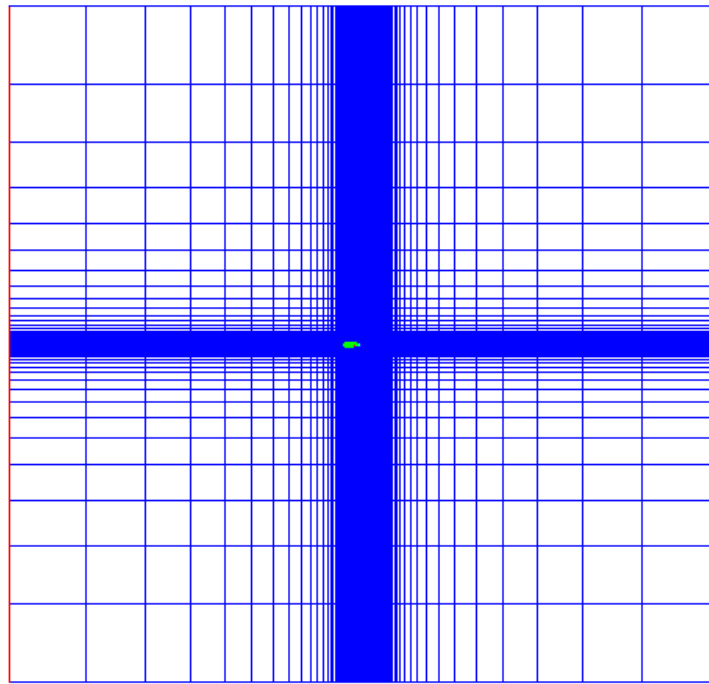
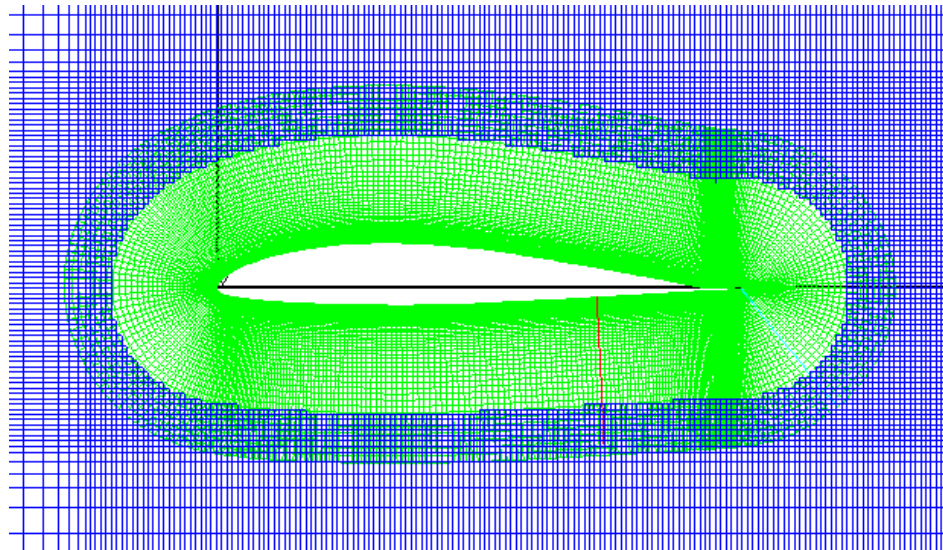


Figure 4-1. Vertol VR-7 airfoil geometry.



(a)



(b)

Figure 4-2. Far-field stretched Cartesian (a) and near-field body-fitted O-type (b) overset grids for VR-7 dynamic stall cases in OVERFLOW 2.1

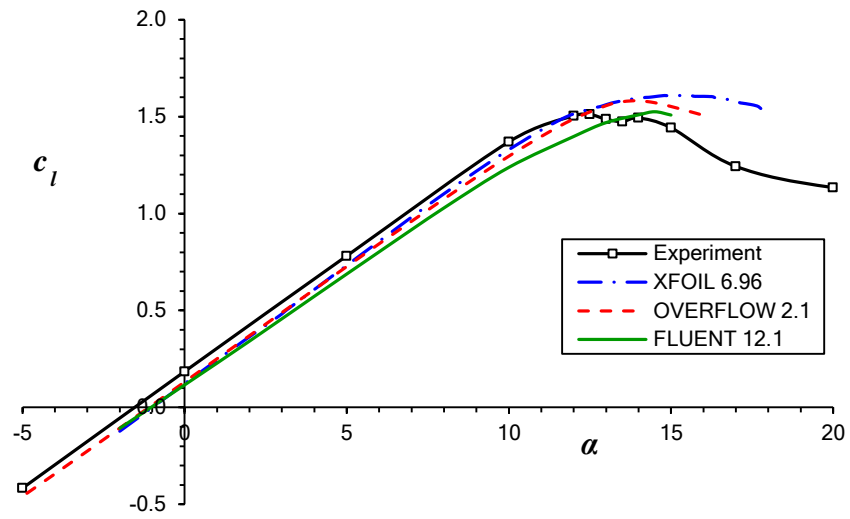
4.2 Static Predictions

The static aerodynamic characteristics of the VR-7 airfoil at the baseline operating conditions, $M_\infty = 0.184$ and $R = 2.56 \times 10^6$, were first considered as a way to validate the grid and solution techniques used with OVERFLOW 2.1. These data are compared in Fig. 4-3, along with theoretical predictions at the same conditions from FLUENT 12.1, XFOIL 6.96, and the experimental results from the USADSDP [15]. The OVERFLOW results use the S-A turbulence model while the FLUENT solution uses the L-M turbulence model.

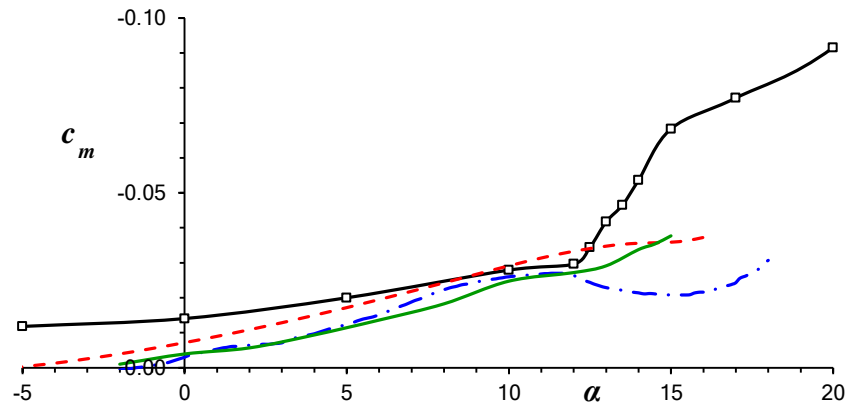
Experimentally obtained drag coefficients are not included in Fig. 4-3, as only the pressure drags were measured. All three theoretical methods overpredict $c_{l,max}$ compared to experiment, with FLUENT showing the best agreement. It is peculiar to note, however, that both CFD methods and XFOIL show reasonable agreement with each other for the zero-lift angle of attack, but differ somewhat from the experimental result. None of the codes show strong agreement with experiment for predicting pitching-moment coefficients, but FLUENT and XFOIL show qualitative agreement with each other. While FLUENT was better able to predict the maximum lift coefficient of the VR-7, this could be the result of a variety of factors ranging use of a transitional turbulence model to the solution scheme. An overview of the key results is presented in Table 4-1.

Table 4-1. Summary of CFD and XFOIL theoretical predictions compared with experiment for VR-7 airfoil, $M_\infty = 0.184$, $R = 2.56 \times 10^6$

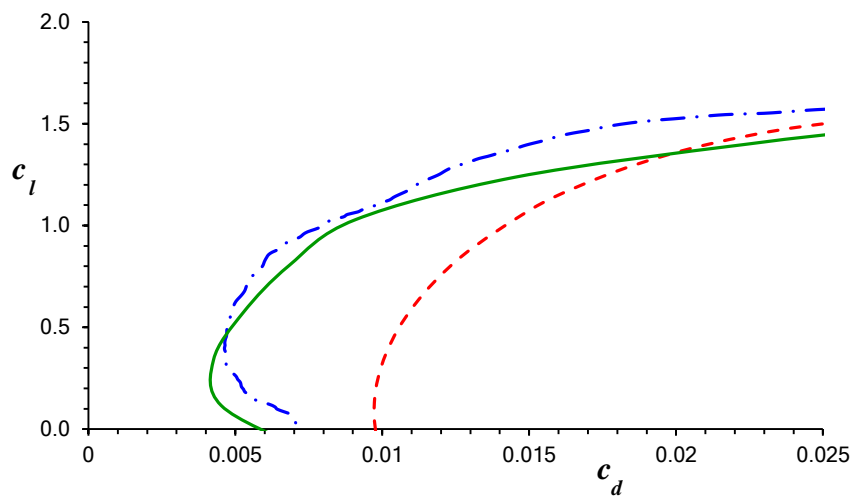
Case	α_0	$c_{l,max}$	α_{stall}	$c_{m,0}$
Experiment [15]	-1.538°	1.511	12.5°	-0.01336
OVERFLOW 2.1	-1.103°	1.582	14°	-0.00539
FLUENT 12.1	-1.037°	1.525	14.5°	-0.00241
XFOIL 6.96	-0.993°	1.611	15.5°	-0.00061



(a) Lift



(b) Pitching Moment



(c) Drag

Figure 4-3. Comparison of CFD, XFOIL, and experimental [15] predictions for the VR-7 airfoil at $M_\infty = 0.184$, $R = 2.56 \times 10^6$

4.3 Quasi-Steady Scaling

4.3.1 Lift Scaling

While the results from OVERFLOW are consistent with those obtained using other theoretical methods, they do not match the experiment in zero-lift angle of attack or maximum lift coefficient. This has major implications when performing an unsteady analysis. Even for attached flow, the lift coefficients for a given angle of attack range and reduced frequency would not be expected to match. For a dynamic stall case, post-stall conditions for an experimental case may be pre-stall in the CFD simulation, which would drastically alter the unsteady characteristics. Thus, it is unwise to rely purely on CFD to predict the onset of dynamic stall.

To account for these differences, the following quasi-steady scaling of lift coefficient and angle of attack are proposed:

$$\alpha' = \frac{\alpha - \alpha_0}{\alpha_{stall} - \alpha_0} \quad 4.1$$

$$c_l' = \frac{c_l}{c_{l,max,static}} \quad 4.2$$

This is similar to a method of accounting for compressibility effects for Gurney flapped airfoils [5,7], except that this scaling is meant to account for differences in predicting viscous effects at a given Reynolds and Mach number.

To apply these scaling factors to a CFD simulation, one first needs to have a reliable prediction of the zero-lift angle of attack, stall angle of attack, and static maximum lift coefficient, such as those obtained from a static experiment. For a given physical angle of attack range of an unsteady oscillation, Eq. 4.1 can be used to calculate the equivalent scaled angle of attack range. Next, static CFD predictions are required to determine the theoretical zero-lift angle of attack, stall angle of attack, and maximum lift coefficient. Then the α' range for the desired

conditions can be substituted into Eq. 4.1, with the computationally-obtained α_0 and α_{stall} used as the parameters to determine the physical angle of attack range for the CFD solution. Once the unsteady CFD solution is obtained at same reduced frequency, the computationally-predicted lift coefficients must be scaled by Eq. 4.2 with the computational static maximum lift coefficient. The entire process can then be inverted by multiplying the scaled lift coefficients by the experimental static maximum lift coefficient and redefining the angle of attack range to the original, desired range.

In a mathematical sense this scaling can be thought of as a mapping of one solution to another. The lift curves for practical airfoils all follow the same qualitative shape and nearly identical slopes in the linear region, varying quantitatively only by the zero-lift angle of attack and maximum lift coefficient [53]. Thus it is reasonable to assume that accurate predictions are possible through a mapping of only those two parameters.

In a physical sense, the quasi-steady scaling is a way to adjust for the differences in the actual amount of trailing edge separation and the predicted amounts. As stated earlier, one of the limitations in most CFD turbulence models is that they assume the flow to be fully turbulent. This results in a completely different behavior in the boundary layer growth than would be experimentally observed, even if the boundary layer is tripped at the stagnation point. At transitional Reynolds numbers, such as that used in the baseline static case, there is no reason to expect that the boundary layer characteristics at the trailing-edge in the experiment would be the same as those predicted by OVERFLOW.

4.3.2 Moment Scaling

At this time there has been no investigation into using a similar scaling for pitching-moment predictions. Unlike the lift curve, the mapping of the pitching-moment coefficient from

one dataset to another is not straightforward, as the curves have limited linearity and drastically different post-stall behavior. As was seen in Fig. 4-3, there is no agreement between the theoretical methods or experiment on whether the pitching moment should increase or decrease after stall. The present study therefore makes no adjustment to the pitching-moment coefficients obtained from CFD cases based on the scaled angle of attack.

4.4 Trailing-Edge Stall Suppression

The first set of dynamic stall cases considered for comparison of theory and experiment focus on trailing-edge stall suppression, which are cases where the maximum angle of attack is only a few degrees past stall. For the VR-7 cases included in the USADSDP, the angle of attack range is $4.55^\circ \pm 10.05^\circ$, which has a maximum approximately two degrees past stall. At lower reduced frequencies the airfoil experiences dynamic stall, but as the frequency increases the amount of stall is reduced and the airfoil exhibits attached flow behavior [15,31]. This effect is due to the lags in the boundary layer development increasing with reduced frequency.

Figures 4-4 through 4-7 show comparisons of the experimental data from the USADSDP with predictions obtained from OVERFLOW. In all plots, two types of numerical predictions are presented. The first, labeled as “unscaled,” matches the reported angle of attack and reduced frequency from the experiment. The second, labeled as “scaled,” follows the procedure outlined in Section 4.3 and plots the resulting equivalent lift coefficients and the raw pitching-moment coefficients versus the equivalent angle of attack.

The predictions for the lowest reduced frequency considered, $k = 0.01$, are plotted in Fig. 4-4 along with the experimental results. The unscaled results significantly overpredict the maximum lift coefficient and fail to match the predominant behavior of the dynamic stall. There is also no evidence of stalling behavior in the pitching-moment coefficient. The scaled results

show significant improvement in the lift coefficient predictions. While the pitching-moment coefficient still does not show significant stall behavior, the curve at least changes character in this region. This is most likely due to the differences observed in the post-stall behavior between experiment and CFD. Within that, it is possible that three-dimensional post-stall flow effects dominate the experimental pressure distribution, which is not modeled by two-dimensional CFD.

The next highest reduced frequency considered is $k = 0.025$, the results for which are shown in Fig. 4-5. These data show very similar behavior to what was observed for $k = 0.01$ and the same qualitative improvement is gained from the scaled predictions over the unscaled predictions.

Increasing the reduced frequency to $k = 0.1$ begins to reveal deficiencies in the computational methods for predicting dynamic stall, which can be seen in Fig. 4-6. The experiment still exhibits the dynamic stall loop, but the unscaled predictions completely miss this behavior and underpredict the maximum lift coefficient. The scaled predictions show a very small dynamic stall hysteresis loop, but $c_{l,max}$ is still underpredicted. The quality of the improvement gained by the quasi-steady scaling appears to be worse than at lower frequencies, as the lift during the upstroke is no longer accurately predicted. The pitching-moment coefficients, however, show reasonably good agreement considering the differences in the static predictions.

The final trailing-edge stall suppression case, run at $k = 0.25$, is shown in Fig. 4-7. Neither the scaled nor the unscaled OVERFLOW predictions show good agreement with experiment for lift coefficient. It should be noted, however, that the error in predicting the maximum lift coefficient is still reduced by using the scaled approach. The pitching-moment coefficient predictions show reasonably good agreement, but at this point the solution is behaving almost entirely as attached flow.

The quantitative improvement in lift predictions obtained by using the quasi-steady scaling are depicted graphically in Figs. 4-8 and 4-9. The maximum lift coefficient is predicted

more accurately by the scaled approach at every angle of attack. Improvement is also gained in predicting the angle of attack associated with $c_{l,max}$ at lower reduced frequencies, while both scaled and unscaled predictions yielded similar errors at higher frequencies.

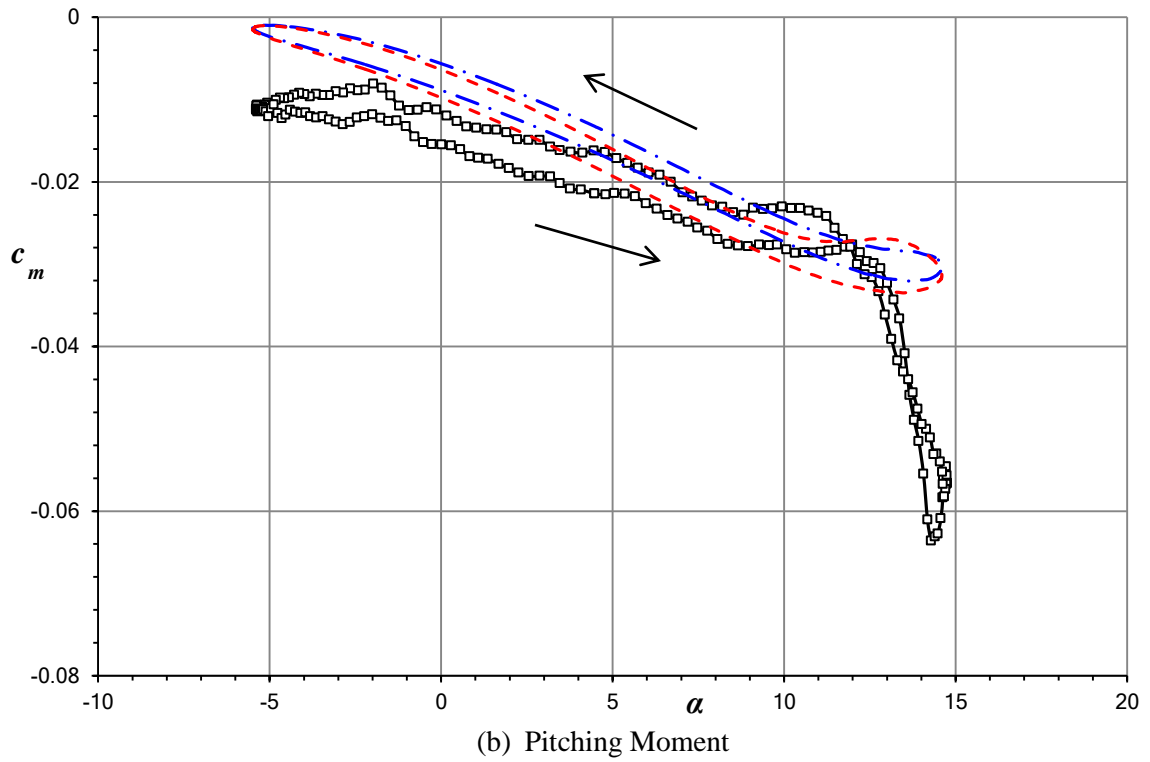
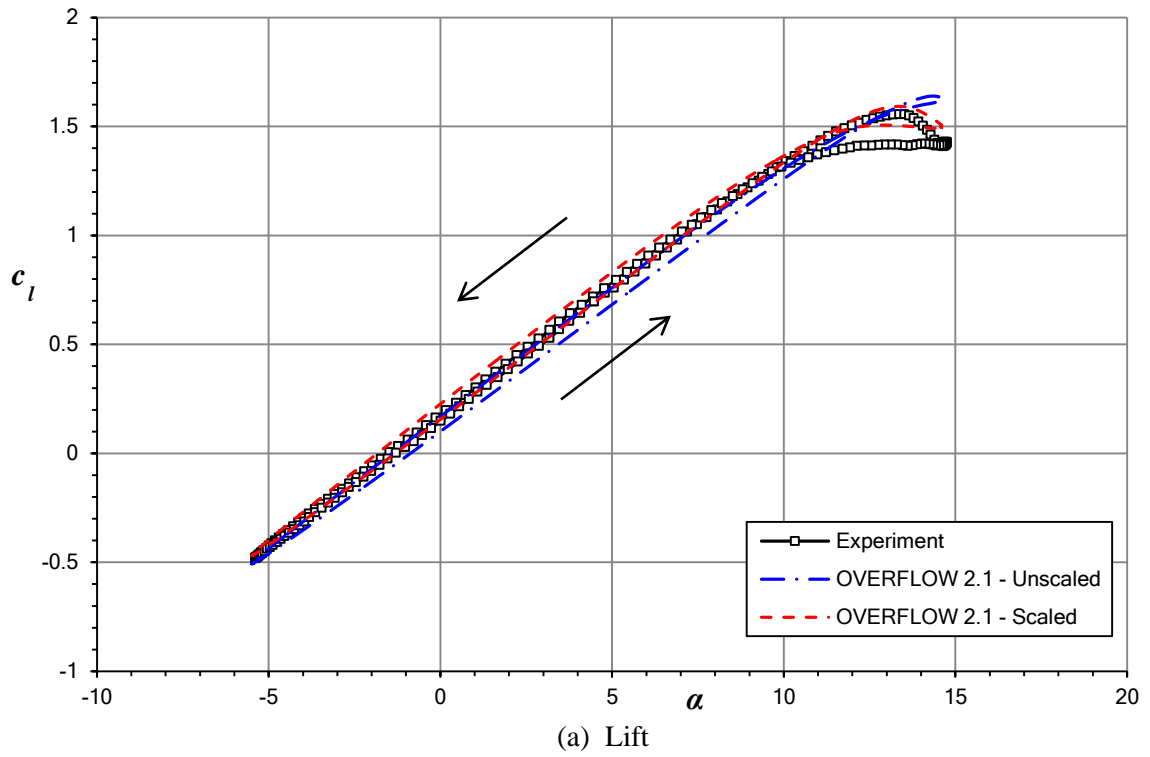


Figure 4-4. Dynamic stall predictions for the VR-7 compared with experiment [15] at $M_\infty = 0.184$, $R = 2.56 \times 10^6$, $\alpha = 4.55^\circ \pm 10.05^\circ$, and $k = 0.01$

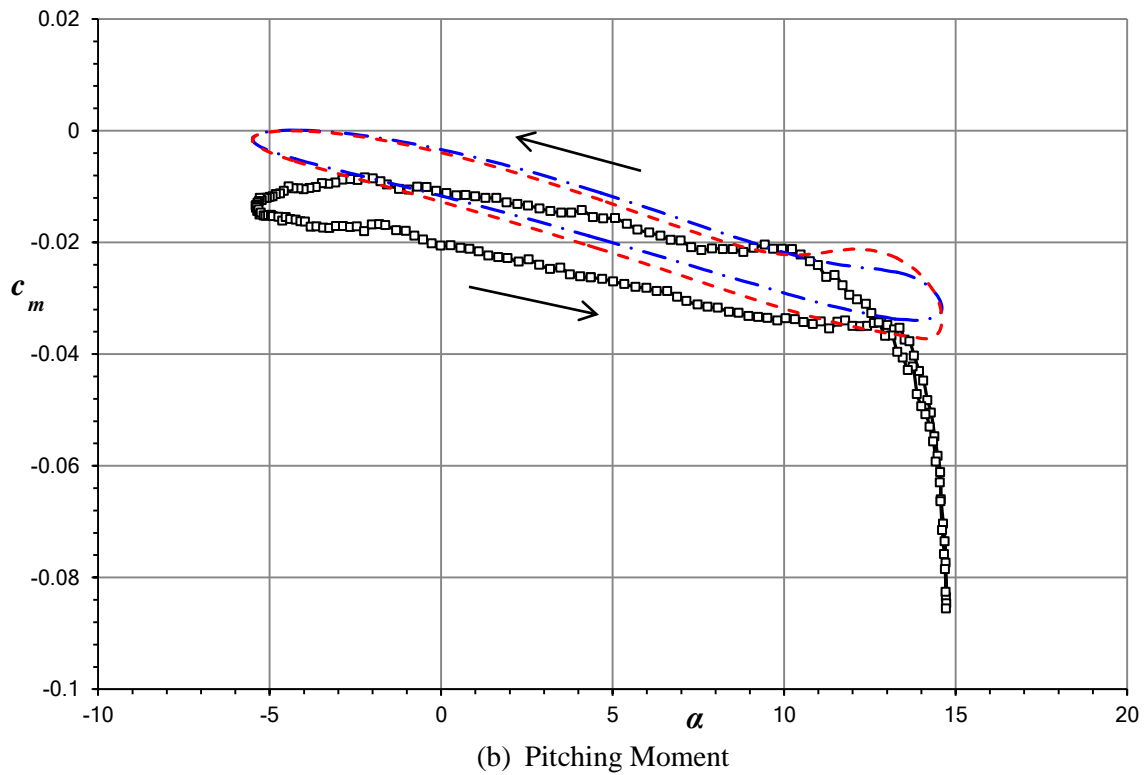
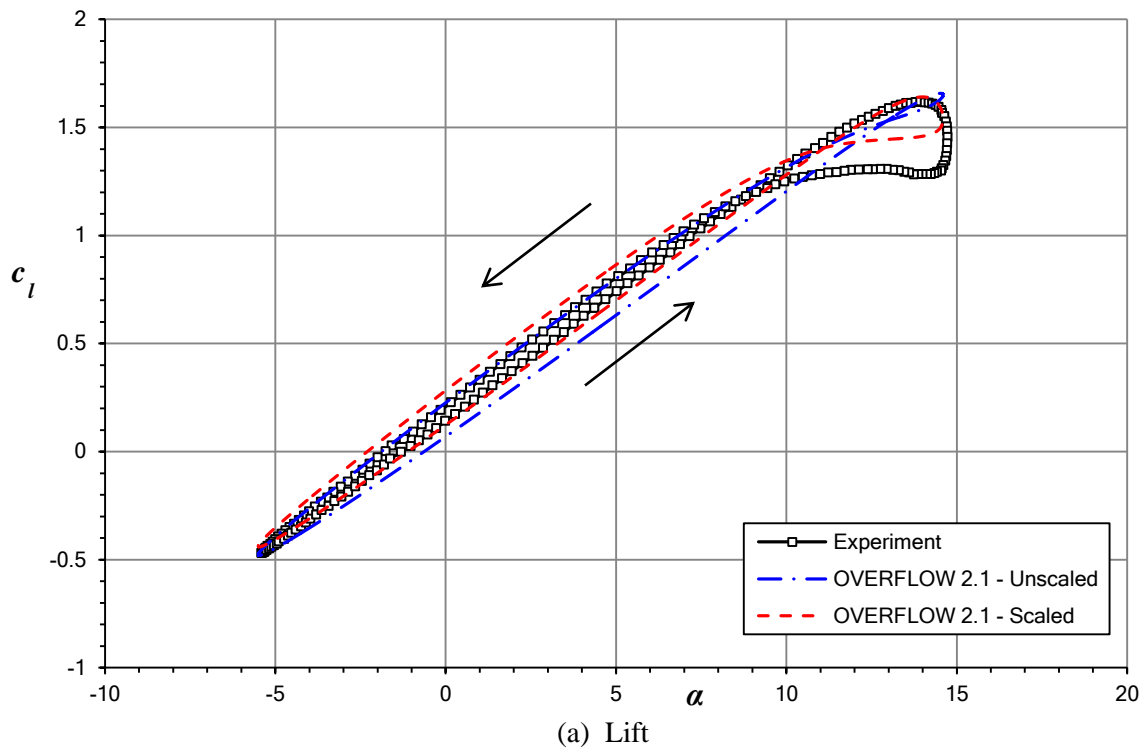


Figure 4-5. Dynamic stall predictions for the VR-7 compared with experiment [15] at $M_\infty = 0.184$, $R = 2.56 \times 10^6$, $\alpha = 4.55^\circ \pm 10.05^\circ$, and $k = 0.025$

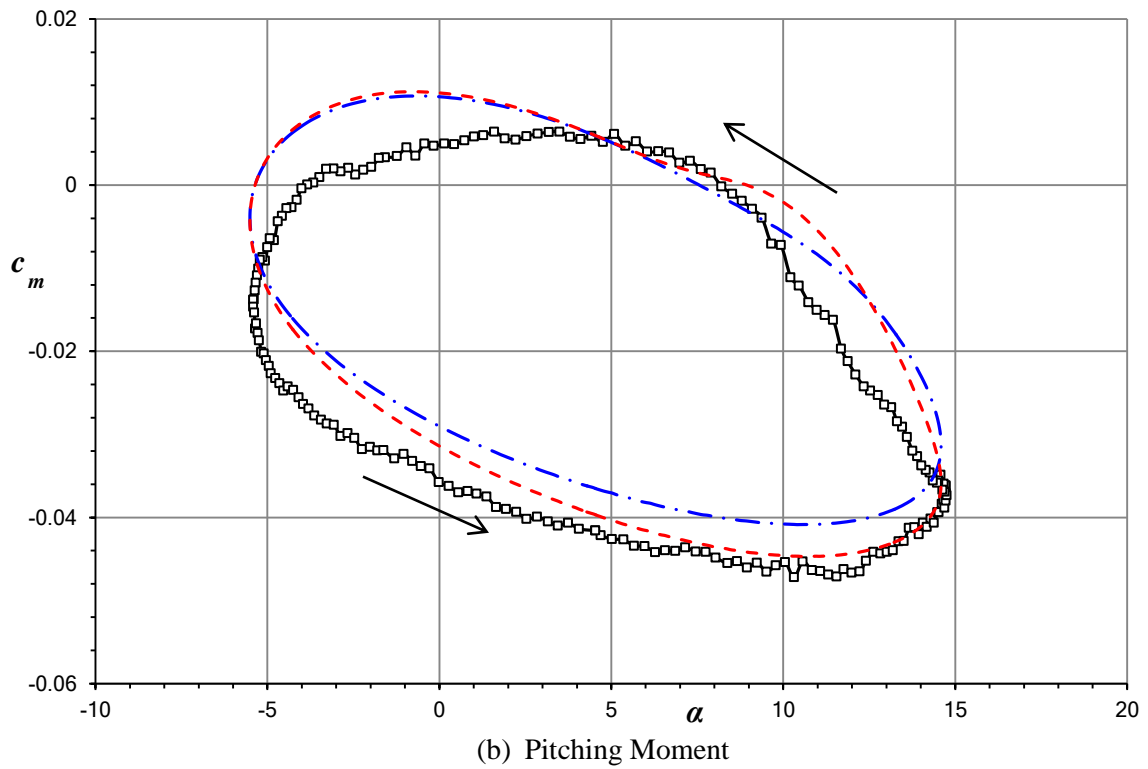
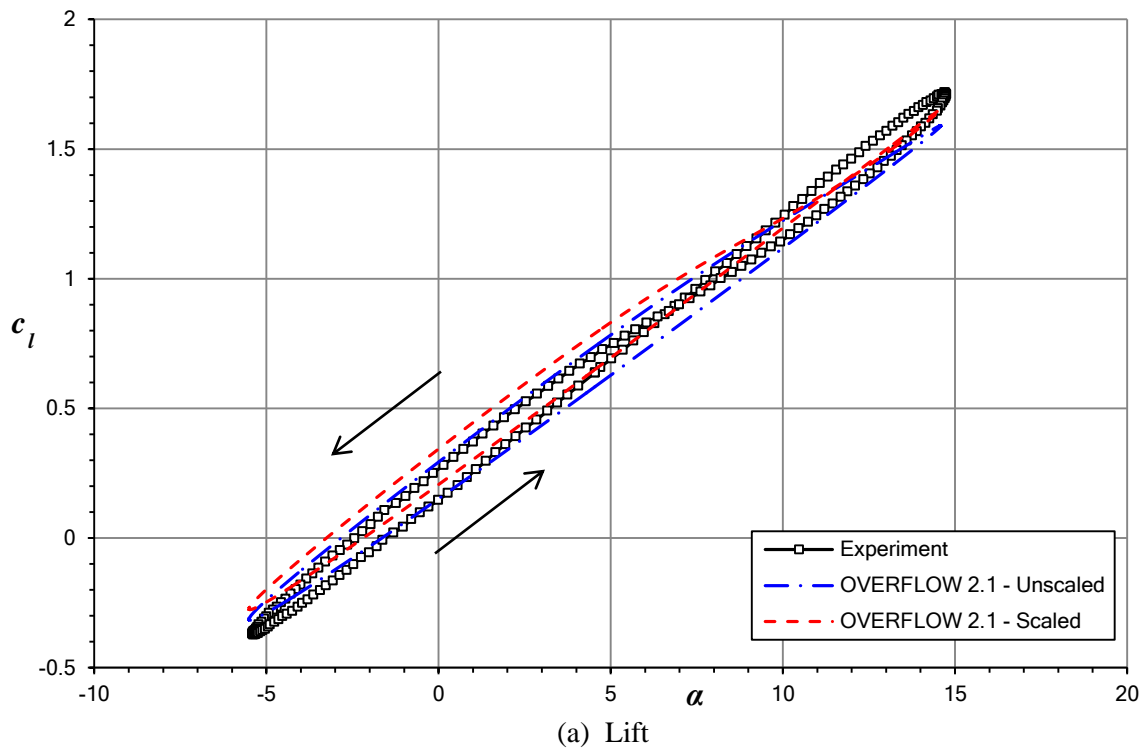


Figure 4-6. Dynamic stall predictions for the VR-7 compared with experiment [15] at $M_\infty = 0.184$, $R = 2.56 \times 10^6$, $\alpha = 4.55^\circ \pm 10.05^\circ$, and $k = 0.1$

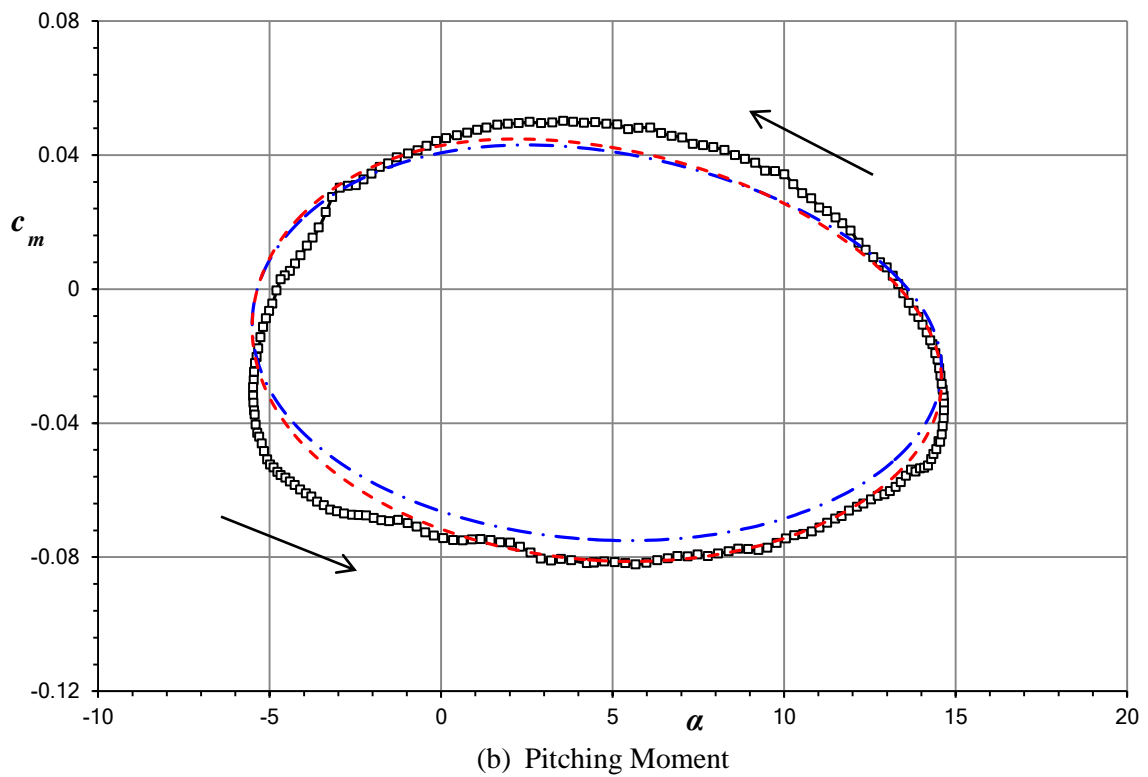
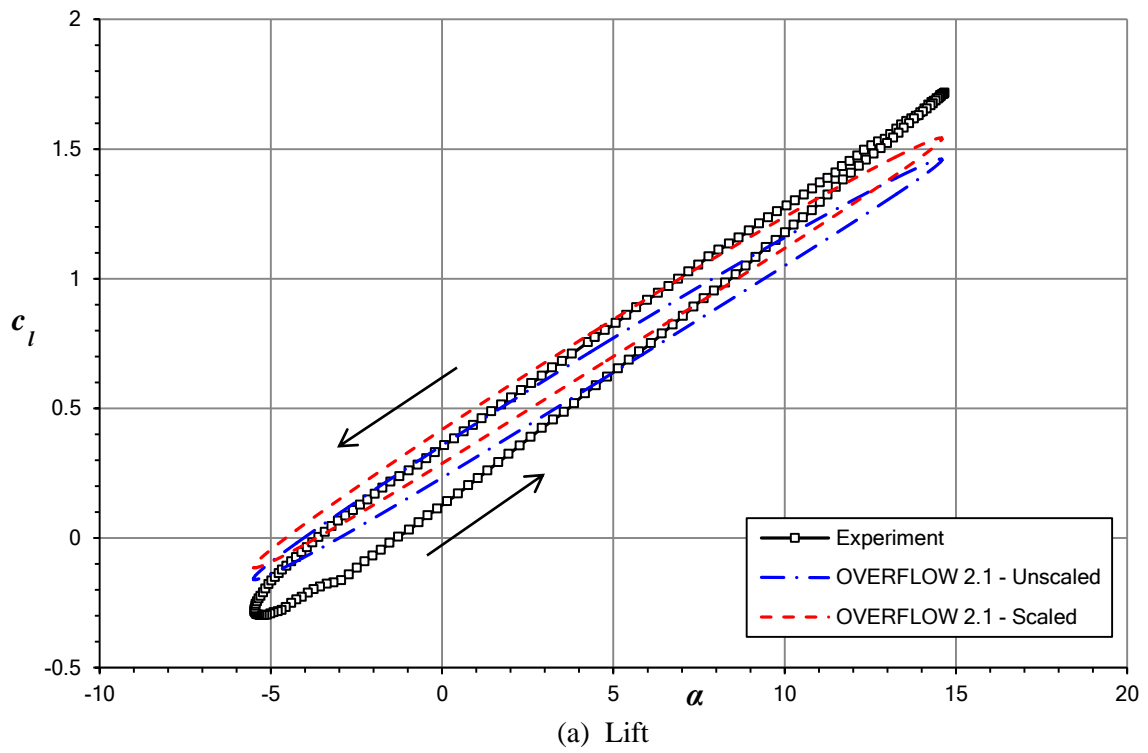


Figure 4-7. Dynamic stall predictions for the VR-7 compared with experiment [15] at $M_\infty = 0.184$, $R = 2.56 \times 10^6$, $\alpha = 4.55^\circ \pm 10.05^\circ$, and $k = 0.25$

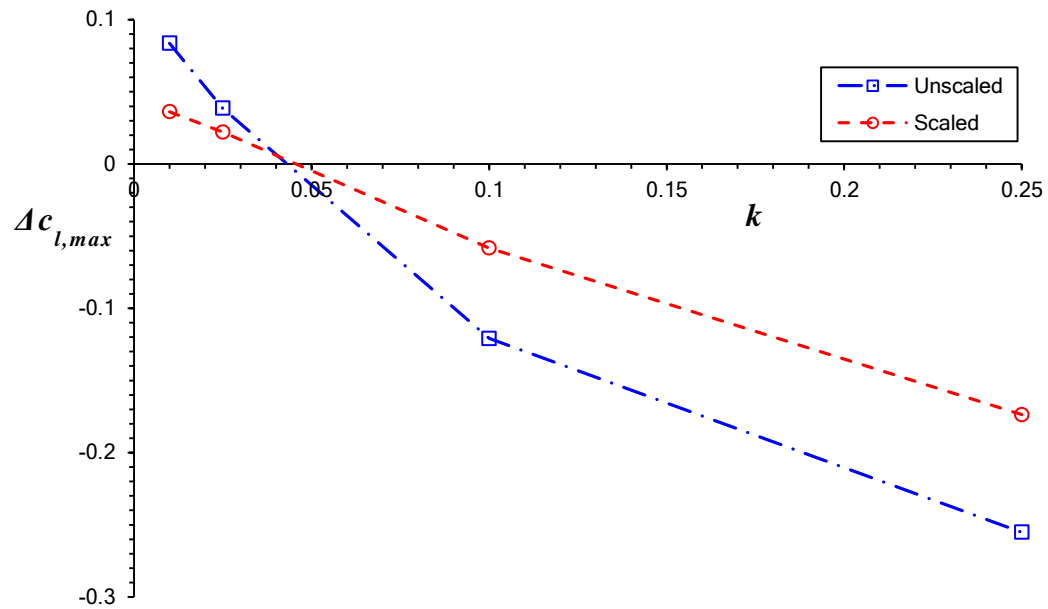


Figure 4-8. Error in predicted maximum lift coefficient as a function of reduced frequency for both scaled and unscaled simulations

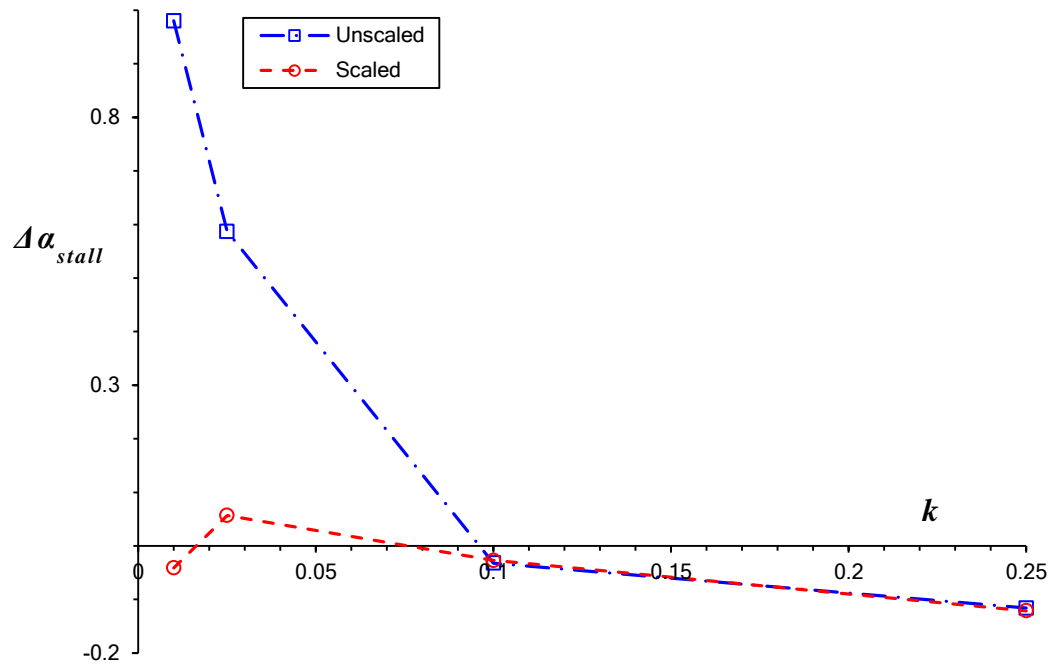


Figure 4-9. Error in predicted stall angle of attack as a function of reduced frequency for both scaled and unscaled simulations

4.5 Double Stall

The second set of dynamic stall cases analyzed in OVERFLOW were the double stall cases included in the USADSDP [15]. These VR-7 cases have a nominal angle of attack range of $\alpha = 15^\circ \pm 10^\circ$, which takes the airfoil significantly beyond stall. As with the stall suppression cases, both the scaled and unscaled approaches were used for the OVERFLOW solutions. These predictions are compared with experiment in Figs. 4-10, 4-11, and 4-12. For the most part, the use of scaled CFD predictions shows improvement compared to unscaled predictions.

For $k = 0.025$, shown in Fig. 4-10, the unscaled solution noticeably overpredicts the maximum lift coefficient, whereas the scaled solution slightly underpredicts it. The character of the lift predictions on the down-stroke is significantly different between the two OVERFLOW methods. Surprisingly, the experimental data follow a curve that is approximately the average of the two methods in this region. Both approaches show reasonably good agreement for the magnitude of the maximum negative pitching-moment coefficient, however neither accurately predicts the angle of attack at which it occurs. Based on the experimental data it can be observed that the maximum magnitude occurs on the down-stroke when the airfoil is exhibiting post-stall behavior. Thus the differences between experiment and CFD may be due to the three-dimensional post-stall behavior that would be observed in a wind tunnel but is not being modeled with OVERFLOW.

The predictions for $k = 0.10$, shown in Fig. 4-11, ostensibly shows a deviation from the trend of scaled solutions showing better agreement than unscaled solutions, but this is due to post-stall behavior having inherent errors in a two-dimensional CFD simulation. The unscaled solution better captures the magnitude of the secondary lift peak and the lift coefficient at the reattachment point, however this is when the flow is expected to be highly three-dimensional. The scaled solutions shows overall better agreement in lift and pitching moment through most of the

upstroke, even though the unscaled solution shows a more accurate prediction for the lift coefficient at the reattachment point. Both methods significantly overpredict the maximum magnitude of the pitching-moment coefficient, with the scaled solution showing superfluous peaks due to the post-stall vortices.

The results for $k = 0.20$ are shown in Fig. 4-12. Both the scaled and unscaled solutions underpredict the maximum lift coefficient, but the scaled approach better captures the character of the lift overshoot. In fact, the scaled solution shows very good agreement with experiment for both lift and pitching-moment coefficient. The only exception is that the scaled CFD appears to predict an additional vortex during the down-stroke, as evidenced by the extra peaks in the lift and pitching-moment coefficients not present in the experimental data. The unscaled CFD appears to over-resolve multiple vortices, however the predictions do not show nearly as good agreement.

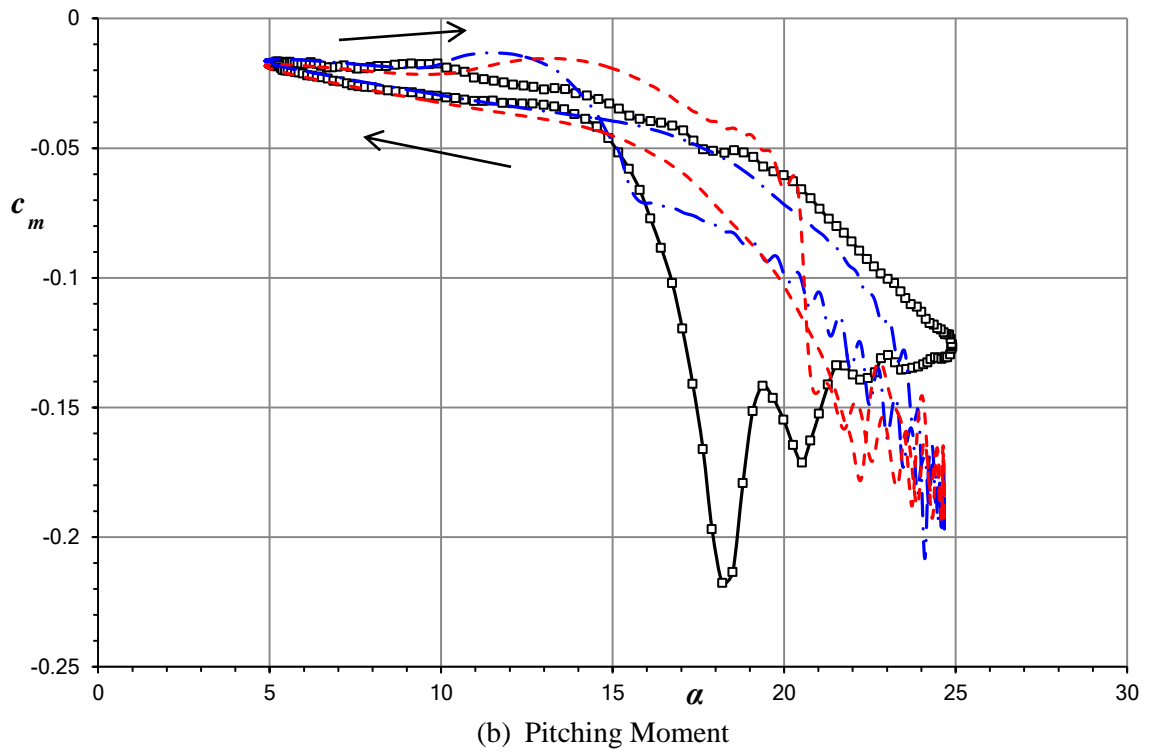
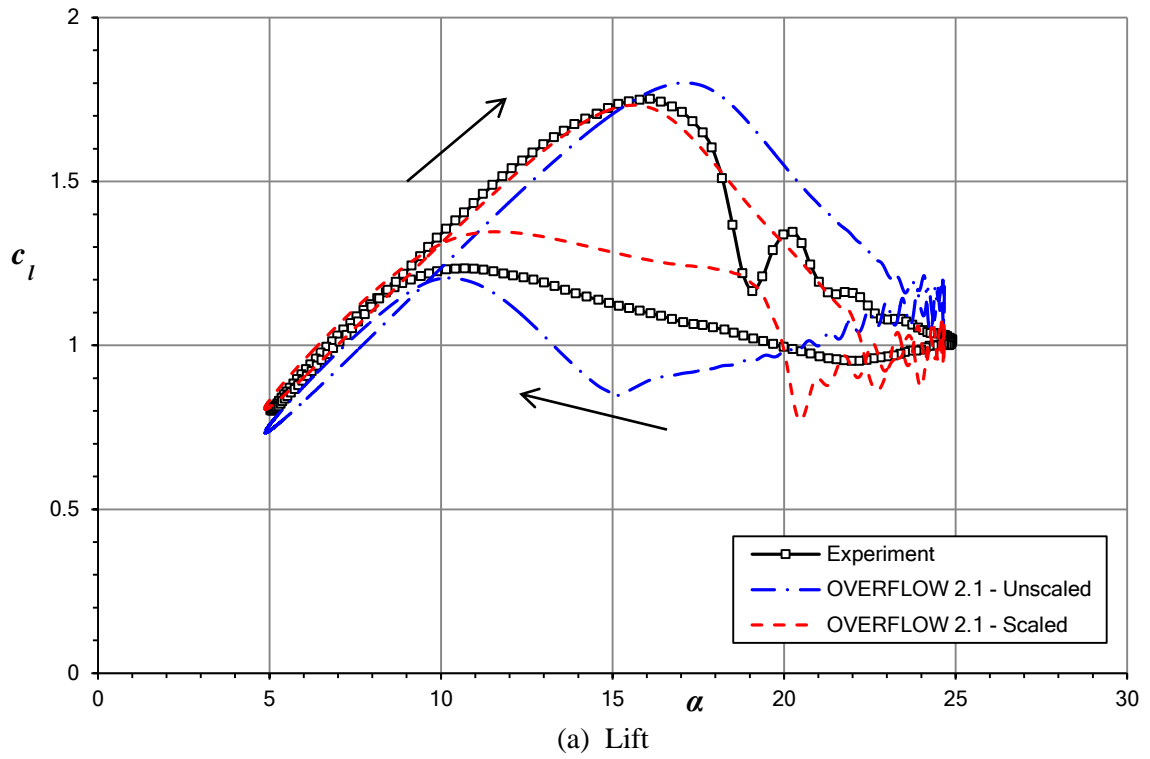


Figure 4-10. Dynamic stall predictions for the VR-7 compared with experiment [15] at $M_\infty = 0.184$, $R = 2.53 \times 10^6$, $\alpha = 14.77^\circ \pm 9.90^\circ$, and $k = 0.025$

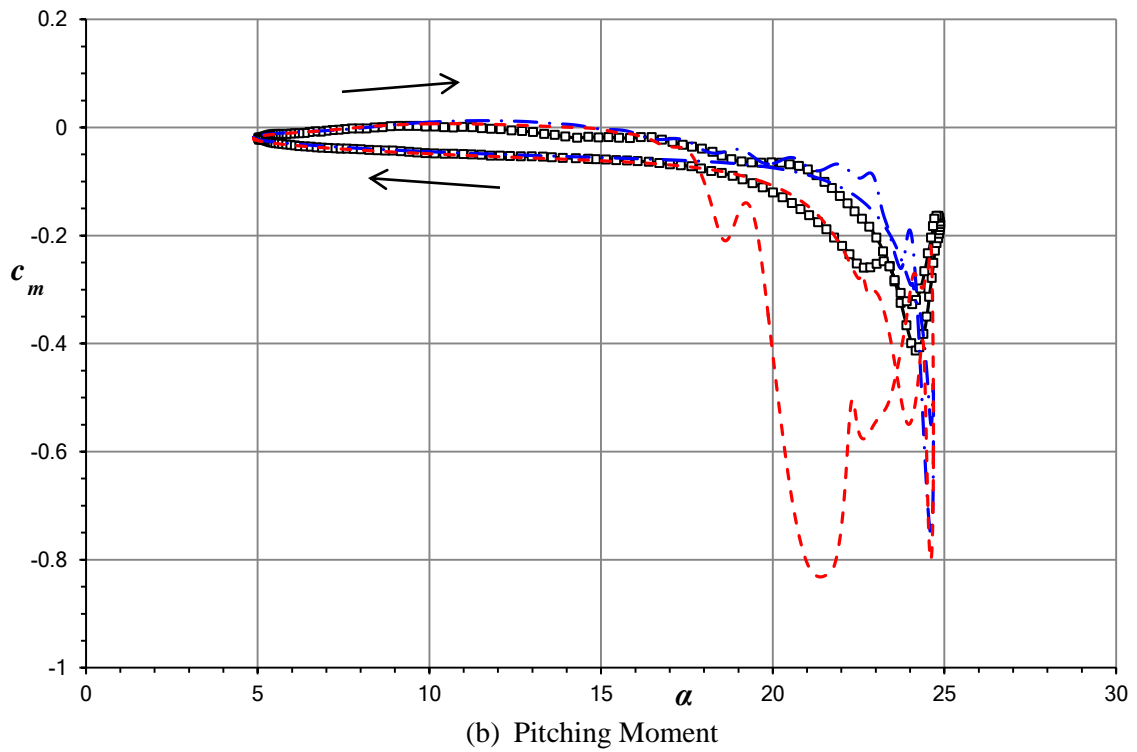
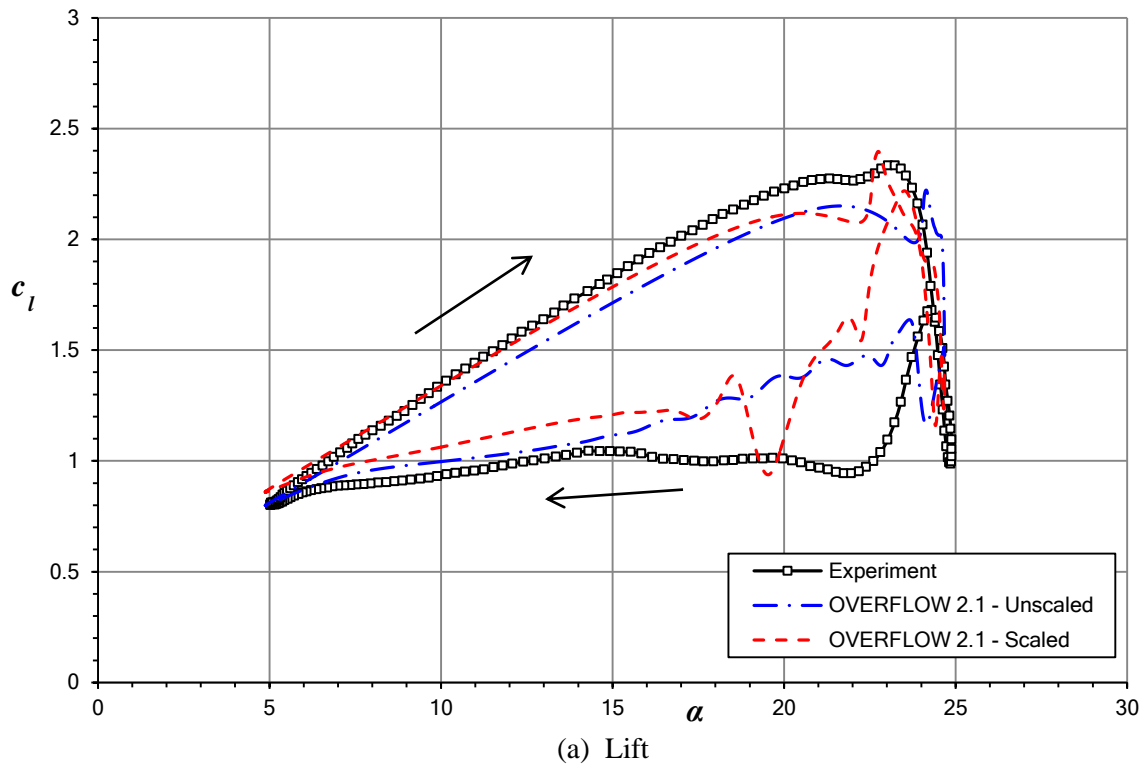


Figure 4-11. Dynamic stall predictions for the VR-7 compared with experiment [15] at $M_\infty = 0.185$, $R = 2.60 \times 10^6$, $\alpha = 14.78^\circ \pm 9.90^\circ$, and $k = 0.10$

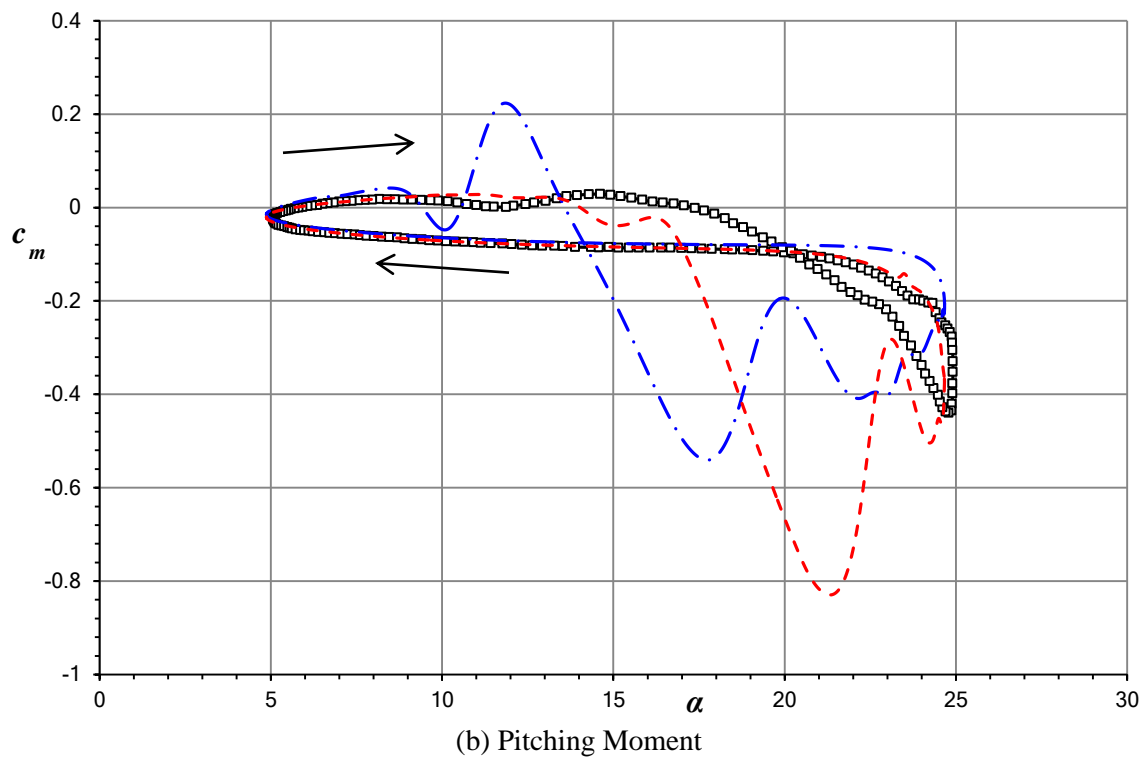
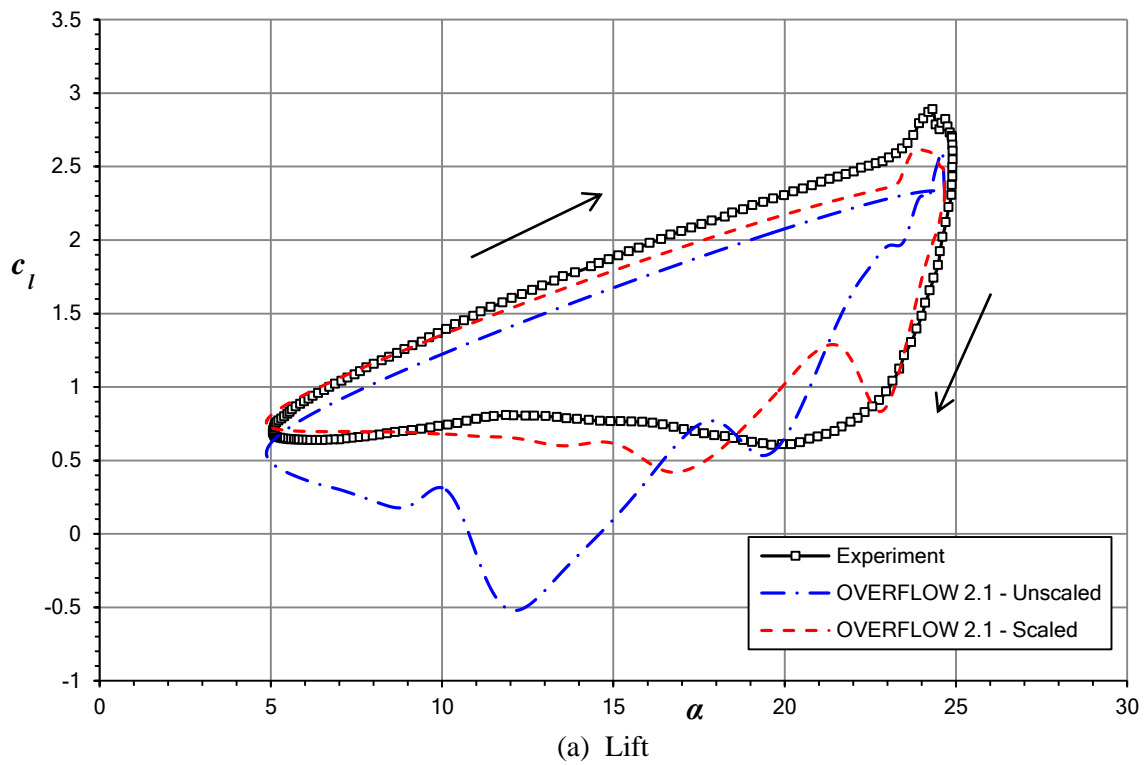


Figure 4-12. Dynamic stall predictions for the VR-7 compared with experiment [15] at $M_\infty = 0.185$, $R = 2.58 \times 10^6$, $\alpha = 14.77^\circ \pm 9.90^\circ$, and $k = 0.20$

Chapter 5

Upstream Miniature Trailing-Edge Effector Predictions

The VR-7 airfoil geometry was also analyzed using CFD with the aim of understanding the flow physics of an upstream miniature trailing-edge effector (MiTE), which is a deployable Gurney flap located upstream of the trailing-edge of the airfoil. The distance upstream is dependent on the airfoil geometry and the desired flap size, as there generally needs to be sufficient rotor-blade thickness to store the MiTE. The ultimate goal of this research is to further develop an unsteady MiTE aerodynamic model based on the Duhamel integral [5,7]; therefore, OVERFLOW has been used to supply the aerodynamic responses required to develop the form of the model. The details of this model are presented in [29].

5.1 Upstream MiTE Grids

Two different approaches were considered for modeling the geometry of an upstream MiTE. The first method, used by Kinzel et al. [5-8] and Chow and van Dam [21-23], models the MiTE as having finite thickness and moving as a solid body in the flow field. This has the advantage of being more physically realistic, but is unable to model a truly indicial MiTE deployment. The second approach, used extensively by Min et al. [26], takes advantage of being able to modify the off-body boundary conditions in the flow field and applies a wall condition to a line of grid points normal to the airfoil/wing surface. This, in effect, treats the MiTE as being infinitely thin. While this can more closely represent an indicial MiTE deployment, it is limited in its ability to represent a finite deployment speed.

The grids for the finite-thickness MiTE geometry are shown in Figs. 5-1, 5-2, and 5-3. The key feature in this overset approach is the collar grids, which facilitate the deployment of the MiTE without introducing orphan points into the solution. Two small ($0.0005c$) gaps are introduced on the airfoil surface on either side of the MiTE, into which the collar grids make a 90° convex bend. By properly defining the collar surface grid and taking advantage of hyperbolic field grid generation, the collar field grid aligns exactly with the flap. A no-slip condition is applied at the base of the gap and on a select range of collar field grid points that are coincident with the MiTE surface. This results in a continuous application of the no-slip boundary condition along the surfaces of the airfoil and the MiTE, even after XRAY hole cutting occurs.

The infinitely-thin MiTE approach uses the same airfoil O-grid and box-grid as the finite-thickness approach, except that the MiTE surface and the collar grids have been removed. The line of grid points for the off-body no-slip boundary condition extends from the airfoil surface grid point closest to the MiTE centerline to the desired height into the flow field. Because the VR-7 airfoil has low curvature near the trailing edge of the lower surface, this set of grid points maintains a nearly straight path normal to the airfoil.

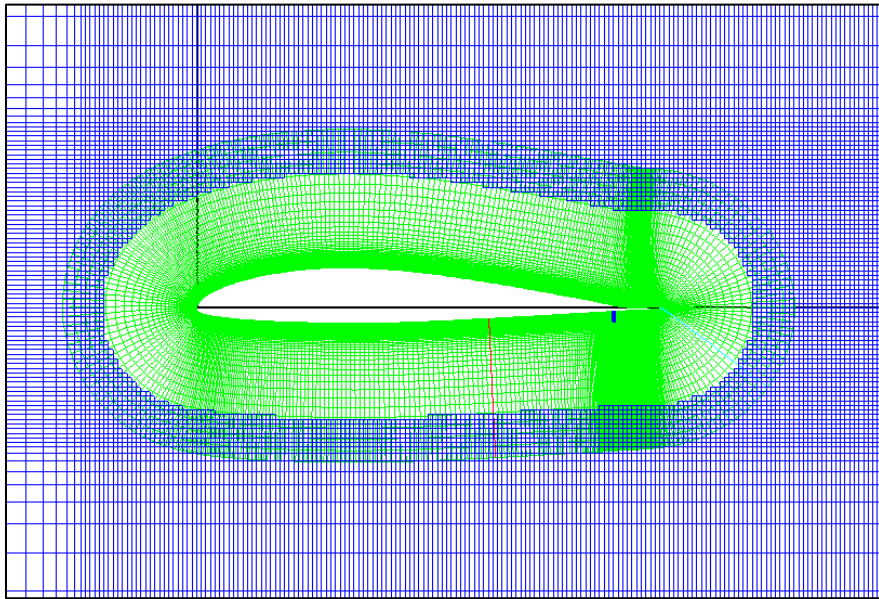


Figure 5-1. Near-field grid with a hole cut in far-field grid for the VR-7 with a $0.02c$ MiTE at $0.90c$

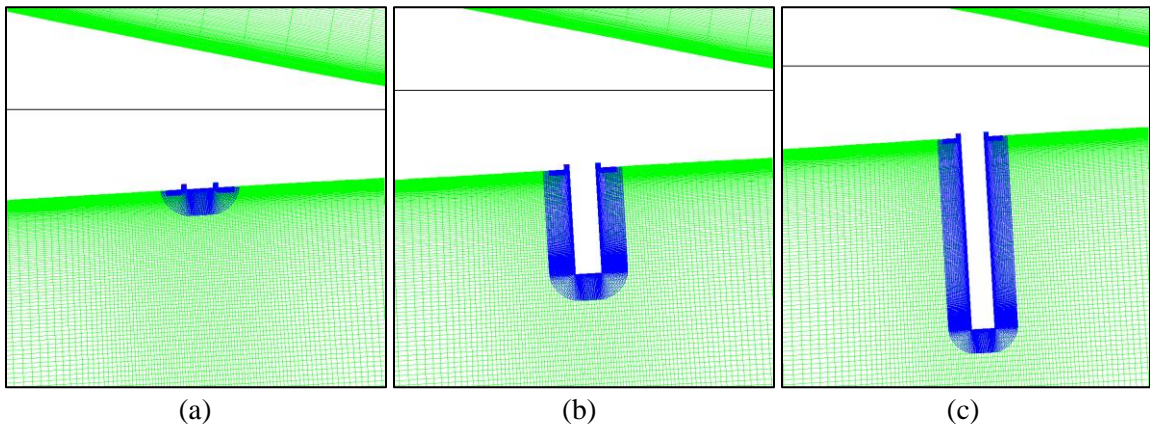


Figure 5-2. Body-fitted grid for a $0.02c$ MiTE retracted (a), partially extended (b), and fully deployed (c)

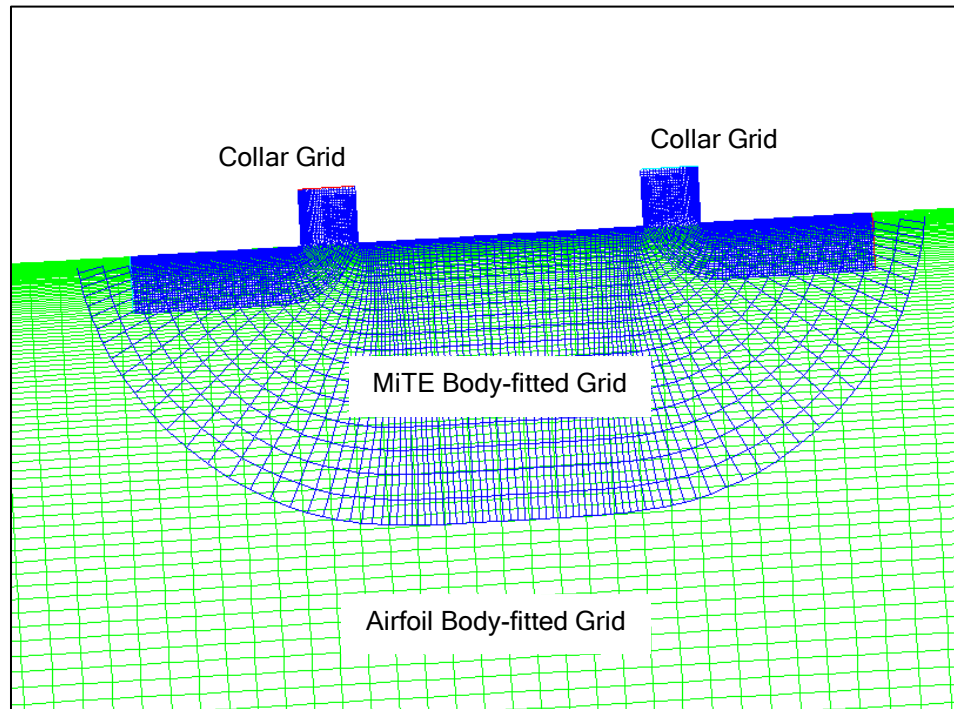


Figure 5-3. Close up of body-fitted grids and collar grids with the MiTE retracted

5.2 Baseline Operating Conditions

The baseline operating conditions for this study were chosen to be a Mach number of 0.3 and a Reynolds number of 4×10^6 , which reasonably represent the retreating blade of a rotor in forward flight.

The Mach number is high enough that the flow-solver does not have numerical problems and low enough that compressibility effects do not immediately influence the solution. Higher Mach numbers, such as $M_\infty = 0.5$, have also been considered to provide validation cases for compressibility corrections present in the indicial models.

The Reynolds number is assumed to be high enough that the flow over a rotorcraft airfoil would be mostly turbulent and that the quality of the fully-turbulent solution would minimally be affected by neglecting for laminar separation bubbles.

5.3 Indicial and Ramp Deployments

5.3.1 Verification of CFD Indicial Response

A true indicial deployment can be modeled using the infinitely thin MiTE approach described above, but it is not initially clear that this would give an accurate development of forces. One would expect that the circulatory terms of the unsteady forces and moments would be captured, but not having a physical MiTE with a moving wall may give some erroneous results. To test this, a ramp MiTE deployment scheme introduced by Chow and van Dam [23] was used which approximates the Heaviside function using a half-period of a sine wave connecting different constant values; this can be seen graphically in Fig. 5-4. The “steepness”, or deployment time, of the half-sine ramp can be controlled using a local reduced frequency, k_{HS} , as follows:

$$T_{deploy}^* = \frac{\pi}{2k_{HS}} \quad 5-1$$

The lift and pitching-moment coefficients for a case using $k_{HS} = 10$ with a $0.02c$ -high MiTE are presented along with the indicial deployment in Fig. 5-5. Both methods converge to the same normalized result within two non-dimensional time units after deployment begins. The normalized data presented in this and subsequent plots are defined as:

$$c_{(l,d,m),norm} = \frac{\Delta c_{(l,d,m)}}{\Delta c_{(l,d,m),GF}} \quad 5-2$$

The unsteady oscillations seen in Fig. 5-5 are of different phase and magnitude; however, they share the same mean response. With the similarities of the two responses, it can be inferred that the infinitely-thin MiTE indicial deployment is representative of a finite-thickness MiTE deploying in the limit of $k_{HS} \rightarrow \infty$. There is an upper-limit on the deployment rate of a MiTE in a numerical solution, as the MiTE may exceed a Mach number of unity and introduce shockwaves

into the solution. Given that the grids were generated assuming fully subsonic flow, a shockwave would not be adequately resolved and would corrupt the solution.

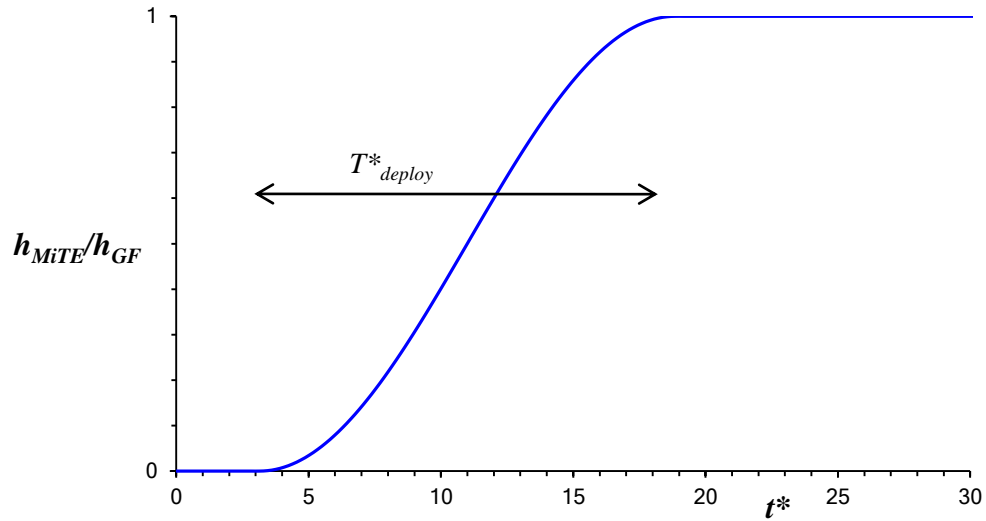
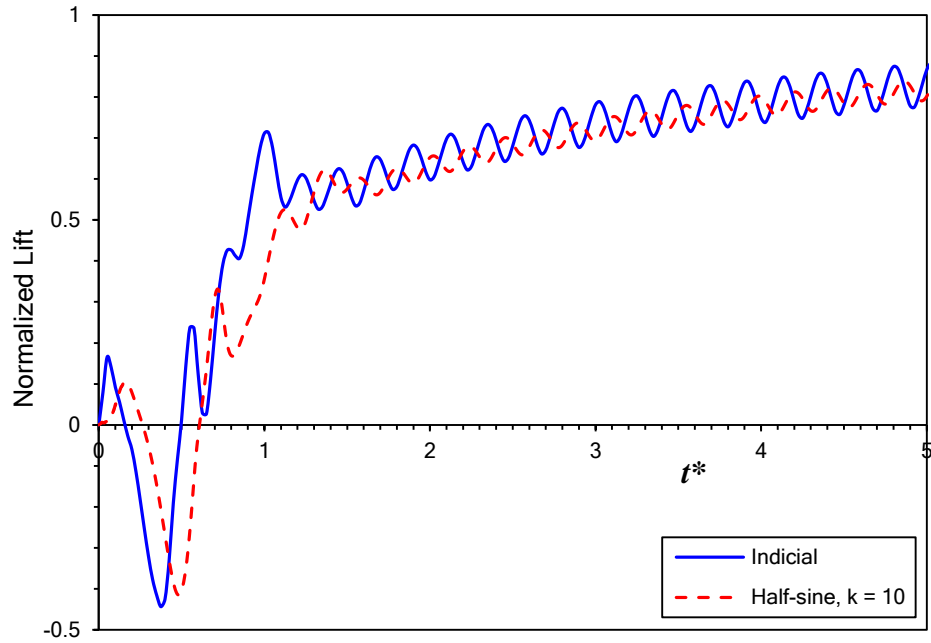
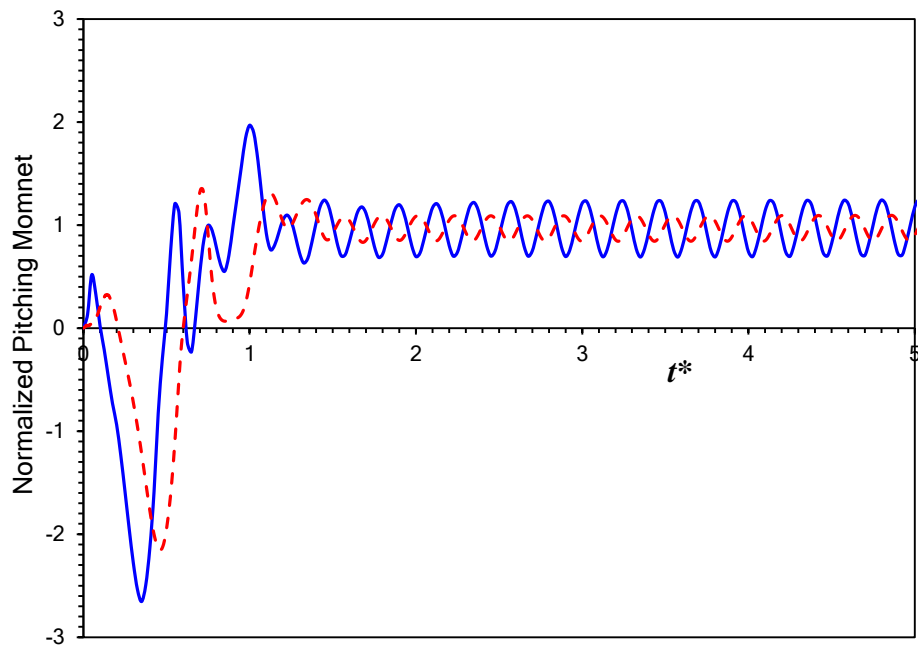


Figure 5-4. Half-sine ramp deployment scheme for $k_{HS} = 0.1$



(a) Lift



(b) Pitching Moment

Figure 5-5. Comparison of the aerodynamic response of an indicially-deployed, infinitely thin MiTE with the response of a finite-thickness MiTE deployed at $k_{HS} = 10$, both $0.02c$ high located at $0.90c$ with $\alpha = 5^\circ$, $M_\infty = 0.3$, $R = 4 \times 10^6$

5.3.2 Vortex due to Upstream MiTE

A peculiar aspect of the responses, common to both methods, is that there is an early sharp decrease in lift coefficient and the magnitude of the pitching-moment coefficient. This represents a significant departure from the flow physics and force development seen for trailing-edge MiTE deployments. An example of typical trailing-edge behavior is shown in Fig. 5-6 for a VR-12 airfoil with a $0.02c$ MiTE having the same half-sine deployment rate as used previously.

The influence of the airfoil lift coefficient was investigated by varying the angle of attack relative to the free stream. The data presented in Fig. 5-7 show that the qualitative flow features are the same at different angles of attack, albeit with varying relative magnitudes. The characteristic peaks and valleys in the lift response have lower values as the angle of attack increases. The magnitude of the initial oscillations of the drag coefficient response become larger with increasing angle of attack, and the average value of the normalized coefficient remains higher as it tends toward the steady-state response. The normalized pitching-moment coefficient shows that the initial decrease (which is actually a more nose-up moment) is approximately the same for all angles of attack, but the secondary peak is lower for the higher angles of attack. From these data it is unclear whether the changes in the aerodynamic response are due to changes in the baseline lift coefficient or changes in the local pressure distribution near the retracted MiTE.

To further investigate the influence of the local pressure distribution, the VR-12 and S408 airfoils were also analyzed in OVERFLOW with a $0.02c$ MiTE located upstream at $0.90c$. These data are compared with those from the VR-7 in Fig. 5-8; the baseline lift coefficient is 0.7 for all cases shown. Based on the force and moment predictions, it can be concluded that the qualitative flow features are independent of the airfoil, however, the magnitudes of the important *peaks* in the aerodynamic response are not. Instead, they are most likely a function of the local pressure distribution near the retracted MiTE. This is corroborated by the retracted-MiTE pressure

distributions shown in Fig. 5-9, with all airfoils operating at a lift coefficient of 0.7; there is a noticeable trend that with more positive pressure coefficients in the MiTE region, the *peaks* in the lift, drag, and pitching-moment responses have a higher magnitude. Since the pressure coefficient on the lower surface of the airfoil tends to become more positive as the lift coefficient increases [53], the trends shown in Figs. 5-7 and 5-8 are consistent with each other.

Further insight into the flow physics can be gained by visualizing the time-accurate solution using a post-processor, which for this study was FIELDVIEW 12 [54]. Figure 5-10 shows a sequence of pressure contours from the $k_{HS} = 10$ MiTE deployment as shown in Fig. 5-7, with blue being low pressure and red being high. It can be seen that immediately after the MiTE is deployed it acts like a pressure dam between regions of very high and very low pressure. At this time in the force development, frames (a) and (b), the high pressure region dominates such that the lift is increased and the pitching moment becomes more nose-down. In frames (c) through (g), the high-pressure region upstream of the MiTE diffuses, but the low-pressure region maintains its strength and convects downstream. It is during this time that the lift decreases and the pitching moment is more nose-up. Once the low-pressure region reaches the trailing edge, frames (g) and (h), it detaches from the airfoil and splits into two smaller regions. The immediate departure of this low pressure from the surface causes a rapid, but temporary, increase in the magnitudes of lift and pitching moment. Then, the airfoil exhibits the Wagner/Küssner-type [1] development of the circulation. As is observed in frames (i) and (j), the vortex that had been observed on the lower surface behind an upstream Gurney flap is not the original low-pressure region, but instead is created after that low-pressure has convected downstream of the trailing edge.

It was originally hypothesized that the low-pressure region behaves as a vortex with negative circulation. While streaklines and instantaneous streamlines can be used to see vortical behavior in the flow-field, it remains difficult to track individual vortex cores. Instead, entropy

was used to visualize the solid core behavior of physical vortices, as entropy increases in and around it. Figure 5-11 shows entropy contours for select frames following the same MiTE deployment as shown in Fig. 5-10. Figure 5-11(a) confirms the hypothesis that the low-pressure is indeed a vortex which forms immediately behind the MiTE and is bound to the tip of the flap. Even though the vortex core convects downstream, it appears to remain bound by a vortex sheet to the MiTE, as seen in Fig. 5-11(b), and deforms in a manner that is visually similar to a Kelvin-Helmholtz instability [55]. The next frame, Fig. 5-11(c), shows a peculiar occurrence in that a strong, positive-circulation vortex is pulled down from the upper surface. Based on the pressure contours of Fig. 5-10(f) and 5-10(g), it appears that this is due to the region of low pressure reaching the trailing edge, and so higher pressure fluid on the upper surface gets pulled to the lower surface. The last frame of Fig. 5-11 confirms that after the initial vortices have passed the trailing edge, the airfoil sheds a Karman vortex street.

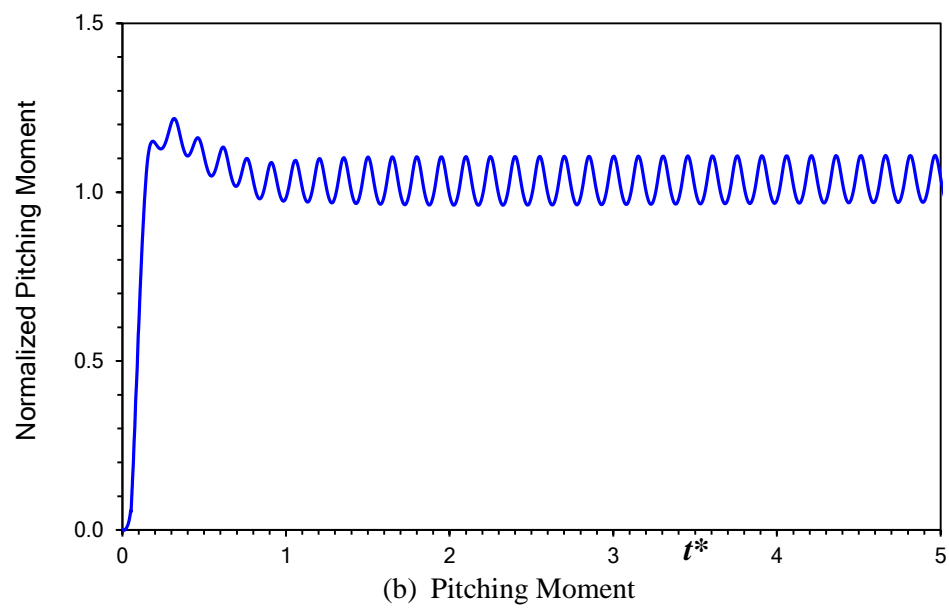
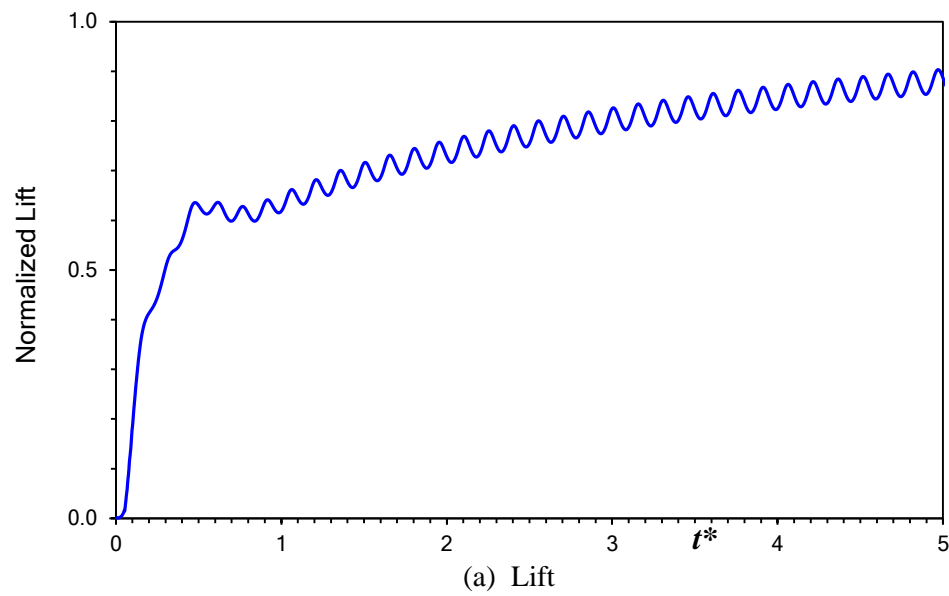


Figure 5-6. Half-sine ramp deployment of a $0.02c$ MiTE at $1.00c$ on the VR-12 airfoil, $k_{HS} = 10$, with $\alpha = 5^\circ$, $M_\infty = 0.3$, $R = 4 \times 10^6$

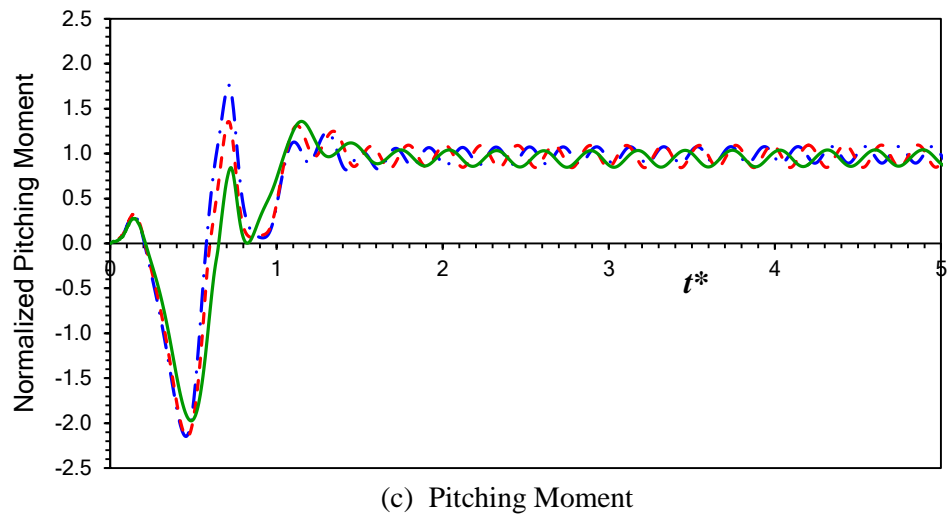
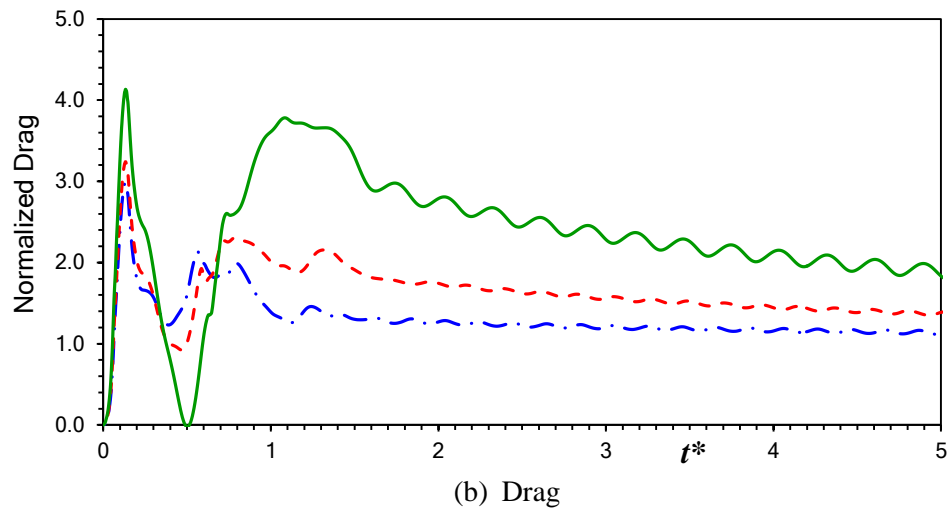
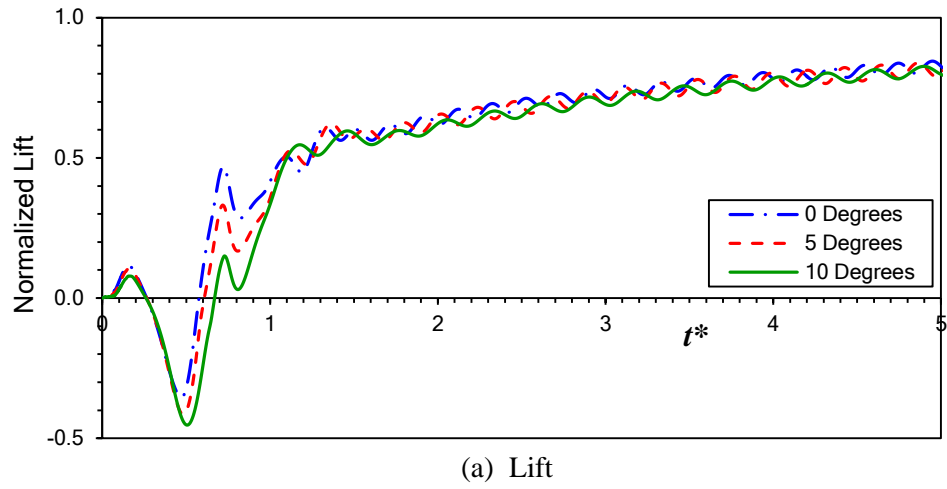
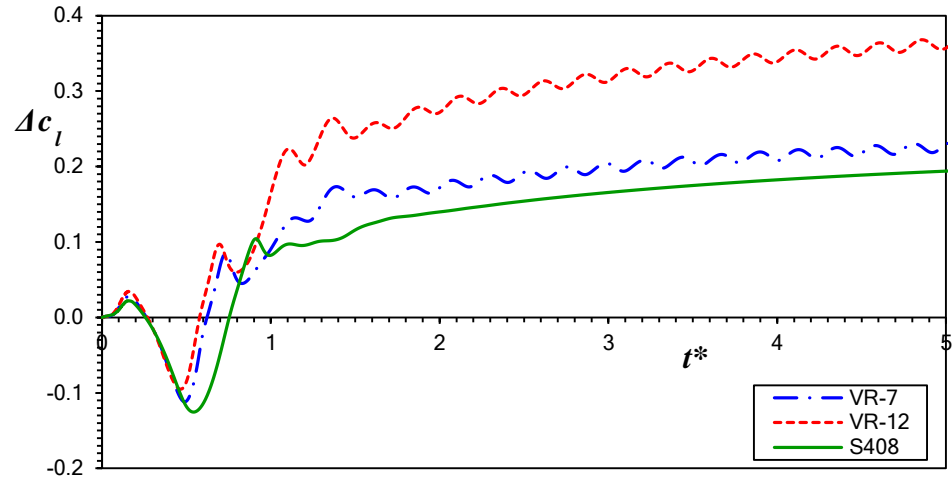
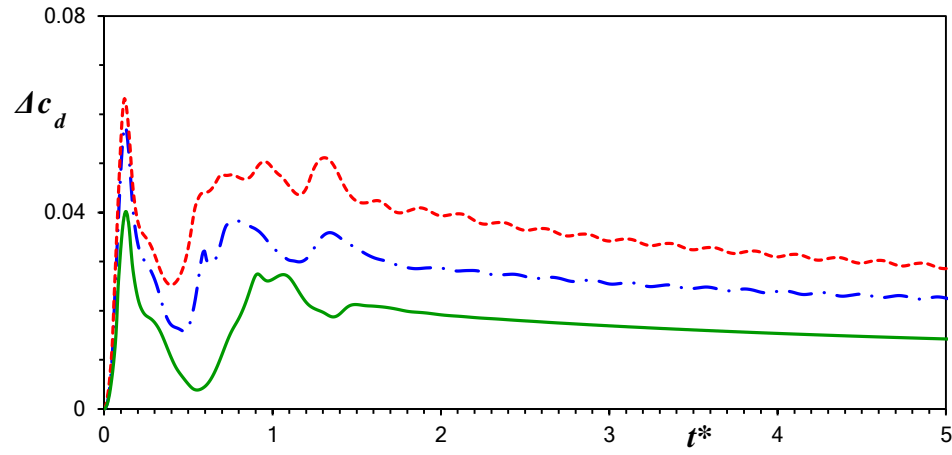


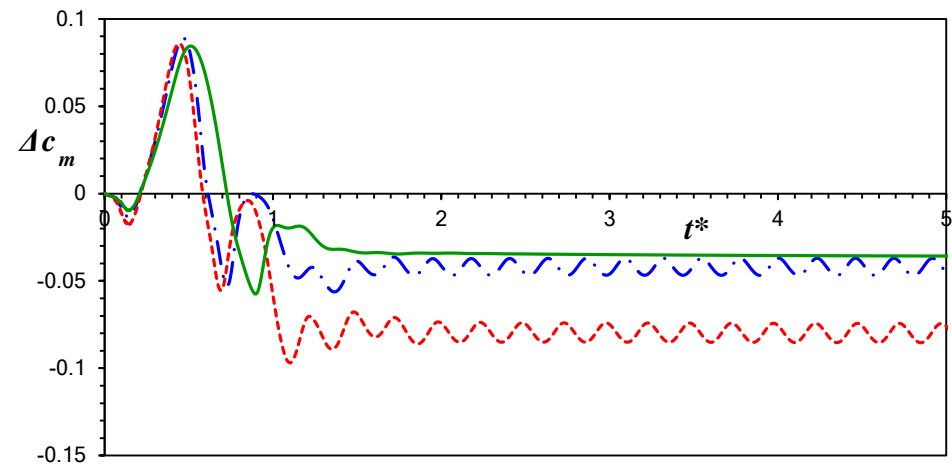
Figure 5-7. Aerodynamic predictions for a $k_{HS} = 10$ ramp deployment of a $0.02c$ MiTE at $0.90c$ on the VR-7 airfoil, $M_\infty = 0.3$, $R = 4 \times 10^6$, and $\alpha = 0^\circ$, 5° , and 10°



(a) Lift



(b) Drag



(c) Pitching Moment

Figure 5-8. Half-sine ramp deployment of a $0.02c$ MiTE upstream at $0.90c$ for various airfoils, $k_{HS} = 10$, with $\alpha = 5^\circ$, $M_\infty = 0.3$, $R = 4 \times 10^6$

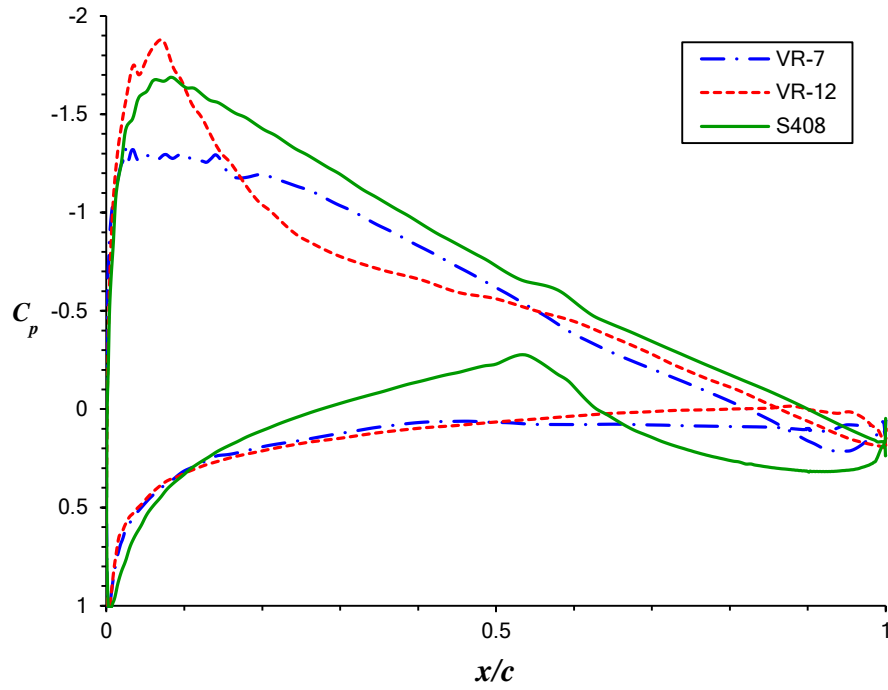


Figure 5-9. Pressure distributions for the VR-7, VR-12, and S408 airfoils at $c_l = 0.7$, $M_\infty = 0.3$, and $R = 4 \times 10^6$

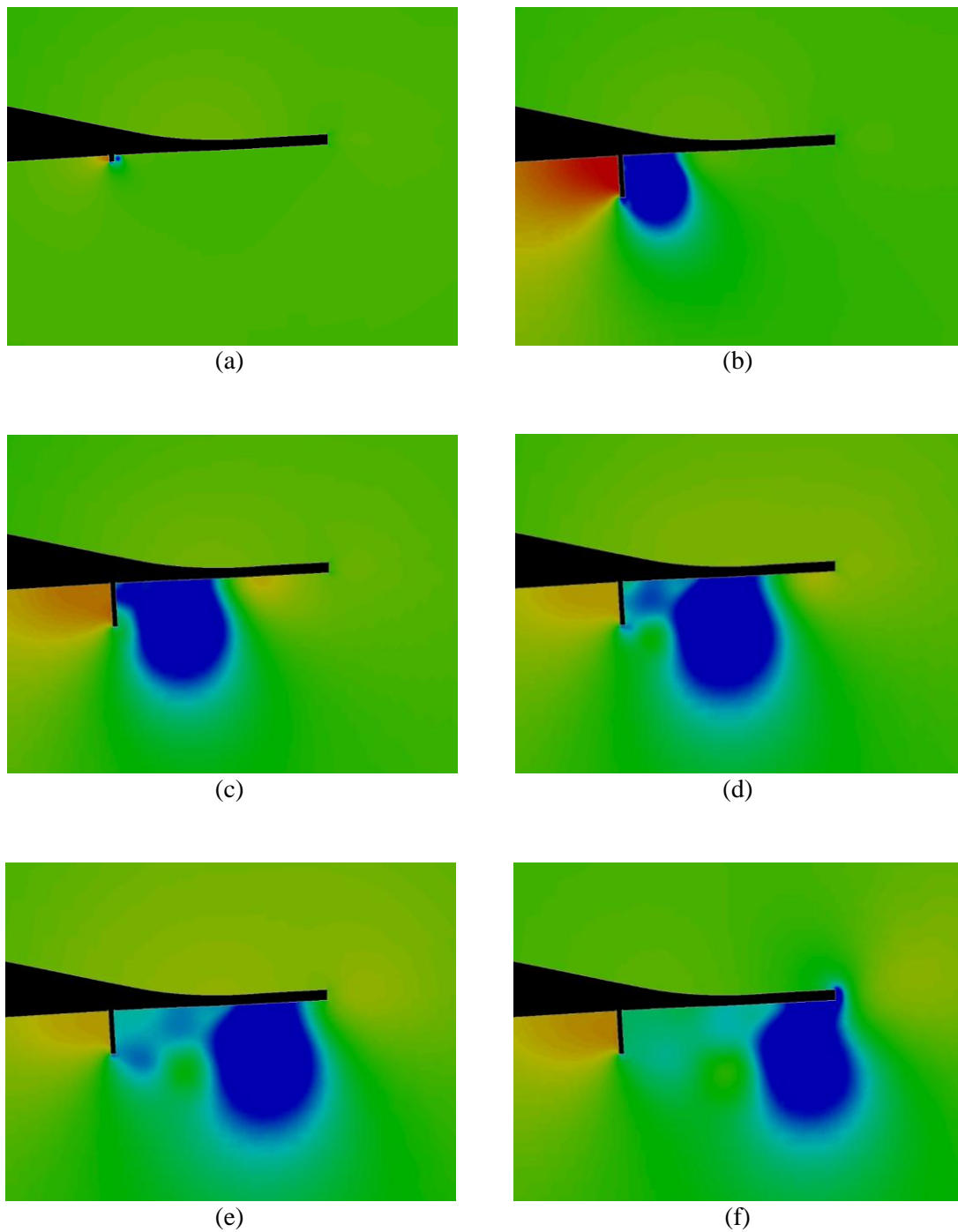
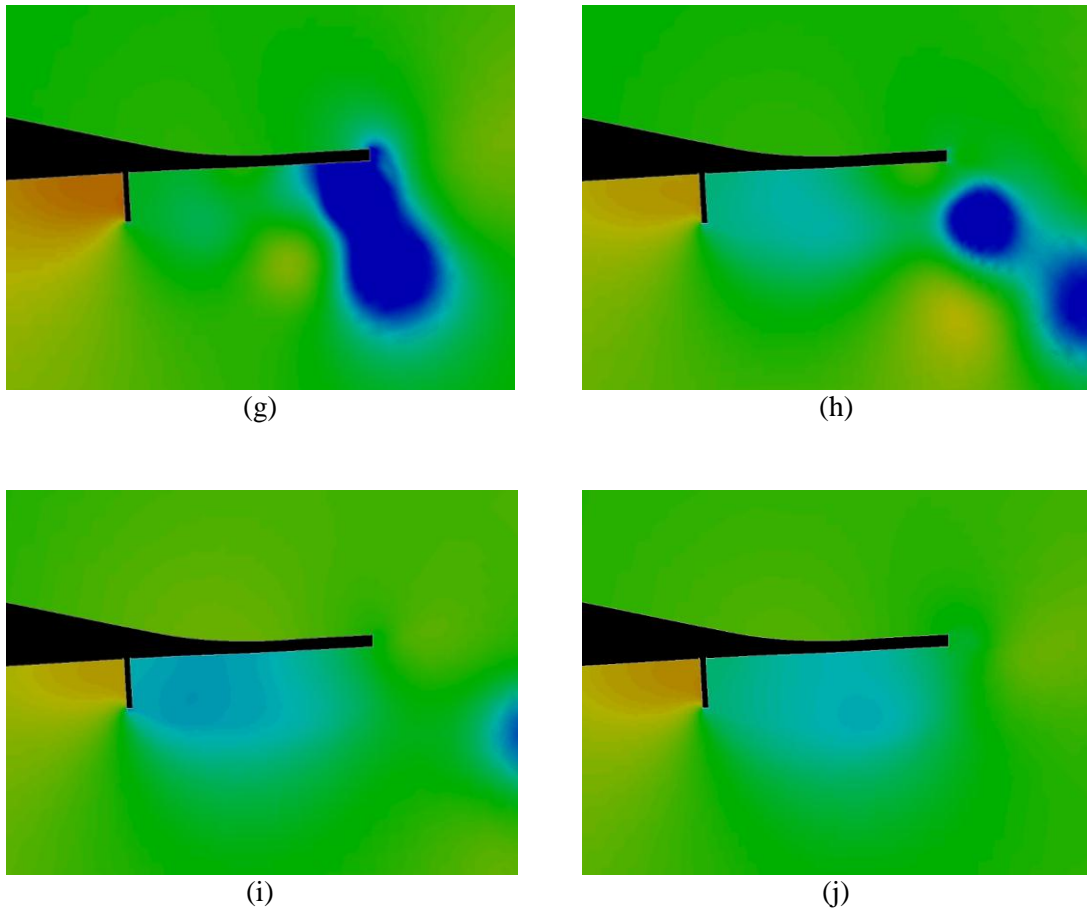
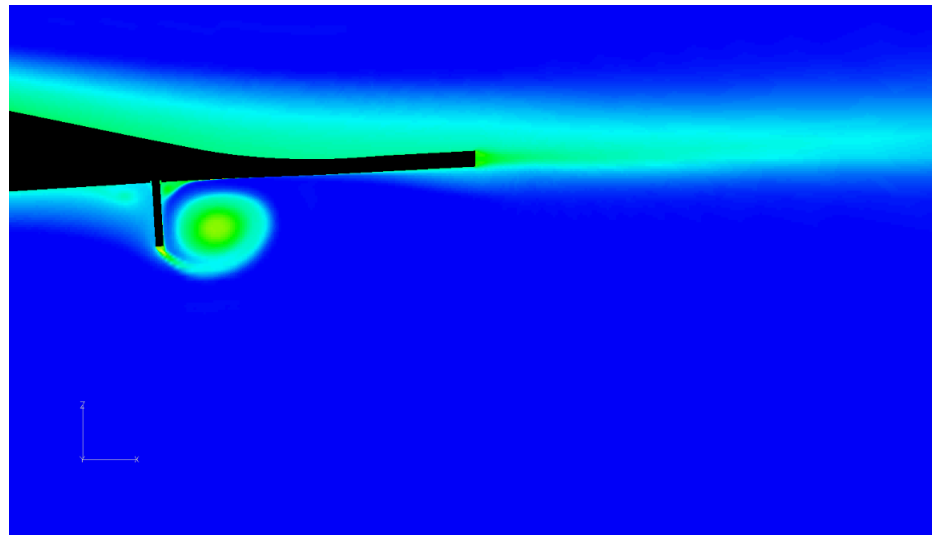
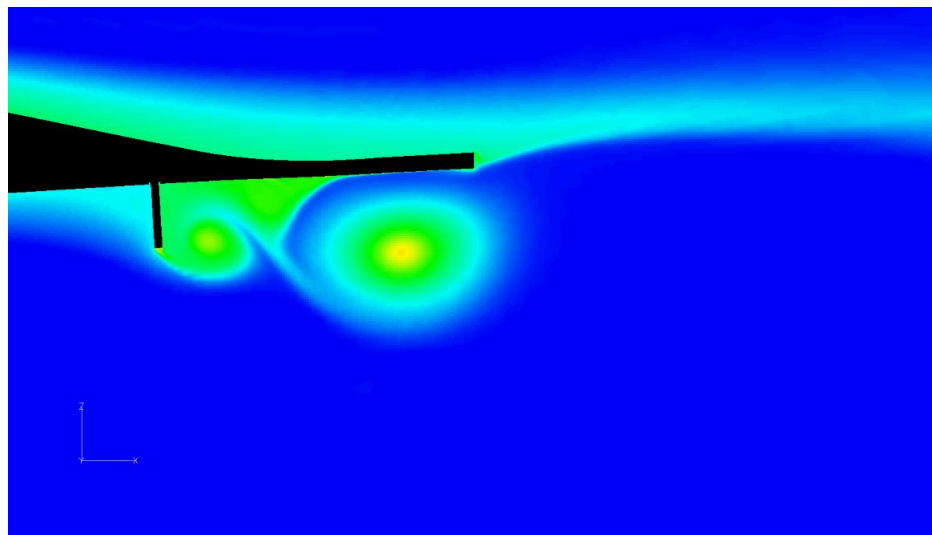


Figure 5-10. Pressure contours (red = high, blue = low) of select frames following a $k_{HS} = 10$ half-sine deployment of a $0.02c$ MiTE at $0.90c$ on the VR-7 airfoil, $\alpha = 5^\circ$, $M_\infty = 0.3$, $R = 4 \times 10^6$



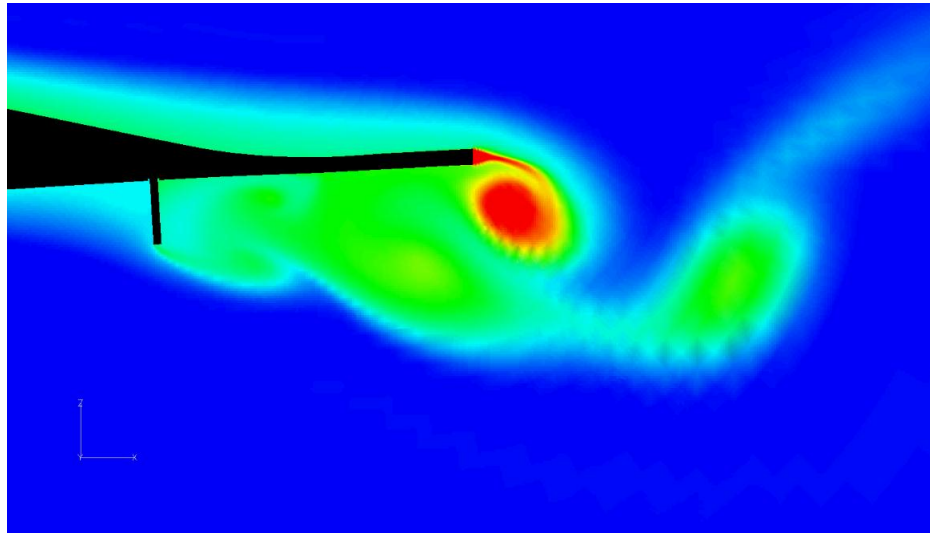


(a)

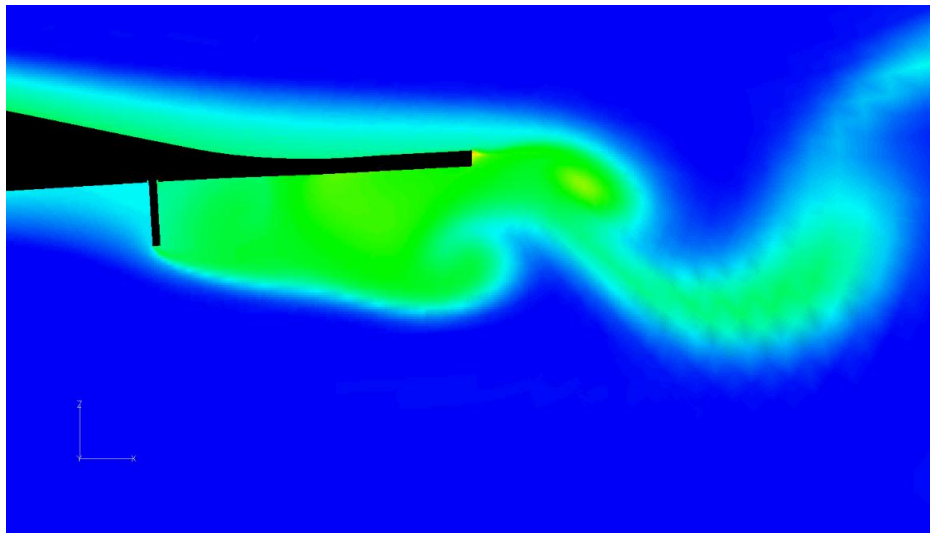


(b)

Figure 5-11. Entropy contours (red = high, blue = low) of select frames following a $k_{HS} = 10$ half-sine deployment of a $0.02c$ MiTE at $0.90c$ on the VR-7 airfoil, $\alpha = 5^\circ$, $M_\infty = 0.3$, $R = 4 \times 10^6$



(c)



(d)

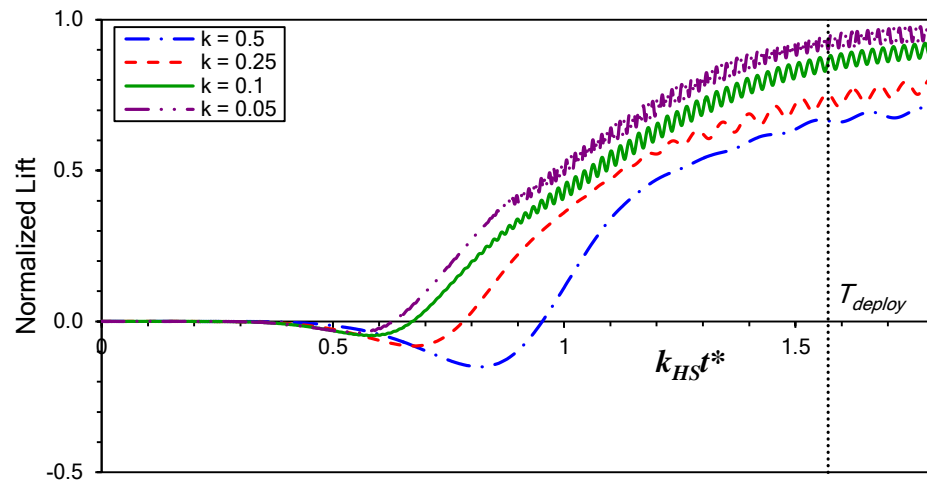
Figure 5-11 (concluded). Entropy contours (red = high, blue = low) of select frames following a $k_{HS} = 10$ half-sine deployment of a $0.02c$ MiTE at $0.90c$ on the VR-7 airfoil, $\alpha = 5^\circ$, $M_\infty = 0.3$, $R = 4 \times 10^6$

5.3.3 Slower Ramp Deployments

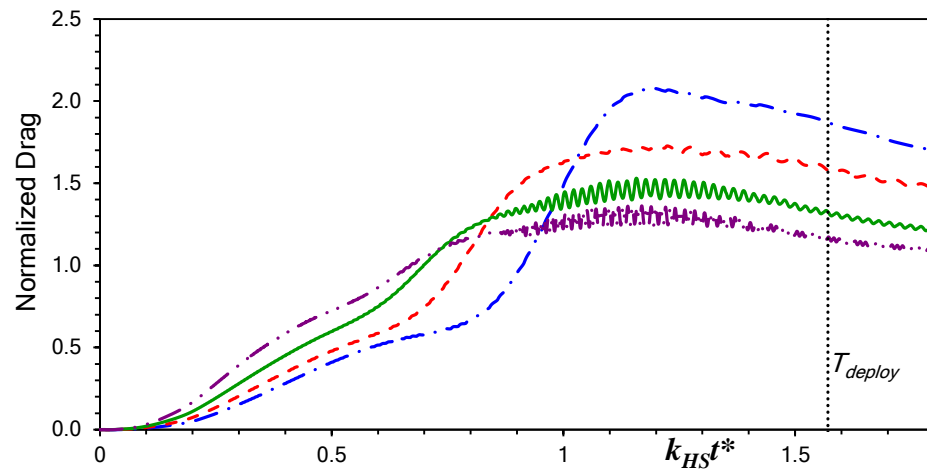
Using the Duhamel integral as the basis of an unsteady MiTE model assumes that the governing equations obey the superposition principle. Accuracy is lost, however, when the governing equation is non-linear and the superposition principle is no longer valid [56]. While the well-known Wagner function was derived for indicial airfoil responses and can be integrated using the Duhamel integral, it is a solution to Laplace's equation. Laplace's equation governs potential flow, which is a linearization of the incompressible Navier-Stokes equations that assumes attached flow and negligible viscosity [57]. An indicially deployed MiTE, on the other hand, is characterized by large amounts of separated flow and flow instabilities, which introduces non-linearities to the unsteady response. As such, it may be beneficial to linearize an unsteady model about a non-indicial response that is representative of rotorcraft deployment. In other words, the model would not be based purely on the indicial response, but instead would be calibrated so that a select finite deployment rate would have the most accuracy [29].

The aerodynamic responses for several deployment rates are plotted in Fig. 5-12; the non-dimensional time of the response is scaled by the reduced frequency of the half-sine deployment, as the product $k_{HS}T^*_{deploy}$ is a constant. The different curves can thus be thought of as having the same physical deployment time, but with varying freestream velocity. This is reflected in the lift coefficient responses shown in Fig. 5-12(a); the $k_{HS} = 0.5$ response corresponds to the slowest incoming velocity, and so the shed vorticity is convected downstream at the slowest rate.

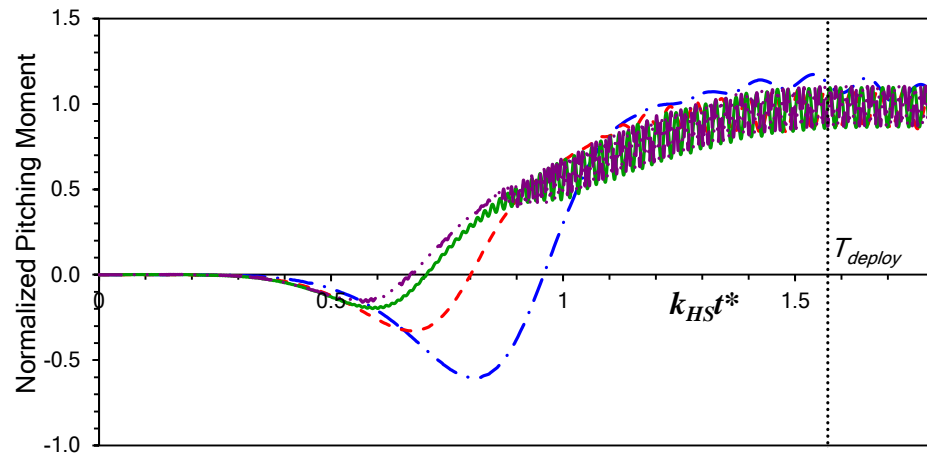
Comparing these data to results presented by Chow and van Dam [23,24] shows that the same character of the aerodynamic response is observed, albeit with slower deployment rates in this study. While this does not necessarily validate the solutions presented in this work, it shows that they are consistent with other existing upstream MiTE predictions.



(a) Lift



(b) Drag



(c) Pitching Moment

Figure 5-12. Comparison of aerodynamic responses of the VR-7 airfoil for various half-sine deployments of a $0.02c$ MiTE at $0.90c$, $\alpha = 5^\circ$, $M_\infty = 0.3$, $R = 4 \times 10^6$

5.3.4 Verification of Two-Dimensional Approach

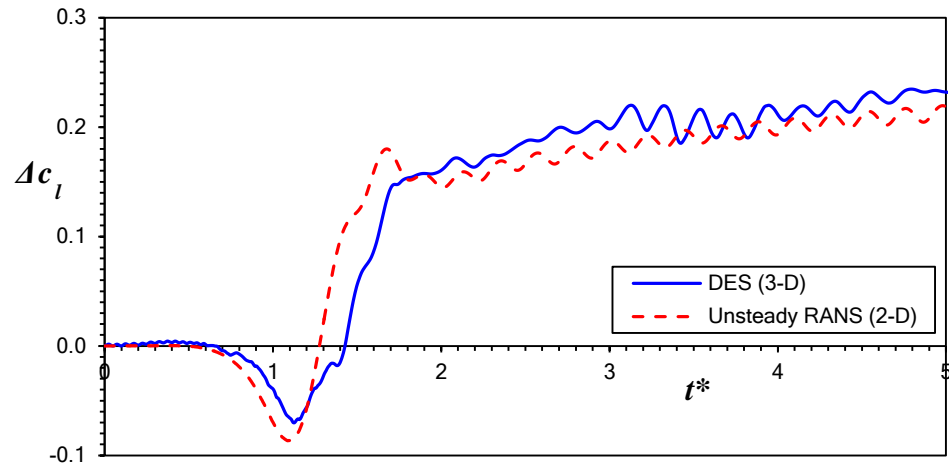
There was concern that with a large region of separated flow behind a MiTE that two-dimensional unsteady RANS was missing flow physics that are necessary to understand the unsteady aerodynamic response. To test this, a three-dimensional detached-eddy simulation (DES) [35] case was run for the VR-7 airfoil with a $k_{HS} = 1.0$ half-sine MiTE deployment at the same conditions as all previous ramp deployments. The goal is to discover what, if any, important features in the unsteady force and moment development are not captured by two-dimensional unsteady RANS, and to determine if DES solutions would be more appropriate for the present investigation.

This DES case is three-dimensional in the sense that spanwise components of the turbulence are resolved instead of being assumed to be zero, however the geometry remains two-dimensional in the sense of a wind-tunnel test being two-dimensional. Running a DES case is not as simple as switching turbulence models, as using DES on a computationally two-dimensional grid would yield poor quality results that lack physical meaning. As such, the spanwise resolution of the grid was increased to 101 grid points to capture the large-scale three-dimensional turbulence while maintaining the same tangential and normal grid relative to the airfoil.

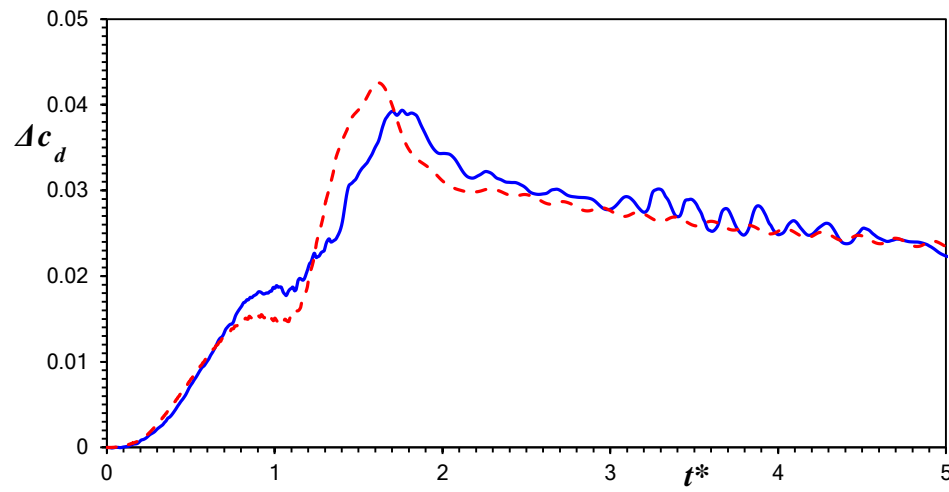
The region of interest for the DES study is that immediately downstream of the MiTE, and so the spanwise spacing was set to match the spacing in this region so that the grid would be nearly isotropic in the streamwise and spanwise directions in the region of interest. There is still grid stretching normal to the airfoil, however this was deemed to be an acceptable error for keeping the computation times and solution sizes reasonable. All solutions were run time-accurate such that the Courant number in this region would be as close to unity as possible.

The three-dimensional DES predictions for lift, drag, and pitching-moment coefficients are shown in Fig. 5-13 compared with those from two-dimensional RANS at the same conditions.

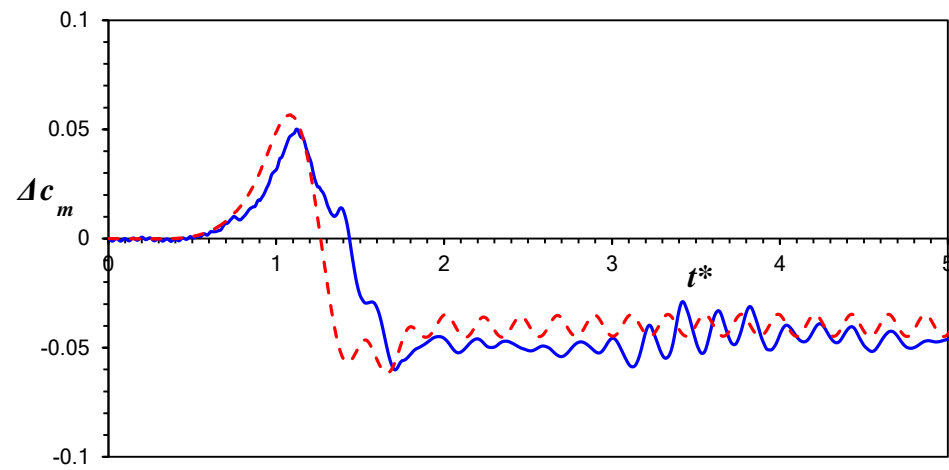
Each of the three aerodynamic coefficients shows strong qualitative and quantitative agreement between the two solutions methods. In the context of using CFD to identify important flow physics to provide a framework for the development of an unsteady MiTE model, it can be concluded that unsteady RANS sufficiently captures all important flow features that DES can predict. More specifically, it was revealed that the lower-surface vortex shows little diffusion due to three-dimensional turbulence in the DES solution and is of comparable strength to that predicted by unsteady RANS calculations.



(a) Lift



(b) Drag

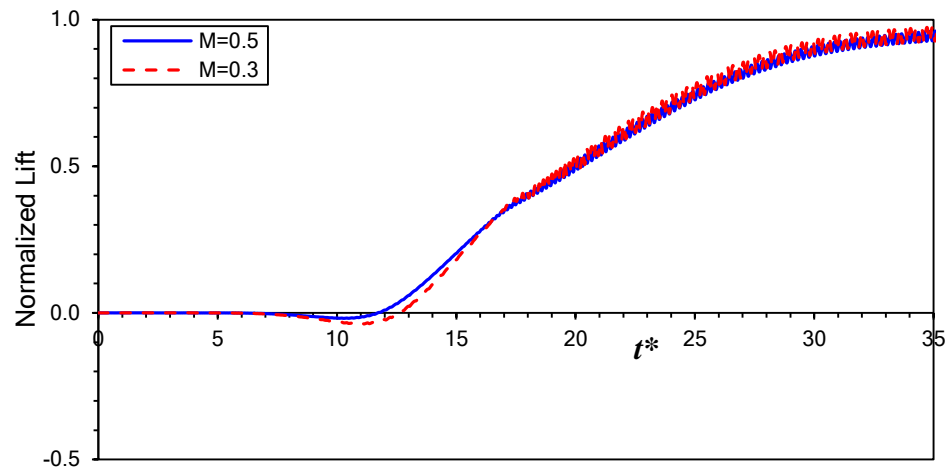


(c) Pitching Moment

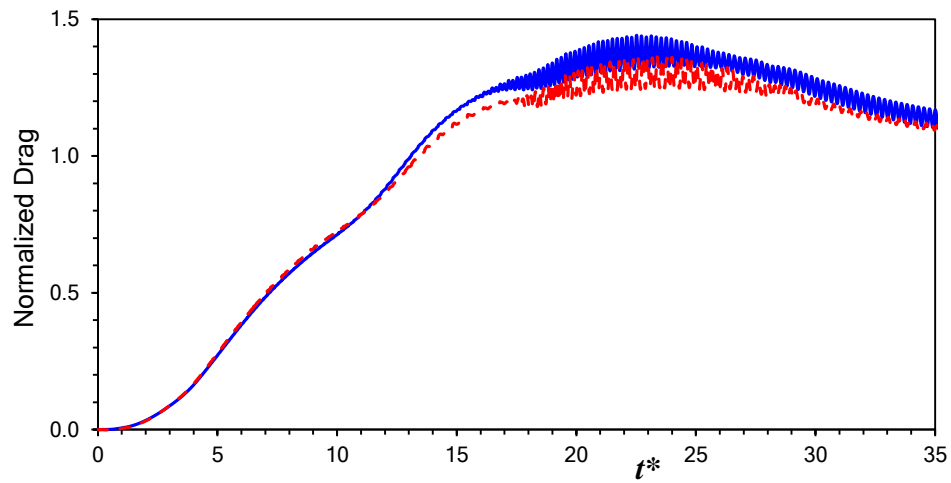
Figure 5-13. Comparison of DES (3-D) and unsteady RANS (2-D) predictions for a $k_{HS} = 1.0$ half-sine MiTE deployment on a VR-7 airfoil, $\alpha = 5^\circ$, $M_\infty = 0.3$, $R = 4 \times 10^6$

5.3.5 Effect of Compressibility

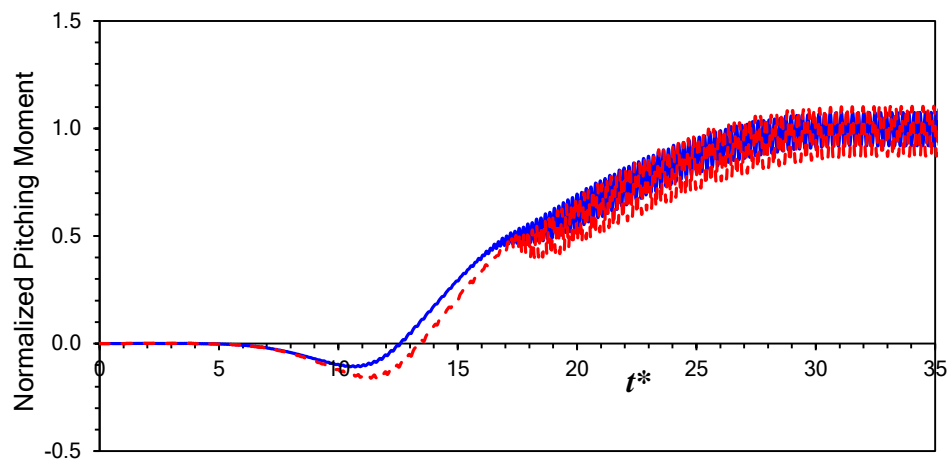
The effect of compressibility on the development of aerodynamic forces and moments was investigated through OVERFLOW solutions run with $M_\infty = 0.5$. Half-sine ramp deployments at this Mach number with $k_{HS} = 0.05$ and $k_{HS} = 0.25$ are shown in Figs. 5-14 and 5-15, respectively, along with results from $M_\infty = 0.3$. There is very similar behavior for both reduced frequencies at the two Mach numbers, except that the forces and moments develop more quickly at the higher Mach number. This is also accompanied by a reduction in the magnitude of the decrease in lift and pitching moment seen early in the deployment, along with an increase in the maximum drag predicted for the higher one. A possible explanation for the change in lift and pitching-moment predictions is that the influence of the lower surface vortex propagates upstream at a slower rate relative to the convection speed at $M_\infty = 0.5$ compared to $M_\infty = 0.3$. The increased drag predicted at $M_\infty = 0.5$ is most likely due to the baseline lift coefficient being higher, as they are at the same positive angle of attack. A similar effect can be observed in Fig. 5-6 for different angle of attacks at the same Mach number.



(a) Lift

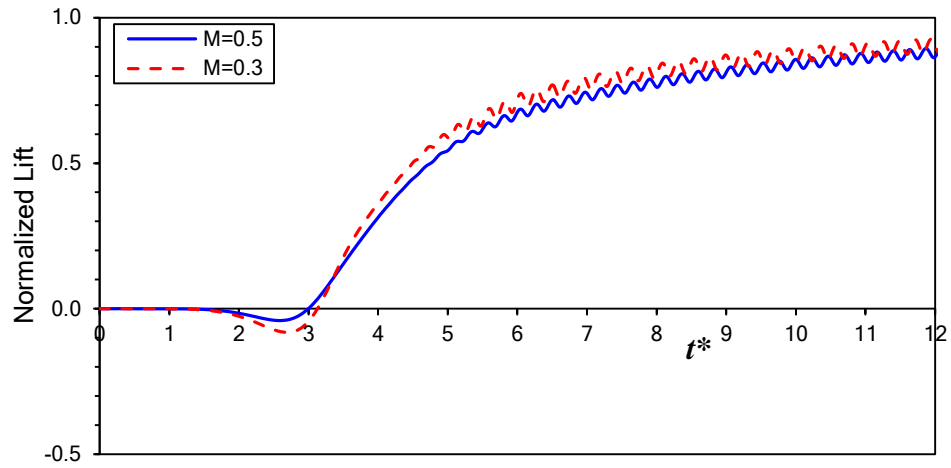


(b) Drag

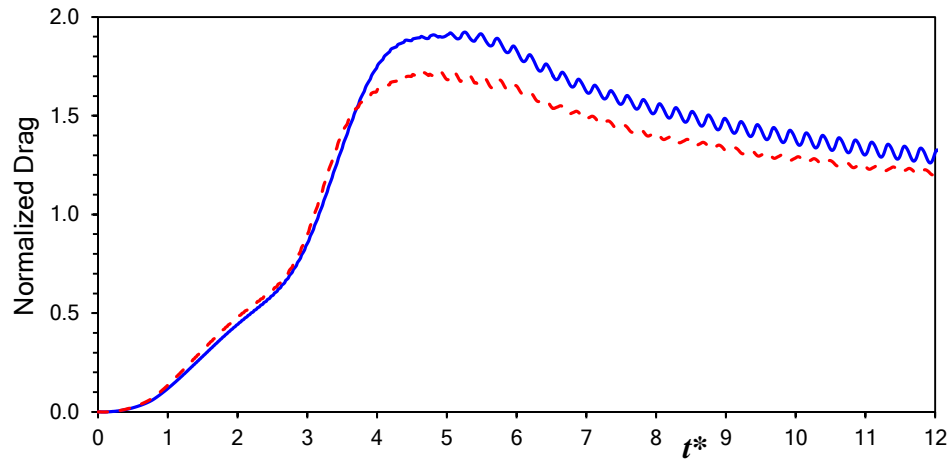


(c) Pitching Moment

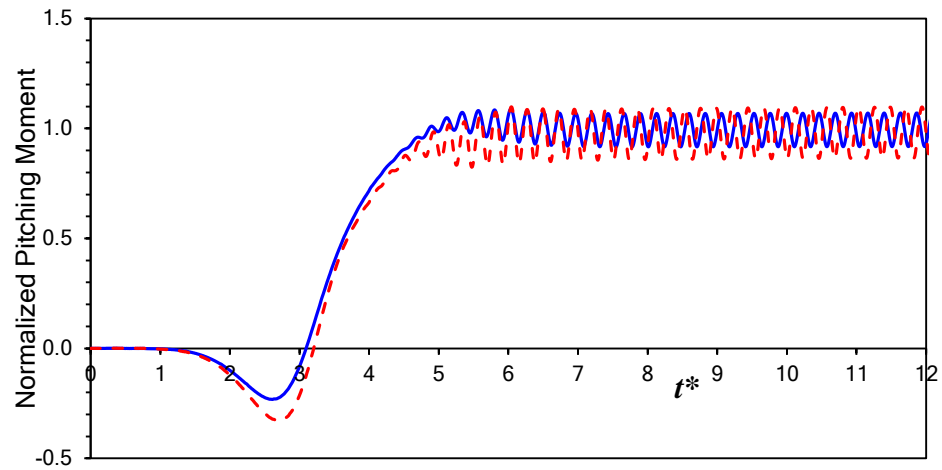
Figure 5-14. Comparison of $M_\infty = 0.3$ and $M_\infty = 0.5$ aerodynamic responses of the VR-7 airfoil for a $k_{HS} = 0.05$ half-sine deployment of a $0.02c$ MiTE at $0.90c$, $\alpha = 5^\circ$, $R = 4 \times 10^6$



(a) Lift



(b) Drag



(c) Pitching Moment

Figure 5-15. Comparison of $M_\infty = 0.3$ and $M_\infty = 0.5$ aerodynamic responses of the VR-7 airfoil for a $k_{HS} = 0.25$ half-sine deployment of a $0.02c$ MiTE at $0.90c$, $\alpha = 5^\circ$, $R = 4 \times 10^6$

5.4 Ramp Retractions

It was apparent from the oscillating upstream MiTE cases used by Kinzel [5-8] and Roedts [10,11] that the aerodynamic response for a retracting MiTE will not be identical to that of the deployment, and so CFD solutions for retraction would be necessary to develop a complete model for arbitrary MiTE translation. As such, several cases were run in OVERFLOW using a half-sine retraction scheme, which is identical to that shown in Fig. 5-4, except that the MiTE is moving upward instead of downward.

5.4.1 Effect of Retraction Rate

The first set of retraction cases were run at the baseline conditions at various deployment rates; these data are shown in Fig. 5-16, again with the ordinate normalized by k_{HS} . It can be seen in Fig. 5-16(a) that a different indicial response is truly necessary, as the response is monotonic, which contrasts with the decrease in lift that was observed immediately following a MiTE deployment. The lift and pitching moment do not show any surprising features, except that the pitching-moment coefficient for $k_{HS} = 0.1$ dips slightly below the baseline value before the MiTE is fully retracted.

The drag, however, exhibits some rather strange characteristics. At the highest reduced frequency, the drag coefficient actually decreases to below the baseline value before trending back towards it. At the lower frequencies, there is a peak in the response while the MiTE is being retracted, followed by a sharp bend in the data when the retraction is complete. The bend is peculiar in that it is not present in any of the other coefficients; a possible reason for this is that the MiTE would no longer be able to support a chordwise pressure difference at that moment, thereby changing the rate at which drag changes with time.

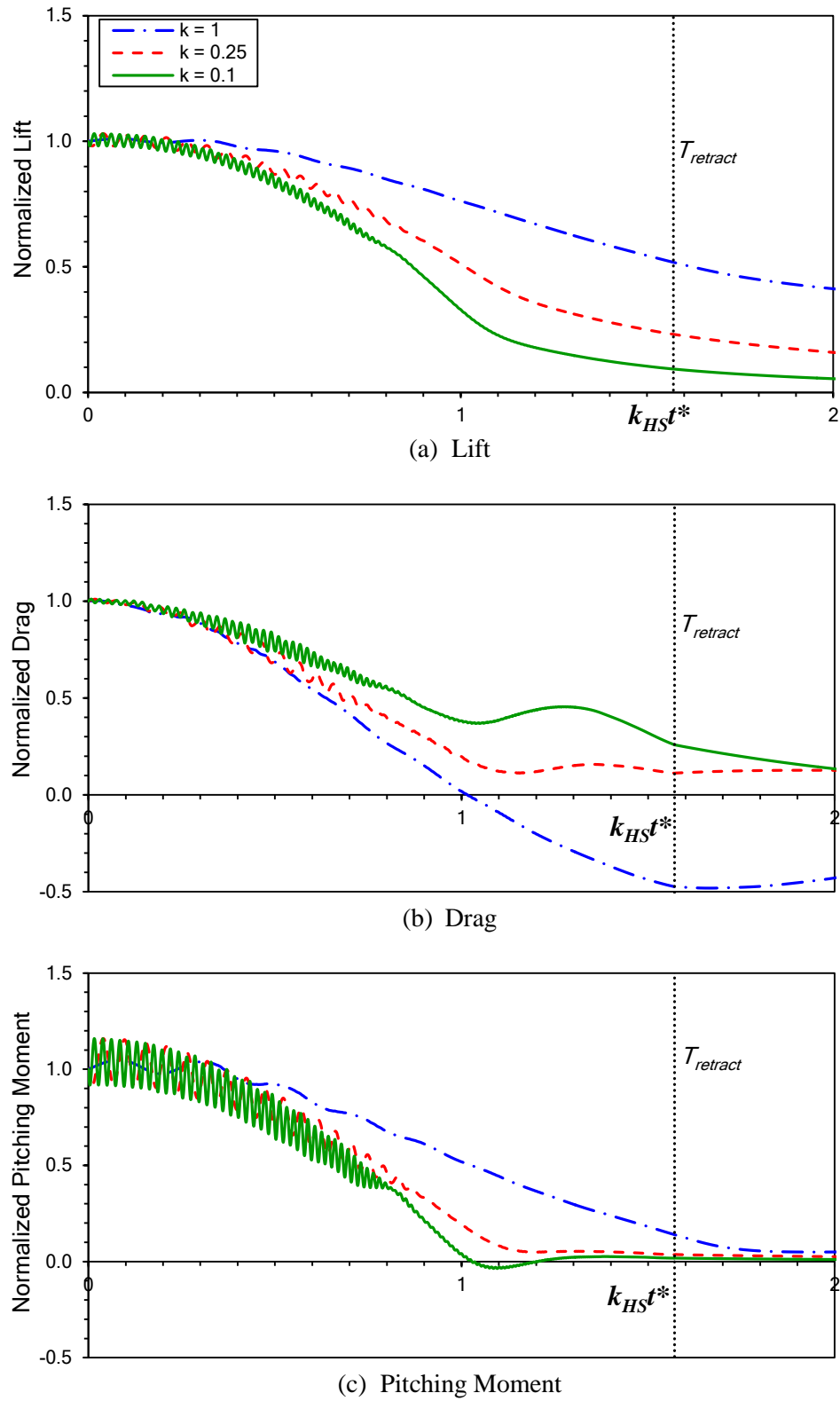


Figure 5-16. Comparison of aerodynamic responses of the VR-7 airfoil for various half-sine retractions of a $0.02c$ MiTE at $0.90c$, $\alpha = 5^\circ$, $M_\infty = 0.3$, $R = 4 \times 10^6$

5.4.2 Effect of Compressibility

As with the MiTE deployment cases, the effect of compressibility on the retraction response was investigated by comparing OVERFLOW solutions from $M_\infty = 0.5$ with those at $M_\infty = 0.3$ having identical retraction rates; comparisons for $k_{HS} = 0.1$ and $k_{HS} = 0.25$ can be seen Figs. 5-17 and 5-18, respectively. As with the deployment comparisons, there is little qualitative difference between the two solutions in lift and pitching-moment characteristics. The lift responds more slowly at the higher Mach number, while the pitching-moment responds more slowly at the lower Mach number. The drag, however, is quite different between the two Mach numbers. At $M_\infty = 0.5$, the drag coefficient drops below the baseline value, whereas at $M_\infty = 0.3$, the drag coefficient remains above the baseline value. Both Mach numbers show peaks in the drag at the same time in the response, even though the drag is below the baseline at the higher Mach number. The reasons for the higher Mach number having lower drag are presently unknown.

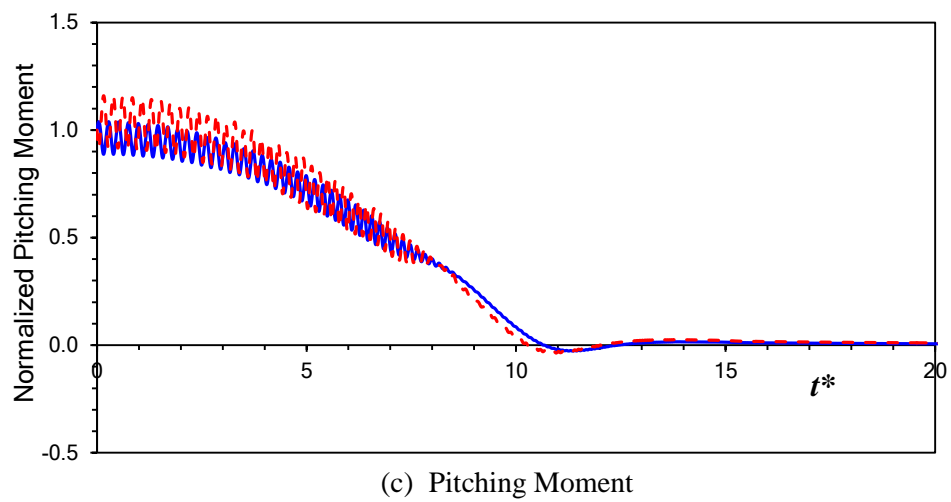
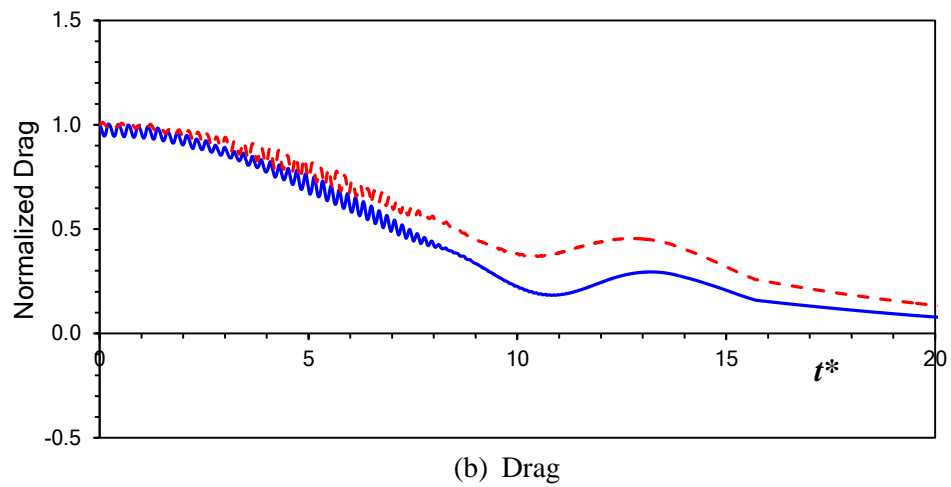
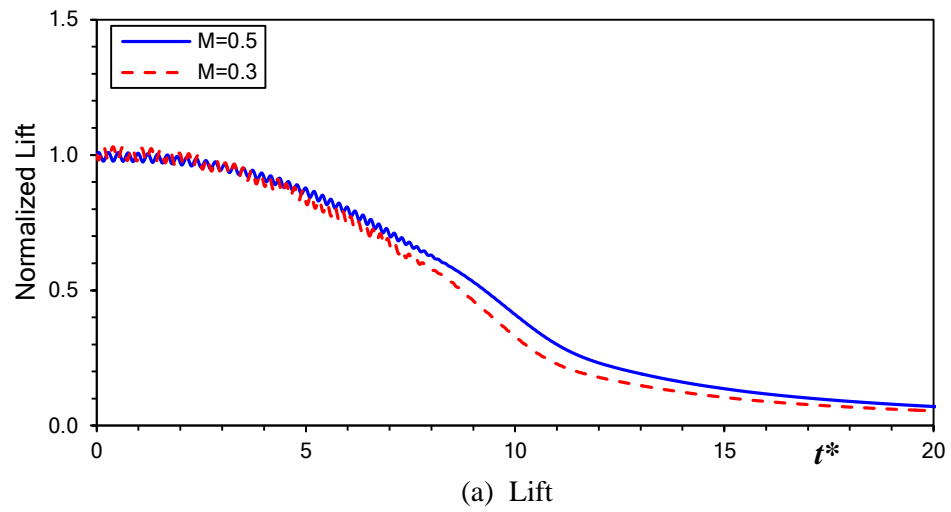


Figure 5-17. Comparison of $M_\infty = 0.3$ and $M_\infty = 0.5$ aerodynamic responses of the VR-7 airfoil for a $k_{HS} = 0.1$ half-sine retraction of a $0.02c$ MiTE at $0.90c$, $\alpha = 5^\circ$, $R = 4 \times 10^6$

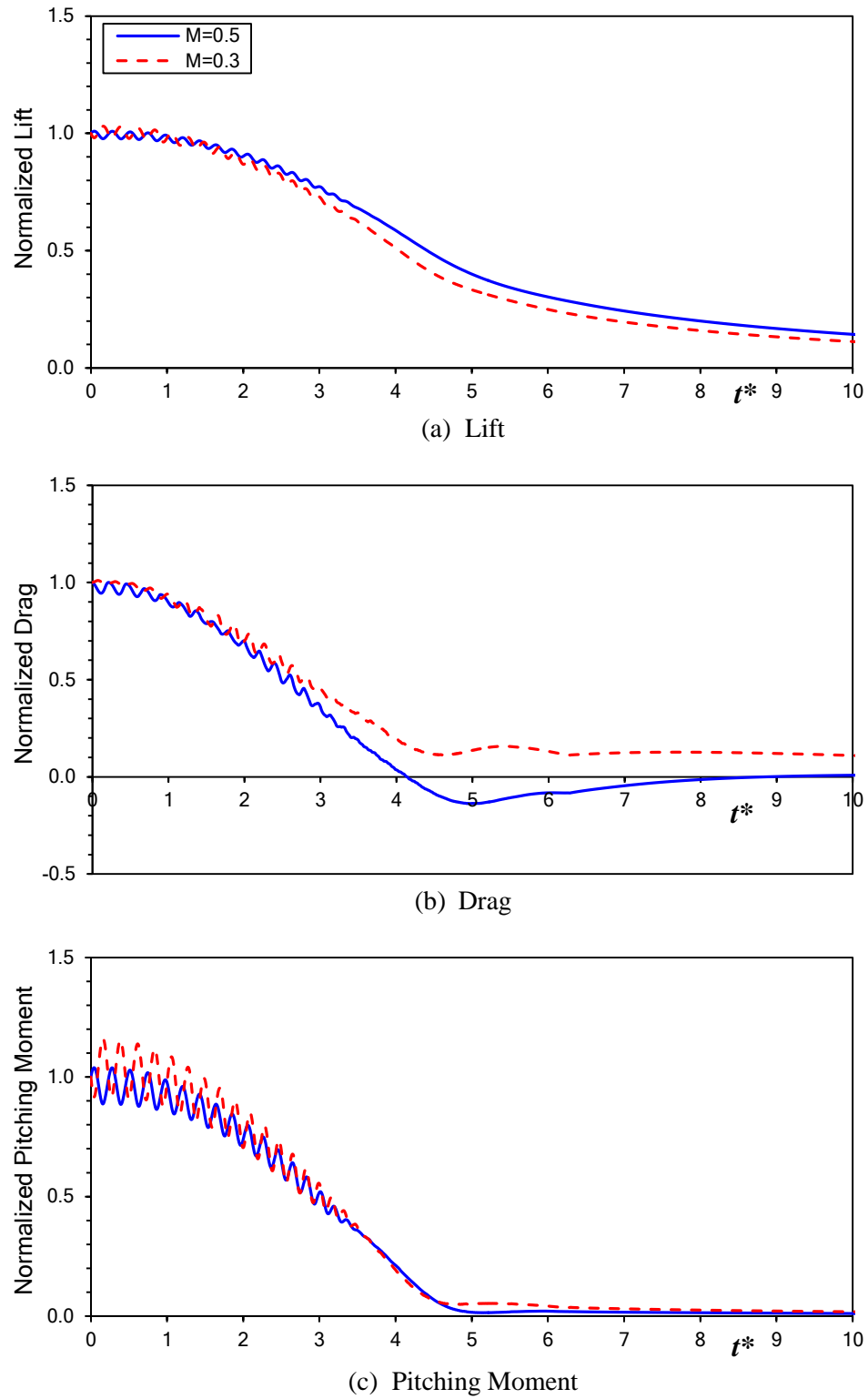


Figure 5-18. Comparison of $M_\infty = 0.3$ and $M_\infty = 0.5$ aerodynamic responses of the VR-7 airfoil for a $k_{HS} = 0.25$ half-sine retraction of a $0.02c$ MiTE at $0.90c$, $\alpha = 5^\circ$, $R = 4 \times 10^6$

5.5 Oscillating Deployments

5.5.1 Effect of Reduced Frequency

As the main rotor of a helicopter exists in an oscillatory environment, a series of oscillatory MiTE deployments were run in OVERFLOW. The selected reduced frequencies represent a range of possible 1/rev through 4/rev deployments, albeit neglecting the influence of forward flight. A rotor blade in forward flight experiences an oscillatory local velocity, as the blade is rotating at a constant rate, and the center of rotation is translating. A MiTE deploying with a constant physical frequency, such as 1 Hz, would therefore have a non-constant reduced frequency on a rotor in forward flight. It is still nevertheless useful to investigate the aerodynamics of a MiTE deploying with constant reduced frequency, as it can provide insight into how the forces and moments react when the vortices of previous deployments still influence the flow field. The results of these runs are plotted in Fig. 5-19.

The lift response follows the trends observed by Kinzel for upstream oscillating MiTEs [5-8], with the deviations from the trailing-edge MiTE behavior increasing with reduced frequency. At all times during the oscillation the lift coefficient remains bounded by the static Gurney flap result, although the lift decreases below the clean airfoil result for a portion of the oscillation at higher frequencies. The pitching-moment coefficient follows a similar trend with reduced frequency, although all frequencies appear to reach the Gurney flap result when the MiTE is fully deployed. Similar deviations from trailing-edge MiTE behavior are also seen, with the pitching-moment coefficient becoming increasingly nose-up for a portion of the oscillation. This corresponds with the portion of the oscillation where lift has noticeably decreased, confirming that this is in fact due to the lower surface vortex.

The drag coefficients show an unexpected result in that they are above the corresponding “quasi-steady” response for all frequencies for essentially all heights during the oscillation. While most likely not an issue for retreating-blade stall mitigation, this could have a major impact on the use of MiTEs for rotorcraft overall power reduction and individual blade control. One must be careful that reduction of induced power using MiTEs to redistribute the thrust loading on the rotor disk may be offset by a profile power penalty that is not accounted for in quasi-steady analyses.

An example of the trailing-edge MiTE behavior as calculated by Kinzel [5] is included for reference as Fig. 5-20.

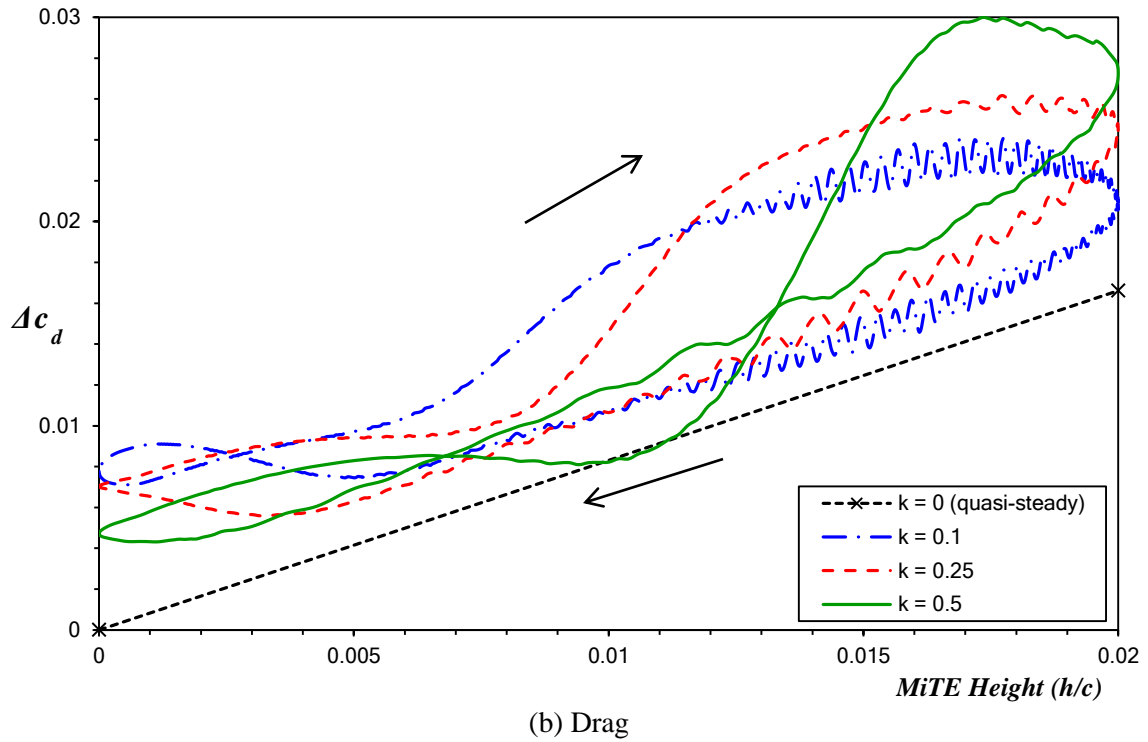
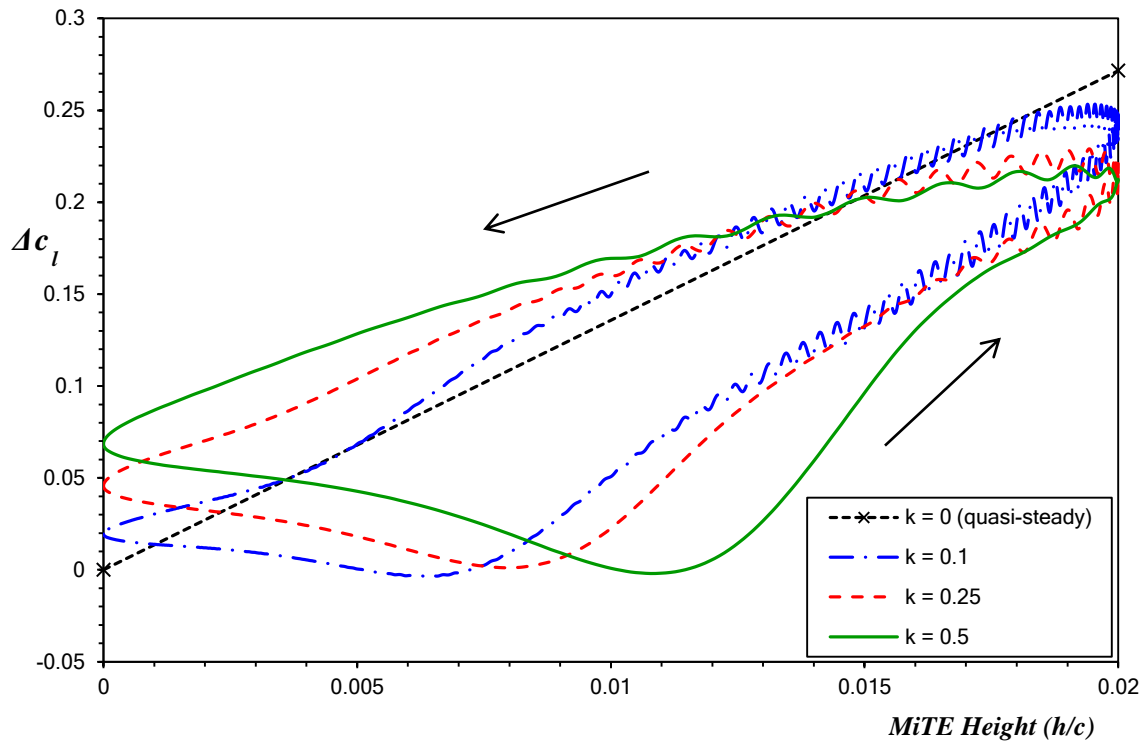


Figure 5-19. Comparison of limit-cycle aerodynamic responses of the VR-7 airfoil for various oscillatory deployments of a $0.02c$ MiTE at $0.90c$, $\alpha = 5^\circ$, $M_\infty = 0.3$, $R = 4 \times 10^6$

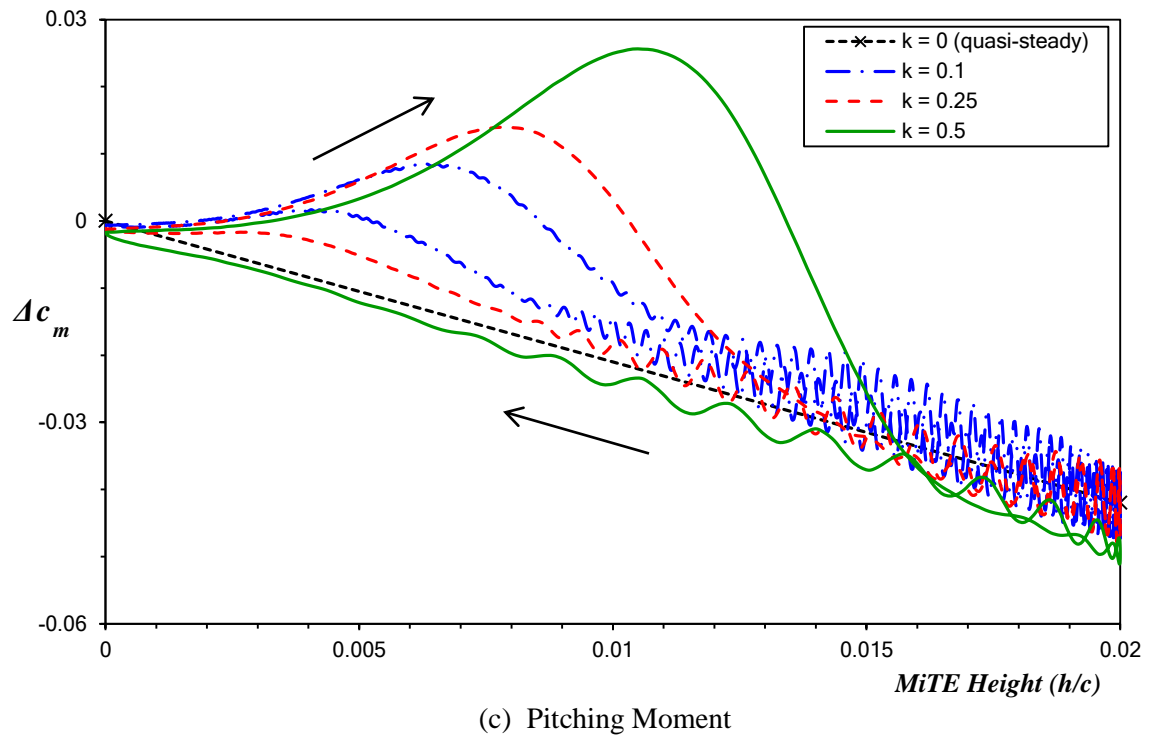
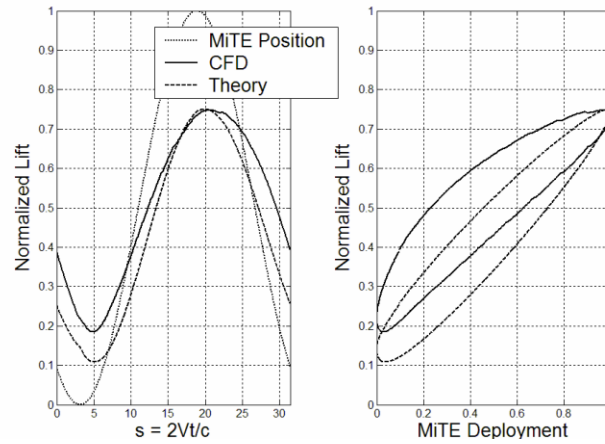
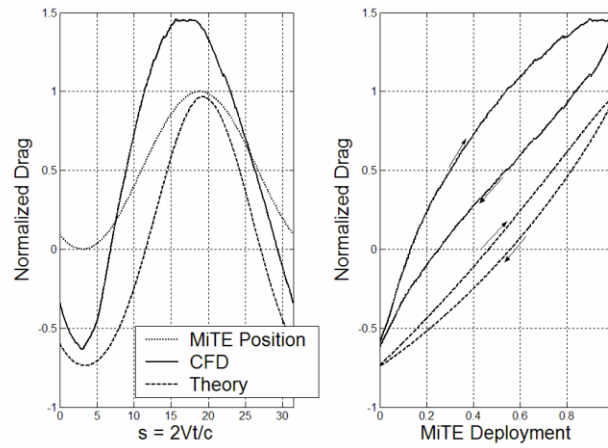


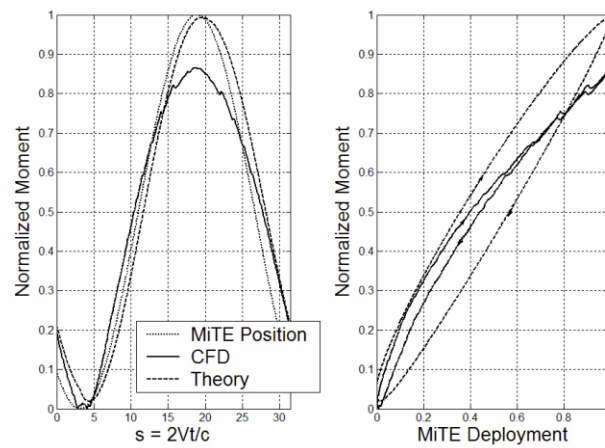
Figure 5-19 (concluded). Comparison of limit-cycle aerodynamic responses of the VR-7 airfoil for various oscillatory deployments of a $0.02c$ MiTE at $0.90c$, $\alpha = 5^\circ$, $M_\infty = 0.3$, $R = 4 \times 10^6$



(a) Lift



(b) Drag

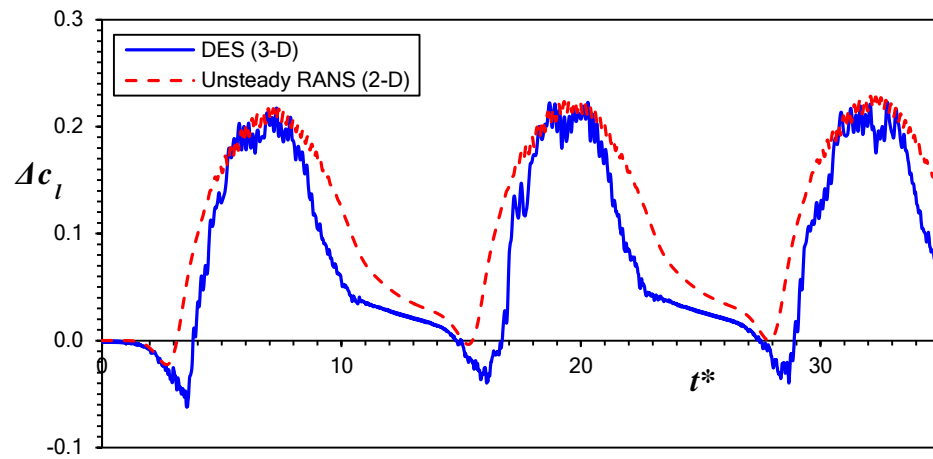


(c) Pitching Moment

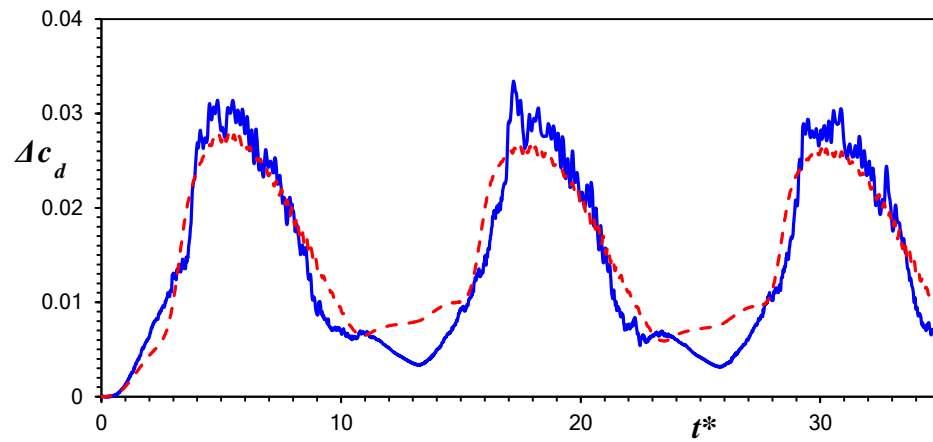
Figure 5-20. Comparisons between CFD predictions and Kinzel's trailing-edge MiTE model for $k = 0.2$, $M_\infty = 0.3$, $\alpha = 10^\circ$ [5]

5.5.2 DES Verification

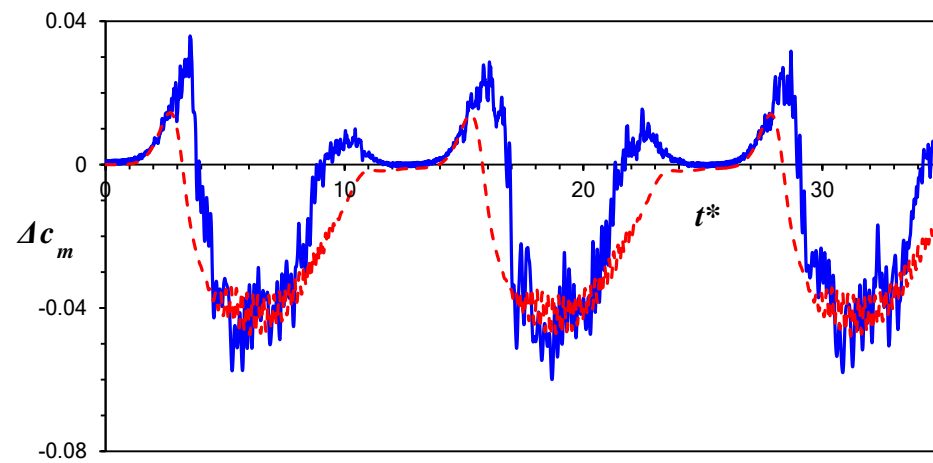
The two-dimensional unsteady RANS approach was also compared with three-dimensional DES predictions for an oscillating MiTE with $k = 0.25$. These results are presented in Fig. 5-20; the data are plotted with respect to non-dimensional time for clarity. The lift coefficient response shows extremely good qualitative agreement between the two methods. The magnitude of the lift deficit region is predicted to be greater using DES compared to using RANS, but the phase angle of this feature shows strong agreement. The pitching-moment response using DES shows an additional nose-up peak as the MiTE is being retracted that is not captured with the RANS solution. The phase angle of the nose-up peak during MiTE deployment shows good agreement, but the DES solution predicts it to have a larger magnitude. The DES predictions for the drag coefficient also show reasonable agreement with the RANS predictions, except that DES predicts a more distinct “valley” in the response during MiTE retraction. Even with the DES solution showing additional features in the aerodynamic responses, it shows that a two-dimensional unsteady RANS is sufficiently accurate for understanding the unsteady aerodynamic response due to a MiTE.



(a) Lift



(b) Drag



(c) Pitching Moment

Figure 5-21. Comparison of DES (3-D) and unsteady RANS (2-D) predictions for a $k = 0.25$ oscillating MiTE deployment on a VR-7 airfoil, $\alpha = 5^\circ$, $M_\infty = 0.3$, $R = 4 \times 10^6$

5.5.3 Comparison with Experiment

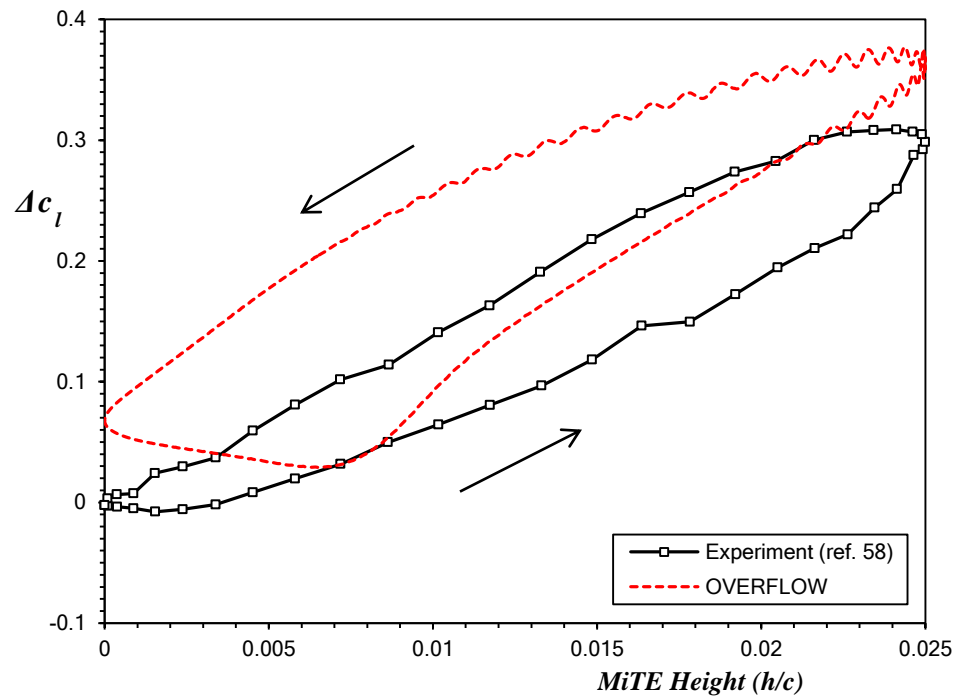
Experimental results for an oscillating upstream MiTE on an NACA 0012 airfoil were published by Tang and Dowell which provide a potentially useful dataset for validating the computational methods used in this study [58]. This geometry was analyzed in OVERFLOW at the same angle of attack and Reynolds number, but with a slightly higher Mach number of 0.2 to provide improved numerical stability. The OVERFLOW solutions for lift, drag, and pitching-moment coefficient are compared with the Tang and Dowell experiment [58] in Fig. 5-21.

The lift coefficient predictions show reasonable agreement with the experiment, except that the results are shifted up by approximately 0.08. The experimental data does not appear to show any influence from a lower-surface vortex, whereas the CFD predictions show it clearly.

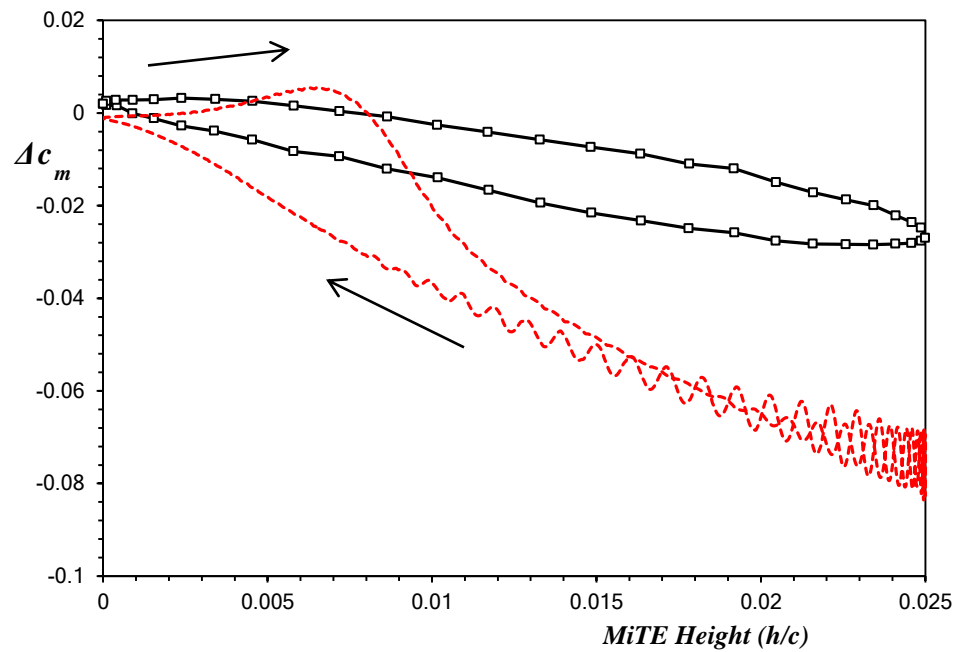
The agreement between CFD and experiment is somewhat poor for the pitching-moment coefficient. While the two curves return to similar value when the MiTE is fully retracted, the computational results predict the maximum magnitude of the nose-down pitching moment to be significantly higher than was observed in the experiment. Again, the CFD predictions show the influence of the lower-surface vortex while the experiment shows no such characteristics.

An aspect of the Tang and Dowell experiment that must be noted is that the wind-tunnel model had only one pressure tap aft of the MiTE on the lower surface [58], thus providing inadequate resolution of the pressure distribution between the flap and the trailing edge. Not only would this lack of resolution introduce errors in the integrated lift and pitching moment, but the influence of the lower-surface vortex during MiTE deployment would not be directly measured.

An additional peculiarity of the experimental data is that both the lift and pitching-moment hysteresis loops return to the baseline values when the MiTE is retracted [58]. If the experimental lift coefficient were shifted more positive by 0.08, then there would be significant improvement in the agreement between the two curves.



(a) Lift



(b) Pitching Moment

Figure 5-22. Comparison of OVERFLOW predictions with experiment [58] for a $0.025c$ MiTE at $0.90c$ oscillating at $k = 0.204$ on an NACA 0012 airfoil, $R = 0.348 \times 10^6$

Chapter 6

Summary and Conclusions

6.1 Static CFD Analyses

The OVERFLOW computational fluid dynamics solver has been validated for the analysis of static airfoils, both with and without Gurney flaps. The linear region of the lift curve is well-captured, including the zero-lift angle of attack and the zero-lift pitching moment. There are several considerations that need to be made when performing such analyses, as the available transition models do not capture the influence of either natural transition or transition via a laminar separation bubble. As a result of this, the maximum lift coefficient is generally overpredicted by the solver. The drag coefficients below stall are overpredicted as well. The pitching-moment coefficient predictions shows noticeable deviations from experiment for clean airfoil configurations, and the agreement improves significantly once a Gurney flap is deployed. It is believed that this is due to the influence of trailing-edge separation on the pitching-moment coefficient; a upper- and lower-surface separation points on a clean airfoil are dependent on the details of the boundary layer growth, while a Gurney flap provides a well-defined separation location on the lower surface.

6.2 Dynamic Stall Predictions

OVERFLOW was also shown to be a useful tool for predicting the onset of dynamic stall for a harmonically oscillating airfoil. The VR-7 airfoil used in the dynamic simulations was first analyzed statically using OVERFLOW, FLUENT, and XFOIL. The OVERFLOW results

overpredicted the maximum lift coefficient relative to experiment, and there was also error in the prediction of the zero-lift angle of attack. These deviations were accounted for in the dynamic stall predictions through the use of a quasi-steady lift scaling. This scaling was compared to results obtained from OVERFLOW by matching the raw angle of attack range and it was shown that the scaled predictions were, in general, more accurate.

The difference in the zero-lift angle of attack as predicted by OVERFLOW and observed in the experiment is of some concern. It was shown in the static CFD studies that OVERFLOW generally showed good agreement for this quantity. Given that OVERFLOW predictions were in agreement with those from FLUENT, an unstructured solver using a different turbulence model, and XFOIL, a panel method with an integral boundary layer, the accuracy of the reported experimental data should be further investigated.

As there is no readily-applicable quasi-steady mapping for the pitching-moment coefficient, there was no attempt in this study to use a scaling to improve the accuracy of the predictions.

6.3 CFD Investigation of Upstream MiTEs

Important details of the transient flow field affecting an upstream MiTE have been investigated and yielded valuable insight. An indicially deploying MiTE forms a vortex immediately downstream of the MiTE which subsequently convects downstream. It was found that this vortex is responsible for creating the lift deficit and increase in nose-up pitching moment observed early in the transient response. For slower, ramp deployments this vortex becomes distributed and its influence is reduced.

The qualitative details of the aerodynamic response for a deploying MiTE were discovered to be airfoil-independent, with the quantitative details following a trend that depends

on the lower surface pressure distribution. The influence of the vortex is stronger for higher pressure coefficients in the MiTE region. The implication of this result is that an unsteady upstream MiTE aerodynamic model needs some way of accounting for the pressure distribution of the clean airfoil in order to provide an accurate prediction.

For an oscillating upstream MiTE, the lower-surface vortex also introduces deviations from the normal unsteady hysteresis loop that was previously observed for trailing-edge MiTEs. These deviations can be thought of as additional harmonics in the aerodynamic coefficients, which must be captured by an unsteady upstream MiTE model. This could have a major impact on the use of MiTEs for rotorcraft performance enhancement and rotor vibration control. While the oscillatory cases presented in this study do not model the time-varying velocity of a rotor flow field, they provide a useful dataset for qualifying the predictions of an unsteady model.

The two-dimensional, unsteady RANS approach for the indicial, ramp, and oscillating MiTE deployments was justified through comparisons with three-dimensional DES solutions. For all comparisons shown, the RANS solution showed very good qualitative agreement with the DES predictions. In the context of using CFD as a “virtual wind tunnel” to foster the development of an unsteady upstream MiTE model, using DES solutions would not provide enough additional detail to justify the significantly increased computation time.

The influence of an oscillating MiTE on an NACA 0012 airfoil was also investigated in OVERFLOW and compared with experimental data from Duke University. The CFD predictions showed good agreement with the experiment for lift coefficient, considering that the model used for the wind-tunnel test had only one lower-surface pressure tap aft of the MiTE and that the experimental data appeared to be shifted to the baseline lift coefficient. The pitching-moment coefficient showed the same quality agreement as the lift coefficient, but this appears to also be due to the experiment have inadequate resolution of the lower-surface pressure distribution.

From these comparisons, it can be concluded that OVERFLOW is a useful, validated tool for analyzing upstream MiTEs, and that the solver functions well for providing unsteady data for the development of an unsteady aerodynamic model.

6.4 Recommendations for Future Work

6.4.1 Transition in Unsteady CFD Simulations

The Langtry-Menter transitional turbulence model was explored for the static VR-7 case, but it was not utilized in any unsteady simulations. Future CFD investigations into dynamic stall should seriously consider using this transition model, as it may provide better predictions for the lift and pitching-moment coefficients without the need for a scaling factor. This particular transition model has already been implemented into the various ANSYS flow solvers, but it should also be possible to implement it in OVERFLOW as well.

6.4.2 Additional Unsteady MiTE Experiments

The Tang and Dowell data for an oscillating upstream MiTE is a useful set of data, but it would be beneficial for the development of CFD methods and an unsteady aerodynamic model to perform additional experiments with higher resolution of the pressure distributions. This would provide additional validation of the computational methods and also allow the opportunity to determine if the lower-surface vortex is physically realistic and learn how it influences the unsteady development of forces and moments.

Appendix A

Description of Langtry-Menter Turbulence Model [40-42]

The additional transport equations of the L-M model are given as:

$$\frac{\partial(\rho\gamma)}{\partial t} + \frac{\partial(\rho U_j \gamma)}{\partial x_j} = P_\gamma - E_\gamma + \frac{\partial}{\partial x_j} \left[\left(\mu + \frac{\mu_t}{\sigma_f} \right) \frac{\partial \gamma}{\partial x_j} \right] \quad \text{A.1}$$

$$\frac{\partial(\rho \tilde{Re}_{\theta t})}{\partial t} + \frac{\partial(\rho U_j \tilde{Re}_{\theta t})}{\partial x_j} = P_{\theta t} + \frac{\partial}{\partial x_j} \left[\sigma_{\theta t} (\mu + \mu_t) \frac{\partial \tilde{Re}_{\theta t}}{\partial x_j} \right] \quad \text{A.2}$$

All correlations for the variables in the above equations are defined in Ref. 42. The underlying assumption of the transition correlation is that the boundary layer momentum thickness can be calculated based on the vorticity Reynolds number using the following relations:

$$Re_v = \frac{\rho y^2}{\mu} \left| \frac{\partial u}{\partial y} \right| \quad \text{A.3}$$

$$Re_\theta = \frac{\max(Re_v)}{2.193} \quad \text{A.4}$$

The constant in the denominator of Eq. A-4 is based on the result for the Blasius profile. Langtry and Menter show that the error of using this constant is less than 10% for shape factors associated with moderate pressure gradients, however extreme gradients can cause the error to be as great as 20-40%. The influence of the pressure gradient is incorporated into the transition correlation by use of the following parameter:

$$\lambda_\theta = \frac{\rho \theta^2}{\mu} \frac{dU}{ds} \quad \text{A.5}$$

While this is similar to the Twaites-Walz parameter, the velocity gradient is defined locally in the turbulence model rather than from the inner limit of the outer flow solution. The

Langtry-Menter model makes no use of the pressure gradient parameter in the calculation of momentum thickness Reynolds number, and the reasons for this are unclear.

The production of the intermittency variable is determined from empirical correlations based on the transitional momentum-thickness Reynolds number, which is itself a transport variable. The intermittency variable is coupled with the turbulence model by multiplying the turbulent kinetic energy production term of the original SST model. Thus when the intermittency is zero, there is no turbulence produced in the boundary layer and it is laminar. Once the transition criterion is satisfied, the intermittency increases to unity and transition occurs.

Appendix B

Airfoil Coordinates

Table B-1. Somers S903 airfoil coordinates [52]

<u>Upper Surface</u>		<u>Lower Surface</u>	
x/c	y/c	x/c	y/c
0.00001	0.00035	0.00011	-0.00088
0.00032	0.00180	0.00072	-0.00201
0.00242	0.00608	0.00182	-0.00317
0.00942	0.01372	0.00411	-0.00490
0.02086	0.02187	0.01420	-0.00970
0.03671	0.03007	0.02963	-0.01426
0.05695	0.03802	0.05031	-0.01838
0.08152	0.04554	0.07601	-0.02209
0.11029	0.05253	0.10643	-0.02536
0.14306	0.05897	0.14123	-0.02820
0.17946	0.06490	0.18001	-0.03057
0.21899	0.07029	0.22234	-0.03247
0.26115	0.07502	0.26775	-0.03390
0.30544	0.07897	0.31573	-0.03486
0.35132	0.08201	0.36574	-0.03536
0.39827	0.08397	0.41722	-0.03541
0.44581	0.08464	0.46959	-0.03502
0.49357	0.08384	0.52226	-0.03419
0.54122	0.08146	0.57462	-0.03295
0.58849	0.07752	0.62607	-0.03129
0.63507	0.07208	0.67602	-0.02922
0.68070	0.06529	0.72392	-0.02668
0.72507	0.05739	0.76934	-0.02360
0.76790	0.04867	0.81194	-0.02009
0.80885	0.03953	0.85137	-0.01636
0.84753	0.03044	0.88711	-0.01255
0.88343	0.02189	0.91879	-0.00882
0.91595	0.01437	0.94609	-0.00537
0.94435	0.00830	0.96860	-0.00261
0.96779	0.00397	0.98563	-0.00087
0.98538	0.00138	0.99633	-0.00014
0.99630	0.00026	1.00000	0.00000
1.00000	0.00000		

Table B-2. Vertol VR-7 airfoil coordinates [30]

	<u>Upper Surface</u>	<u>Lower Surface</u>
x/c	y/c	y/c
0.00000	0.00000	0.00000
0.00050	0.00337	-0.00330
0.00100	0.00483	-0.00460
0.00200	0.00696	-0.00633
0.00350	0.00943	-0.00800
0.00500	0.01149	-0.00919
0.00650	0.01330	-0.01010
0.00800	0.01494	-0.01086
0.01000	0.01695	-0.01172
0.01250	0.01923	-0.01263
0.01600	0.02213	-0.01367
0.02000	0.02512	-0.01467
0.02500	0.02846	-0.01575
0.03500	0.03423	-0.01751
0.05000	0.04144	-0.01966
0.06500	0.04759	-0.02154
0.08000	0.05299	-0.02320
0.10000	0.05922	-0.02516
0.12500	0.06565	-0.02709
0.15000	0.07091	-0.02855
0.20000	0.07887	-0.03055
0.25000	0.08378	-0.03186
0.30000	0.08592	-0.03273
0.35000	0.08575	-0.03308
0.40000	0.08365	-0.03271
0.45000	0.07984	-0.03148
0.50000	0.07451	-0.02952
0.55000	0.06781	-0.02712
0.60000	0.05996	-0.02464
0.65000	0.05171	-0.02207
0.70000	0.04322	-0.01929
0.75000	0.03442	-0.01639
0.80000	0.02527	-0.01346
0.85000	0.01575	-0.01050
0.90000	0.00558	-0.00744
0.92500	0.00117	-0.00609
0.95000	-0.00016	-0.00512
0.97500	0.00115	-0.00380
0.99000	0.00194	-0.00300
1.00000	0.00247	-0.00247

REFERENCES

1. Leishman, J. G., *Principles of Helicopter Aerodynamics*, 2nd ed., Cambridge University Press, New York, 2006.
2. Martin, P. B., Wilson, J. S., Berry, J. D., Wong, T., Moulton, M., and McVeigh, M. A., "Passive Control of Compressible Dynamic Stall," 26th AIAA Applied Aerodynamics Conference, AIAA 2008-7506, Honolulu, HI, 18-21 August 2008.
3. Maughmer, M., Lesieutre, G., Thepvongs, S., Anderson, W., and Kinzel, M., "Miniature Trailing-Edge Effectors for Rotorcraft Applications," American Helicopter Society 59th Annual Forum Proceedings, Phoenix, AZ, May 6–8, 2003.
4. Kentfield, J. A. C., "The Potential of Gurney Flaps for Improving the Aerodynamic Performance of Helicopter Rotors," AIAA International Powered Lift Conference, AIAA Paper 1993-4883, Santa Clara, CA, December 1–3, 1993.
5. Kinzel, M. P., "Miniature Trailing-Edge Effectors for Rotorcraft Applications," M.S. Thesis, Department of Aerospace Engineering, The Pennsylvania State University, University Park, PA, Aug. 2004.
6. Kinzel, M. P., Maughmer, M. D., Lesieutre, G. A., and Duque, E. P. N., "Numerical Investigation of Miniature Trailing-Edge Effectors on Static and Oscillating Airfoils," 43rd AIAA Aerospace Sciences Meeting and Exhibit, AIAA 2005-1039, Reno, NV, 10-13 January 2005.
7. Kinzel, M. P., Maughmer, M. D., and Lesieutre, G. A., "Miniature Trailing-Edge Effectors for Rotorcraft Performance Enhancement," *Journal of the American Helicopter Society*, Vol. 52, No. 2, April 2007, pp. 146–158.
8. Kinzel, M. P., Maughmer, M. D., and Duque, E. P. N., "Numerical Investigation on the Aerodynamics of Oscillating Airfoils with Deployable Gurney Flaps," *AIAA Journal*, Vol. 48, No. 7, July 2010, pp. 1457-1469.
9. Yen-Nakafuji, D. T., van Dam, C. P., Smith, R. L., and Collins, S. D., "Active Load Control for Airfoils Using Microtabs," *Journal of Solar Energy Engineering*, Vol. 123, No. 4, 2001, pp. 282–289.
10. Roedts, R. L., "Rotorcraft Performance Enhancements Due to a Lower-Surface Effector," M. S. Thesis, Department of Aerospace Engineering, The Pennsylvania State Univ., University Park, PA, Aug. 2008.
11. Roedts, R. L. and Maughmer, M. D., "Rotorcraft Performance Enhancements Due to a Lower-Surface Effector," 35th European Rotorcraft Forum, Hamburg, Germany, 22-25 September 2009.

12. Leishman, J. G. and Beddoes, T. S., "A Semi-Empirical Model for Dynamic Stall," *Journal of the American Helicopter Society*, Vol. 34, No. 3, July 1989, pp. 3-17.
13. Tran, C. T. and Petot, D., "Semi-Empirical Model for the Dynamic Stall of Airfoils in View of the Application to the Calculation of the Responses of a Helicopter Blade in Forward Flight," *Vertica*, Vol. 5, No. 1, 1981, pp. 35-53.
14. Ko, S. and McCroskey, W. J., "Computations of Unsteady Separating Flows over an Oscillating Airfoil," *AIAA Journal*, Vol. 35, No. 7, July 1997, pp. 1235-1238.
15. McCroskey, W. J., Carr, L. W., Wilson, J. W., and Martin, P. B., "US Army Dynamic Stall Data Package for NASA TM 84245," US Army AFDD (RDECOM), July 2008.
16. Liebeck, R. H., "Design of Subsonic Airfoils for High Lift," *Journal of Aircraft*, Vol. 15, No. 9, September 1978, pp. 547-561.
17. Jang, C. S., Ross, J. C., and Cummings, R. M., "Computational Evaluation of an Airfoil with a Gurney Flap," 10th AIAA Applied Aerodynamics Conference, AIAA 1992-2708, Palo Alto, CA, 22-24 June 1992.
18. Date, J. C. and Turnock, S. R., "Computation Evaluation of the Periodic Performance of a NACA 0012 Fitted With a Gurney Flap," *Journal of Fluids Engineering*, Vol. 124, March 2002, pp. 227-234.
19. Lee, H-T. and Kroo, I. M., "Computational Investigation of Airfoils with Miniature Trailing Edge Control Surfaces," 42nd AIAA Aerospace Sciences Meeting and Exhibit, AIAA 2004-1051, Reno, NV, 5-8 January 2004.
20. Lee, H-T. and Kroo, I. M., "Two Dimensional Unsteady Aerodynamics of Miniature Trailing Edge Effectors," 44th AIAA Aerospace Sciences Meeting and Exhibit, AIAA 2006-1057, Reno, NV, 9-12 January 2006.
21. Standish, K.J. and van Dam, C.P., "Computational Analysis of a Microtab-Based Aerodynamic Load Control System for Rotor Blades," American Helicopter Society Aeromechanics Specialists' Conference, San Francisco, CA, January 2004.
22. Mayda, E. A., van Dam, C. P., and Nakafuji, D. Y., "Computational Investigation of Finite Width Microtabs for Aerodynamic Load Control," 43rd AIAA Aerospace Sciences Meeting and Exhibit, AIAA 2005-1185, Reno, NV, 10-13 January 2005.
23. Chow, R. and van Dam, C. P., "Unsteady Computational Investigations of Deploying Load Control Microtabs," *Journal of Aircraft*, Vol. 43, No. 5, September-October 2006, pp. 1458-1469.
24. Chow, R. and van Dam, C. P., "Computational Investigations of Deploying Load Control Microtabs on a Wind Turbine Airfoil," 45th AIAA Aerospace Sciences Meeting and Exhibit, AIAA 2007-1018, Reno, NV, 8-11 January 2007.
25. Matalanis, C. G., Wake, B. E., Opoku, D., Min, B-Y., Yeshala, N., and Sankar, L., "Aerodynamic Evaluation of Miniature Trailing-Edge Effectors for Active Rotor Control," American Helicopter Society 66th Annual Forum and Technology Display Proceedings, Phoenix, AZ, May 11-13, 2010.

26. Min, B-Y., Sankar, L. N., Rajmohan, N., and Prasad, J. V. R., "Computational Investigation of Gurney Flap Effects on Rotors in Forward Flight," *Journal of Aircraft*, Vol. 46, No. 6, November-December 2009, pp. 1957-1964.
27. Liu, L., Padthe, A. K., and Friedmann, P. P., "A Computational Study of Microflaps with Application to Vibration Reduction in Helicopter Rotors," 50th AIAA/ASME/ASCE/AHS/ASC Structures, Structural Dynamics and Materials Conference, AIAA 2009-2604, Palm Springs, CA, 4-7 May 2009.
28. Maughmer, M. D. and Bramesfeld, G., "Experimental Investigation of Gurney Flaps," *Journal of Aircraft*, Vol. 45, No. 6, November-December 2008, pp 2062-2067.
29. Vieira, B. A. O., "An Investigation of the Aerodynamics of Miniature Trailing-Edge Effectors Applied to Rotorcraft," M. S. Thesis, Department of Aerospace Engineering, The Pennsylvania State Univ., University Park, PA, Aug. 2010.
30. McCroskey, W. J., McAlister, K. W., Carr, L. W., and Pucci, S. L., "An Experimental Study of Dynamic Stall on Advanced Airfoil Sections Volume 1. Summary of the Experiment," NASA-TM-84245, July 1982.
31. McAlister, K. W., Pucci, S. L., McCroskey, W. J., and Carr, L. W., "An Experimental Study of Dynamic Stall on Advanced Airfoil Sections Volume 2. Pressure and Force Data," NASA-TM-84245, September 1982.
32. Nichols, R. and Buning, P., "User's Manual for OVERFLOW 2.1", Version 2.1t, August 2008.
33. Spalart, P. R. and Allmaras, S. R., "A One-Equation Turbulence Model for Aerodynamic Flows," 30th AIAA Aerospace Sciences Meeting and Exhibit, AIAA 1992-0439, Reno, NV, 6-9 January 1992.
34. Menter, F. R., "Two-Equation Eddy-Viscosity Turbulence Models for Engineering Applications," *AIAA Journal*, Vol. 32, No. 8, August 1994, pp. 1598-1605.
35. Spalart, P., Jou, W-H., Strelets, M., and Allmaras, S. "Comments on the Feasibility of LES for Wings and on a Hybrid RANS/LES Approach," First AFOSR Conference on DNS/LES, August 1997, C. Liu and Z. Liu editors, Greyden Press, Columbus, Ohio.
36. Pulliam, T. H. and Chaussee, D. S., "A Diagonalized Form of an Implicit Approximate Factorization Algorithm," *Journal of Computational Physics*, Vol. 39, February 1981, pp. 347-363.
37. Beam, R. M. and Warming, R. F., "An Implicit Finite-Difference Algorithm for Hyperbolic Systems in Conservation-Law Form," *Journal of Computational Physics*, Vol. 22, September 1976, pp. 87-110.
38. Boger, D. A. and Dreyer, J. J., "Prediction of Hydrodynamic Forces and Moments for Underwater Vehicles Using Overset Grids," 44th Aerospace Sciences Meeting and Exhibit, AIAA 2006-1148, Reno, NV, 9-12 January 2006.
39. "ANSYS FLUENT 12.0 Users Guide," ANSYS, Incorporated, January 2009.

40. Menter, F. R., Langtry, R. B., Likki, S. R., Suzen, Y. B., Huang, P. G., and Völker, S., "A Correlation-Based Transition Model Using Local Variables – Part I: Model Formulation," *Journal of Turbomachinery*, Vol. 128, July 2006, pp. 413-422.
41. Langtry, R. B., Menter, F. R., Likki, S. R., Suzen, Y. B., Huang, P. G., and Völker, S., "A Correlation-Based Transition Model Using Local Variables – Part II: Test Cases and Industrial Applications," *Journal of Turbomachinery*, Vol. 128, July 2006, pp. 423-434.
42. Langtry, R. B. and Menter, F. R., "Correlation-Based Transition Modeling for Unstructured Parallelized Computational Fluid Dynamics Codes," *AIAA Journal*, Vol. 47, No. 12, December 2009, pp. 2894-2906.
43. Drela, M. and Youngren, H., "XFOIL 6.94 User Guide," Massachusetts Institute of Technology, Cambridge, MA, 2001.
44. Chan, W. M., Rogers, S. E., Nash, S. M., Buning, P. G., Meakin, R. L., Boger, D. A., Pandya, S., "Chimera Grid Tools User's Manual, Version 2.0," NASA Ames Research Center, July 2007.
45. Chan, W. M., Gomez, R. J., Rogers, S. E. and Buning, P. G., "Best Practices in Overset Grid Generation," 32nd AIAA Fluid Dynamics Conference, AIAA 2002-3191, St. Louis, Missouri, June, 2002.
46. Benek, J. A., Buning, P. G., and Steger, J. L., "A 3-D CHIMERA Grid Embedding Technique," 7th Computational Fluid Dynamics Conference, AIAA 1985-1523, Cincinnati, OH, 15-17 July 1985.
47. "GAMBIT Modeling Guide," Fluent, Inc, November 1999.
48. Somers, D.M. and Maughmer, M.D., "Design and Experimental Results for the S408 Airfoil," Airfoils, Incorporated, February 2010.
49. Somers, D.M. and Maughmer, M.D., "Experimental Results for the E 387 Airfoil at Low Reynolds Numbers in The Pennsylvania State University Low-Speed, Low-Turbulence Wind Tunnel," U.S. Army Research, Development and Engineering Command TR 07-D-32, May 2007.
50. Medina, R., "Validation of The Pennsylvania State University Low-Speed, Low-Turbulence Wind Tunnel Using Measurements of the S805 Airfoil," M.S. Thesis, Department of Aerospace Engineering, Penn State University, University Park, PA, 1994.
51. Maughmer, M. D. and Coder, J. G., "Comparisons of Theoretical Methods for Predicting Airfoil Aerodynamic Characteristics," Airfoils, Incorporated, April 2010.
52. Somers, D. M., "Effects of Airfoil Thickness and Maximum Lift Coefficient on Roughness Sensitivity," NREL/SR-500-36336, 1998.
53. Abbott, I. H. and von Doenhoff, A. E., *Theory of Wing Sections: Including a Summary of Airfoil Data*, 1st ed., Dover Publications, Mineola, NY, 1959.
54. "FIELDVIEW Reference Manual, Software Release Version 12" Intelligent Light, 2007.

55. Drazin, P. G. and Reid, W. H., *Hydrodynamic Stability*, 2nd ed., Cambridge University Press, New York, 2004.
56. Hayek, S. I., *Advanced Mathematical Methods in Science and Engineering*, Marcel Dekker, New York, 2001.
57. Katz, J. and Plotkin, A., *Low-Speed Aerodynamics*, 2nd ed., Cambridge University Press, New York, 2001.
58. Tang, D. and Dowell, E. H., "Aerodynamic Loading for an Airfoil with an Oscillating Gurney Flap," *Journal of Aircraft*, Vol. 44, No. 4, July-August 2007, pp 1245-1257.